

การศึกษาพลศาสตร์ลำอนุภาคอิเล็กตรอนของอุปกรณ์แทรกสนามแม่เหล็กสูง  
สำหรับเครื่องกำเนิดแสงสยาม



วิทยานิพนธ์นี้เป็นส่วนหนึ่งของการศึกษาตามหลักสูตรปริญญาวิทยาศาสตรมหาบัณฑิต  
สาขาวิชาฟิสิกส์  
มหาวิทยาลัยเทคโนโลยีสุรนารี  
ปีการศึกษา 2557

**ELECTRON BEAM DYNAMICS STUDIES OF HIGH  
FIELD INSERTION DEVICES FOR THE SIAM PHOTON  
SOURCE**



**Siriwan Krainara**

**A Thesis Submitted in Partial Fulfillment of the Requirements for the  
Degree of Master of Science in Physics  
Suranaree University of Technology  
Academic Year 2014**

# **ELECTRON BEAM DYNAMICS STUDIES OF HIGH FIELD INSERTION DEVICES FOR THE SIAM PHOTON SOURCE**

Suranaree University of Technology has approved this thesis submitted in partial fulfillment of the requirements for a Master's Degree.

Thesis Examining Committee

---

(Assoc. Prof. Dr. Prayoon Songsiriritthigul)

Chairperson

---

(Prof. Dr. Santi Maensiri)

Member (Thesis Advisor)

---

(Asst. Prof. Dr. Supagorn Rugmai)

Member

---

(Dr. Prapong Klysubun)

Member

---

(Asst. Prof. Dr. Worawat Meevasana)

Member

---

(Prof. Dr. Sukit Limpijumnong)

Vice Rector for Academic Affairs  
and Innovation

---

(Assoc. Prof. Dr. Prapun Manyum)

Dean of Institute of Science

ศิริวรรณ ไกรนรา : การศึกษาพลศาสตร์ลำอนุภาคอิเล็กตรอนของอุปกรณ์แทรก  
สนามแม่เหล็กสูงสำหรับเครื่องกำเนิดแสงสยาม (ELECTRON BEAM DYNAMICS  
STUDIES OF HIGH FIELD INSERTION DEVICES FOR THE SIAM PHOTON  
SOURCE) อาจารย์ที่ปรึกษา : ศาสตราจารย์ ดร.สันติ แม้นศิริ, 169 หน้า.

เครื่องกำเนิดแสงสยามเป็นวงกักเก็บอิเล็กตรอนที่มีพลังงาน 1.2 กิกะอิเล็กตรอน โวลต์ ซึ่งถูกสร้างขึ้นมาเพื่อผลิตแสงซินโครตรอนจากสนามแม่เหล็กสองขั้ว ในการที่จะตอบสนองความต้องการของผู้ใช้ในการทดลองที่จะใช้แสงซินโครตรอนในย่านที่มีพลังงานสูงที่เรียกว่า รังสีเอกซ์พลังงานสูง (Hard X-ray) ได้มีการติดตั้งอุปกรณ์แทรกสองตัวเข้าไปในวงซึ่งประกอบด้วยไฮบริดมัลติโพลวิกเกิลเลอร์ (hybrid multipole wiggler) ขนาด 2.18 เทสลา และอุปกรณ์แทรกแบบตัวนำยิ่งยวด (superconducting wavelength shifter) ขนาด 6.5 เทสลา โดยอุปกรณ์แทรกเหล่านี้จะผลิตแสงที่มีพลังงานและความเข้มหรือความสว่างสูงกว่าแสงซินโครตรอนที่ผลิตจากสนามแม่เหล็กสองขั้ว แต่เนื่องด้วยอุปกรณ์แทรกที่ติดตั้งจะทำให้พลศาสตร์ลำอนุภาคของวงกักเก็บอิเล็กตรอนมีความผิดเพี้ยน ส่งผลให้จำนวนรอบของการกวัดแกว่งอิเล็กตรอนเปลี่ยนไปจึงทำให้ค่าเบตาตรอนฟังก์ชัน (betatron function) สูงกว่าปกติและขอบเขตเสถียรภาพของการเคลื่อนที่ของอิเล็กตรอนลดลง ดังนั้นค่าพารามิเตอร์ต่างๆ ของลำอิเล็กตรอนหลังจากติดตั้งอุปกรณ์แทรกทั้งสองตัว จึงต้องมีการคำนวณและปรับปรุงแก้ไขพลศาสตร์ลำอนุภาคเพื่อชดเชยการรบกวนที่เกิดจากอุปกรณ์แทรกที่ยังส่งผลให้ช่วงชีวิตของลำแสงลดลง ผลของการศึกษาค้นคว้าครั้งนี้พบว่า จุดให้บริการแสง ( $v_x, v_y$ ) ถูกเปลี่ยนจาก (4.768 2.813) เป็น (4.790 2.818) เพื่อเพิ่มช่วงชีวิตของลำแสงในวงกักเก็บอิเล็กตรอนให้สามารถเดินเครื่องกำเนิดแสงสยามกับอุปกรณ์แทรกทั้งสองได้ ทั้งยังผลิตแสงซินโครตรอนในย่านรังสีเอกซ์พลังงานสูงที่มีประสิทธิภาพและเสถียรภาพตามความต้องการแก่ผู้ใช้ที่ต้องการกระแสของลำอิเล็กตรอนต้องมากกว่า 50 มิลลิแอมแปร์ เมื่อให้บริการแสงไปแล้วเป็นเวลา 11 ชั่วโมง

สาขาวิชาฟิสิกส์  
ปีการศึกษา 2557

ลายมือชื่อนักศึกษา \_\_\_\_\_  
ลายมือชื่ออาจารย์ที่ปรึกษา \_\_\_\_\_



SIRIWAN KRAINARA : ELECTRON BEAM DYNAMICS STUDIES OF  
HIGH FIELD INSERTION DEVICES FOR THE SIAM PHOTON SOURCE.

THESIS ADVISOR : PROF. SANTI MAENSIRI, D.Phil. 169 PP.

INSERTION DEVICE/WAVELENGTH SHIFTER/WIGGLER/HARD X-RAYS.

The Siam Photon Source (SPS) is a 1.2 GeV electron storage ring. It was designed to use the dipole magnets for generating synchrotron radiation. In order to fulfill the increasing demand of users for hard X-ray, the Synchrotron Light Research Institute (SLRI) has installed two high field insertion devices (IDs) into the SPS storage ring; i.e. a 2.18 Tesla hybrid multipole wiggler and a 6.5 Tesla superconducting wavelength shifter. These devices will provide higher photon energy and flux density of synchrotron radiation than those produced from the bending magnets. Due to an influence of the IDs installation, the lattice distortion, betatron tune shift, beta-beating, and dynamic aperture reduction were calculated and compensated during commissioning of the IDs with the machine. The beam lifetime decreases due to the effects from the IDs. Therefore the operating point  $(\nu_x, \nu_y)$  was optimized and changed from (4.768, 2.813) to (4.790, 2.818) to increase the beam lifetime. After commissioning, the machine can operate with the two IDs with high beam stability. The beam current is higher than 50 mA after operating for 11 hours, which meets the beamline user requirements.

School of Physics

Student's Signature \_\_\_\_\_

Academic Year 2014

Advisor's Signature \_\_\_\_\_

## ACKNOWLEDGEMENTS

First of all, I would like to thank my advisor, Prof. Dr. Santi Maensiri and co-advisor, Asst. Prof. Dr. Supagorn Rugmai for their advice throughout this work. I am extremely grateful to them for giving me an opportunity to study in the graduate course in School of Physics of the Suranaree University of Technology. I specially thank the Director of the Accelerator Technology Division of SLRI, Dr. Prapong Klysubun and gratefully thank Assoc. Prof. Dr. Prayoon Songsiriritthigul for their help and good supports. This thesis could not be possible without kindness of them.

I am also deeply indebted to Miss Porntip Sudmuang, Dr. Supat Klinkhieo, Dr. Anusorn Tong-on, Dr. Nawin Junthong, Source Utility Machine Operation team (SUMO), and to all accelerator members in Siam Photon Laboratory (SPL) for their help in the calculation, measurement, and all of my research methodologies. I would like to extend my thanks to the SLRI for giving me the opportunity to work in the accelerator division. And I especially thank Mr. George Garnet Hoyes, Dr. Prapaiwan Sunwong, Dr. Sampart Cheedget, and Dr. Roengrut Rujanakraikarn for their comments on the writing.

In addition, I would like to thank Prof. Dr. Jim Clarke from ASTEC in England for his suggestion on MPW shimming and Dr. Chang Ho-Ping from NSRRC in Taiwan for useful discussion on commissioning processes of IDs with the machine.

Finally, I gratefully acknowledge my family and friends for their support throughout the period of this thesis.

Siriwan Krainara

# CONTENTS

	<b>Page</b>
ABSTRACT IN THAI .....	I
ABSTRACT IN ENGLISH.....	II
ACKNOWLEDGEMENTS.....	III
CONTANTS .....	IV
LIST OF TABLES.....	VIII
LIST OF FIGURES .....	X
<b>CHAPTER</b>	
<b>I INTRODUCTION.....</b>	<b>1</b>
1.1 Motivation.....	1
1.2 Siam photon source.....	3
1.3 Insertion devices at SLRI.....	8
1.4 Review of the beam dynamics studied.....	16
1.5 Research objectives.....	19
1.6 Scopes and limitations of the study .....	19
<b>II THEORY OF ACCELERATOR BEAM DYNAMICS AND INSERTION DEVICES EFFECTS .....</b>	<b>20</b>
2.1 Synchrotron light source .....	20
2.1.1 Particle motion and accelerator magnets .....	20
2.1.2 Beam parameters.....	24
2.1.3 The transformation matrix .....	30

## CONTENTS (Continued)

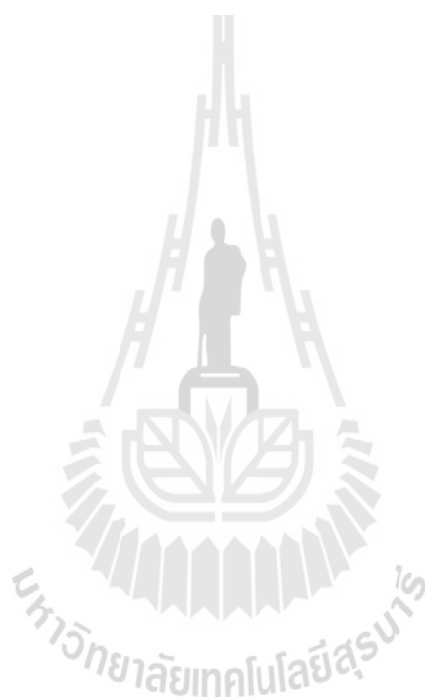
	<b>Page</b>
2.1.4 Beam lifetime.....	32
2.2 Review of insertion devices.....	34
2.2.1 Characteristics of insertion devices.....	34
2.2.2 The motion of electron in insertion devices.....	40
2.3 Effects of insertion devices on beam dynamics.....	41
2.3.1 Tune shift.....	42
2.3.2 Beta-Beating.....	43
2.4 The effect due to the emission of synchrotron radiation.....	44
2.4.1 Momentum compaction.....	44
2.4.2 Energy loss.....	45
2.4.3 Energy spread.....	46
2.4.4 Emittance.....	47
<b>III MAGNETIC FIELD MEASUREMENT OF TWO INSERTION DEVICES.....</b>	<b>49</b>
3.1 Measuring tools.....	50
3.1.1 Hall probe.....	50
3.1.2 Flipping coil.....	51
3.2 Magnetic field mapping of two insertion devices.....	53
3.3 Measurement and compensation of magnetic field integral.....	56
3.3.1 Superconducting wavelength shifter (SWLS).....	58
3.3.2 Hybrid multipole wiggler (MPW).....	70
3.4 Electron trajectory.....	75

## CONTENTS (Continued)

		Page
<b>V</b>	<b>RESEARCH METHODOLOGIES</b> .....	78
	4.1 Operating point optimization .....	78
	4.1.1 Observation of the operation point .....	79
	4.1.2 Operation point selection .....	82
	4.2 Beam optics calculation .....	83
	4.2.1 Calculating model .....	84
	4.2.2 Beam optics calculation and compensation .....	85
	4.2.3 Beam compensation process .....	92
	4.3 Commissioning of insertion devices at SPS .....	94
	4.3.1 Beam injection with Ids at a beam energy of 1.0 GeV .....	96
	4.3.2 Ramping up energy to 1.2 GeV .....	97
	4.3.3 Closing the MPW to a minimum gap of 23.5 mm .....	98
<b>VI</b>	<b>RESULTS AND DISCUSSION OF SWLS AND MPW</b> .....	104
	5.1 Observation of operating point .....	105
	5.2 The effects of insertion devices and commissioning results .....	113
	5.2.1 Effects of the insertion devices on the beam dynamics .....	116
	5.2.2 Effects of radiation from insertion devices .....	143
	5.3 The stored electron for user service .....	147
	5.4 The future work .....	155
<b>VII</b>	<b>CONCLUSIONS</b> .....	156
	REFERENCES .....	161
	APPENDIX .....	167

## CONTENTS (Continued)

	<b>Page</b>
CURRICULUM VITAE.....	169



## LIST OF TABLES

Table	Page
1.1 The quadrupole and sextupole magnets parameters for the bare lattice of SPS storage ring with the emittance of 61nm-rad. ....	6
1.2 Parameters of SPS storage ring.....	7
1.3 The SWLS and MPW specifications .....	13
2.1 Resonance lines and the driving forces up to 5 <sup>th</sup> order.....	27
3.1 The measured results at 6.5 Tesla SWLS magnetic field of the dipole corrector, quadrupole, and sextupole magnet .....	66
3.2 The currents of correction coil are used to compensate field error of SWLS.....	67
3.3 The measured results at 2.18 Tesla MPW magnetic field of the multipole components.....	74
3.4 The electron's trajectories pass though the SWLS and MPW.....	77
4.1 The tune response procedure are observed and measured by adjusting the QF1 and QD2 current magnets .....	80
4.2 The angel parameters of the insertion devices at a beam energy of 1.2 GeV .....	85
4.3 Steering magnet parameters for the SWLS and MPW .....	92
4.4 The factors $B\rho/g$ of the quadrupole magnets for converting the strength, k (m <sup>-2</sup> ) to current (A) for a bare ring.....	96
5.1 Compared beam optic parameters between two operating points .....	107

## LIST OF TABLES (Continued)

<b>Table</b>	<b>Page</b>
5.2 The quadrupole magnets parameters of SPS storage ring without IDs ....	109
5.3 The emittance ratio and beam size of SPS storage ring without IDs.....	112
5.4 Sextupole strength magnets for chromaticities correction.....	129
5.5 The steering magnet current adjacent to SWLS and MPW at 1.2 GeV....	135
5.6 Magnet current are used in the real machine for beam operation in Ampere at 1.0 GeV beam injection.....	139
5.7 The quadrupole current magnets as a function of beam energy (E), and MPW gap with 4.0 Tesla SWLS and 4.6 Tesla SWLS.....	140
5.8 Magnet current are used in the real machine at a beam energy 1.2 GeV with 170A SWLS.....	141
5.9 Magnet current are used in the real machine at a beam energy 1.2 GeV with 200A SWLS.....	142
5.10 The energy loss in the SPS storage ring after installing insertion devices in keV/turn. ....	147
5.11 Magnet current are used in the real machine for beam operation in Ampere.....	148
5.12 Magnet current are used in the real machine at a beam energy 1.2 GeV with two IDs.....	149
5.13 The beam size in the SPS storage ring at different the magnetic field of IDs.....	151
5.14 The beam lifetime in SPS storage ring different conditions .....	153



## LIST OF FIGURES

Figure	Page
1.1 Schematic diagram of Siam Photon Source.....	3
1.2 Double Bend Acrobat (DBA) lattice for the SPS storage ring .....	4
1.3 Bending magnet, Steering magnet, Quadrupole magnet, and Sextupole magnet in the SPS storage ring .....	5
1.4 Tune diagram showing sum resonance lines up to and including the 5th order and operating point with emittance of 61 nm-rad. ....	7
1.5 Betatron and dispersion functions of bare ring lattice with electron beam emittance of 61nm-rad for a 1.2 GeV SPS storage ring.....	8
1.6 Photon flux density generated by electron beams as a function of photon energy. The stored electron beam current is 150 mA at energy of 1.2 GeV.....	9
1.7 The superconducting wavelength shifter from TLS .....	11
1.8 The measured vertical field at the SWLS current of 308 A along the SWLS and B-I curve of SWLS .....	12
1.9 The hybrid multipole wiggler from SRS .....	14
1.10 The magnetic field of MPW at the gap of 20 mm along the MPW and The peak magnetic field of MPW as a function of the pole gaps .....	15
2.1 Bending magnets.....	23
2.2 Defocusing quadrupole magnets.....	23
2.3 Focusing sextupole magnets. ....	24

## LIST OF FIGURES (Continued)

<b>Figure</b>	<b>Page</b>
2.4	Shape of the phase space ellipse depend on the Twiss parameters..... 26
2.5	The change momentum of electron particle when passes though the bending magnet..... 28
2.6	The correction of chromatic effects. .... 29
2.7	An electron trajectory when pass though along the drift space and quadrupole magnet..... 30
2.8	The synchrotron radiation emitted from an electron beam by bending, wiggler, and undulator ..... 35
2.9	Coils set up used in the superconducting wavelength shifter. .... 36
2.10	The cable and cross-section of NbTi wires which are made superconducting coils..... 37
2.11	Schematic of a hybrid (left) and pure permanent (right) magnets insertion devices..... 38
2.12	Peak of the field as a function of the ratio of the magnetic gap to period for a pure permanent magnet structure and a hybrid structure with pole made of Vanadium Permendur. .... 39
2.13	Schematic principle of the creation of synchrotron radiation. An electron trajectory along s-axis passes though the device magnet..... 41
3.1	Model 460 configured as a-axis gaussmeter ..... 50
3.2	Hall probe set up for measured magnetic field of SWLS and MPW..... 51
3.3	The flipping coil diagram and the moving method for measuring the field integral..... 52

## LIST OF FIGURES (Continued)

Figure	Page
3.4	The flipping coil set up for measuring first and second field integral of SWLS..... 52
3.5	Measured vertical field component along the longitudinal axis of SWLS and MPW..... 54
3.6	Peak magnetic field with different excited current of SWLS and MPW gap at center position $x = y = z = 0$ ..... 55
3.7	The flipping coil system diagram. .... 58
3.8	The configuration coil for the first and second field integral measurements of SWLS..... 58
3.9	Side view of the magnetic field vector along the longitudinal axis..... 59
3.10	The schematic views for vertical and horizontal field integrals measurements..... 61
3.11	The signals by using the flipping coil for vertical and horizontal field integrals..... 62
3.12	Measured first integral field distribution along different SWLS current; the field integral were measured at TPS and SPS at $x = y = z = 0$ . .... 63
3.13	The correction coil of SWLS ..... 63
3.14	The vertical magnetic field without and with side coil along the magnet in z-axis ..... 64
3.15	Measured vertical and horizontal first integral field distribution along different trajectory on the transverse x-axis at SWLS current of 308A. . 64

## LIST OF FIGURES (Continued)

<b>Figure</b>	<b>Page</b>
3.16 The correction current coils different SWLS current; the field integral were measured at TPS in red and SPS in blue. ....	68
3.17 The first and second vertical field integral were measured at TPS and SPS. ....	69
3.18 The comparison of the measured magnetic Field as a function of length (z) at the centre of the wiggler, by SLRI and ASTEC .....	70
3.19 The pole cross section of two side poles magnetic field for $y = z = 0$ mm along x positions .....	71
3.20 Measured vertical field integral distribution along different trajectory on the transverse x-axis before and after shimming at the gap of 20 mm .....	72
3.21 The comparison of the filed integral along the horizontal axis at the gap of 20 mm, before after shimming.....	72
3.22 The comparison of the filed integral along the horizontal axis at the gap of 20 mm, before after shimming.....	74
3.23 The trajectories in the x-z plane and y-z plane of an electron beam passing through the SWLS compared different SWLS current .....	76
3.24 The trajectories in the x-z plane and y-z plane of an electron beam passing through the MPW compared between gap of 20 and 50 mm.....	77
4.1 The studied location in the tune diagram.....	82
4.2 The piecewise hard edge model of an insertion device. ....	84
4.3 Flow chart of the MAD-X calculation. ....	86

## LIST OF FIGURES (Continued)

<b>Figure</b>	<b>Page</b>
4.4 The SPS storage ring layout.....	87
4.5 SWLS installation and (b) MPW installation .....	87
4.6 Flow chart of the TRACY-II tracking .....	89
4.7 The steering magnets adjacent to two IDs. SWLS and MPW steering magnets .....	90
4.8 The top view layout for the deviated angle and position of the electron pass though an insertion device. ....	90
4.9 The SWLS (left) and the MPW (right) installed in the SPS ring.....	94
4.10 The steps were used to correct beam optics distortion using MAD-X program.....	99
4.11 The corrected quadruples and steering magnets setting in the machine using MML based on Matlab program for orbit and beam optics correction after including these insertion devices.....	100
4.12 The measured and recorded betatron tune during commissioning processes by using the spectrum analyzer. ....	100
4.13 All corrected magnets were recorded during commissioning and they were generated to functions of energy, SWLS current, and MPW gap...	101
4.14 Some of magnets values as a functions of energy, SWLS current, and MPW gap which were put in PLC program for machine operation. All operated magnets parameter were set in this program.....	102
4.15 Recorded beam lifetime and beam current on website.....	103

## LIST OF FIGURES (Continued)

Figure	Page
4.16 Measured beam profile. The beam size is calculated by the gaussian fitting.....	103
5.1 Contour plot of measured beam lifetime scan over a range of vertical and horizontal betatron tune.....	106
5.2 Tune diagram showing sum resonance lines up to and including the 4 <sup>th</sup> order.....	108
5.3 The simulated optic functions comparison between the nominal and the new optics. ....	109
5.4 Dynamic aperture of two beam optics at 1.2 GeV. Chromaticity +2, off-momentum ( $\Delta p/p = 0\%$ ).....	110
5.5 Coupling measurements of present operating point and new operating point without insertion devices .....	111
5.6 Comparison of present and new working point beam images at the same beam energy of 1.2 GeV .....	112
5.8 The tune shift at an electron beam energy of 1.0 GeV (injection) with corrected chromaticity = +2 in both planes varies to magnetic field of SWLS.....	117
5.9 The tune shift with 4.0 Tesla SWLS (red line) and 4.6 Tesla SWLS (blue line) with corrected chromaticity = +2 in vertical plane, varies to an electron beam energy .....	117
5.10 Measured and theoretical vertical tune shift as a function of magnetic field at 1.2 GeV.....	118

## LIST OF FIGURES (Continued)

<b>Figure</b>	<b>Page</b>
5.11 The tune shift after correction at various SWLS currents at 1.0 GeV.....	119
5.12 The tune shift after correction compared between simulation and measurement with 4.0 Tesla and 4.6 Tesla SWLS without as a function of the energy .....	120
5.13 The tune shift after correction at various MPW magnetic fields compared between simulation and measurement at 1.2 GeV with 4.0 Tesla SWLS and 4.6 Tesla SWLS.....	120
5.14 Tune variations after commissioning with five conditions.....	121
5.15 Betatron function effect on the 1.2 GeV SPS machine with 6.5 Tesla SWLS and 2.18 Tesla MPW.....	123
5.16 The betatron functions along the SPS storage ring with 4.0 Tesla SWLS and 4.6 Tesla SWLS before correction.....	124
5.17 The betatron functions before correction around the SPS storage ring various the magnetic fields of SWLS at 1.2 GeV.....	125
5.18 The betatron functions around the SPS storage ring with the 4.0 Tesla magnetic fields of SWLS and 2.18 Tesla MPW at 1.2 GeV before and after correction.....	126
5.19 The betatron functions before and after correction various the magnetic fields of SWLS with 2.18 MPW at 1.2 GeV.....	127
5.20 The simulated and measured beta beating along the ring with the insertion devices after commissioning at 1.2 GeV with 2.18 Tesla MPW.....	127

## LIST OF FIGURES (Continued)

<b>Figure</b>	<b>Page</b>
5.21 The simulated dynamic apertures of SWLS by using TRACY-II code with chromaticity +2 at 1.0 GeV after correction.....	130
5.22 Dynamic apertures after including IDs, chromaticity + 2, off - momentum ( $\Delta p/p = 0\%$ ) at beam energy of 1.2 GeV.....	131
5.23 The steering magnet current adjacent to SWLS vs. the magnetic field of SWLS as used in the real machine for orbit correction at 1.0GeV....	134
5.24 The steering magnet current adjacent to MPW vs. the MPW gap are used in the real machine for orbit correction at 1.2 GeV.....	134
5.25 The quadrupole strength magnets at 1.0 GeV beam energy with different the magnetic field of SWLS.....	136
5.26 The quadrupole strength magnets with 4.6 T SWLS vary to the beam energy.....	137
5.27 The quadrupole strength magnets as a function of MPW gap with 4.6 T SWLS at beam energy of 1.2 GeV.....	138
5.28 The compared quadrupole magnets currents in storage ring between simulation and setting in the machine with 4.0 Tesla SWLS+ 2.18 Tesla MPW and 4.6 Tesla SWLS+ 2.18 T MPW at 1.2 GeV beam energy.....	138
5.29 The beam emittance as a function of SWLS current in 1.0 GeV.....	144
5.30 The beam emittance with 4.0 Tesla SWLS and 4.6 Tesla SWLS as a function of a beam energy.....	144



## LIST OF FIGURES (Continued)

<b>Figure</b>	<b>Page</b>
5.31 The variation of beam emittance with MPW gap in 1.2 GeV storage ring with SWLS field are 4.0 Tesla and 4.6 Tesla.....	145
5.32 Tune diagram with 4 <sup>th</sup> resonance line, The machine operation without IDs, with 6.5 Tesla SWLS, with 2.18 Tesla MPW, with 4.0 Tesla SWLS + 2.18 Tesla MPW, and 4.6 Tesla SWLS + 2.18 Tesla MPW.....	150
5.33 Beam images for (a) with 4.0 Tesla SWLS+ 2.18 Tesla MPW (b) with 4.6 Tesla SWLS+ 2.18 Tesla MPW.....	151
5.34 The reference electron orbit in the SPS storage ring. ....	154
5.35 The close electron orbit (COD) after applying the magnetic field of insertion devices (IDs), which are corrected by all steering magnets.....	154
5.36 Beam operation windows.....	155
6.1 The machine operation with 4.0 Tesla SWLS, 2.18 Tesla MPW, and 0.55 Tesla U60 at 1.2 GeV beam energy and beam current of 117 mA..	159

# CHAPTER I

## INTRODUCTION

### 1.1 Motivation

The Siam Photon Source (SPS) is a dedicated synchrotron light source with the electron storage ring having the beam energy of 1.2 GeV. In the original design the electron energy of the storage ring was 1.0 GeV. The energy was upgraded to 1.2 GeV in 2005 (Klysubun *et al.*, 2007). The storage ring contains four Double Bend Acromat (DBA) super periods with four long straight sections. Each symmetric period consists of four focusing quadrupole magnets, three defocusing quadrupole magnets, and two bending dipole magnets. The SPS bending magnets can produce synchrotron radiation with the critical energy of 1.38 keV. At present, the bending magnet is the main source of the three photon beamlines; a photoelectron spectroscopy (PES) in the vacuum ultraviolet (VUV) spectral range, X-ray lithography (XRL), and an X-ray absorption fine-structure spectroscopy (XAFS). In order to respond to the requirement of hard X-rays synchrotron radiation from the beam line user, the Synchrotron Light Research Institute (SLRI) had installed a superconducting wavelength shifter (SWLS) and a hybrid multipole wiggler into SPS storage ring. These high-field insertion devices (IDs) can provide higher photon energy and flux density of synchrotron radiation than that of the dipole magnets. Therefore, high flux hard X-rays radiation can be obtained. The long straight sections (LSS) of the storage ring were designed to accommodate installation of the IDs. The LSS themselves have low betatron function,

resulting in a small beam cross section, small tune shift, and smaller non linear effect (Voss, 1998).

At present, high flux photons in the soft X-rays range are generated from U60 undulator (Rugmai *et al.*, 2007), which was installed in the SPS storage ring in 2008. The installations of the SWLS and MPW inevitably affect the beam optic parameters. These include the betatron tune shift, betatron function beating, emittance blow up, energy loss, and reduction of dynamic aperture, which are not preferred in the SPS operation. Therefore, these effects are studied in this research. In order to obtain the results precisely, the calculation are performed by using three different codes consist of MAD-X, AT-ROOT and TRACY-II. The effects of the insertion devices can then be successfully minimized and compensated. In this study, the energy loss per turn after installing two high field IDs is higher than that of the bare ring, and resulting in the lower lifetime. Therefore, the operating conditions should be investigated and optimized for the optimal beam lifetime.

This thesis consists of six chapters; chapter I provides information on parameters of the SPS storage ring and specifications of the IDs, which are used throughout the thesis. A literature review of accelerators, insertion devices, and beam dynamics effects is presented in chapter II. Chapter III discusses the results of field measurements and compensation of the two IDs. Research methodologies including observation operation point, simulation of beam dynamic effects, and commissioning of the IDs into SPS storage ring are given in chapter IV. In this chapter, the simulation tools are also shown. The most important results of the SPS optic simulation and commissioning are discussed in chapter V. Finally, the conclusion will be drawn in chapter VI.

## 1.2 Siam photon source

The Siam Photon Source is an electron accelerator. An electron beam is produced by thermionic electron gun emission from a heated tungsten matrix cathode then accelerated by 2856 MHz high power microwave in the linear accelerator. The 40 MeV electrons are transported by the low energy beam transport line (LBT) to the booster synchrotron which accelerates electron to 1 GeV using 118 MHz Radio Frequency wave in the RF cavity. The 1 GeV electrons are taken away by the high energy beam transport line (HBT) to the storage ring and the energy of the beam is ramped up to 1.2 GeV. The SPS scheme is shown in Figure 1.1.

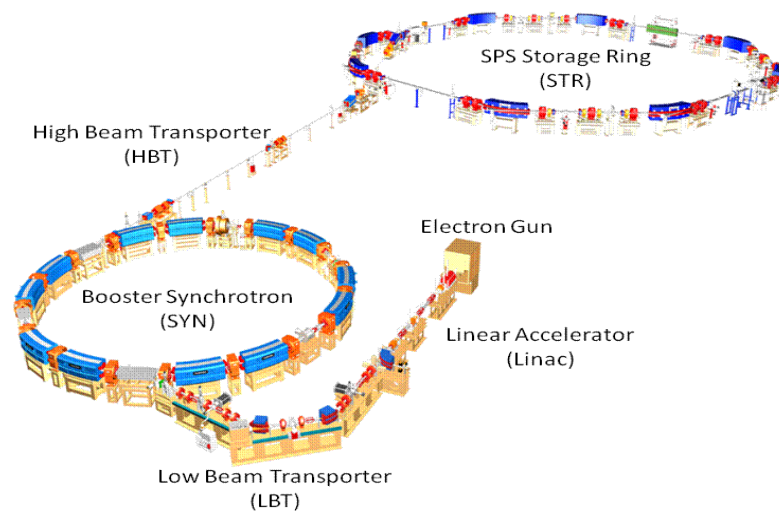


**Figure 1.1** Schematic diagram of Siam Photon Source (From [www.slri.or.th](http://www.slri.or.th)).

After ramping energy to 1.2 GeV, the electrons are stored in the ring to generate synchrotron radiation. The stored electron beam current is 150 mA. At present, the beam emittance is 61 nm-rad and the beam lifetime is approximately 11 hours at 100 mA. The storage ring is 81.3 meters in circumference. The long straight

sections have kept for the insertion devices which is a 4.4 m per section. Four of the straight sections in the storage ring are used to host 118 MHz RF cavity and insertion devices. Each sector of one superperiod consists of aluminum vacuum chambers, two dipole bending magnets where the synchrotron light is produced, seven quadrupole (divided into four families) and four sextupole magnets (separated into two families). This gives a total of 28 quadrupole and 16 sextupole magnets in the storage ring to be used for beam focusing, chromaticity corrections. An overview of the principle design of one SPS achromat is shown in Figure 1.2. There are four horizontal and three vertical steering magnets, and five beam position monitors (BPMs). Other components such as a septum magnet, the 118 MHz RF cavity, a beam current monitor, bump magnets, beam loss monitors are also installed in places around the SPS storage ring.

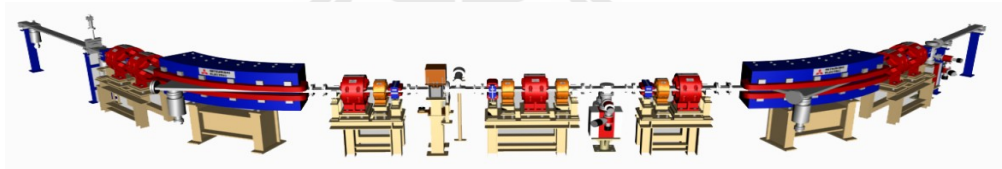


**Figure 1.2** Double Bend Acrobat (DBA) lattice for the SPS storage ring (Adapted from [www.slri.or.th](http://www.slri.or.th)).

Currently the SPS storage ring contains three insertion devices; the superconducting wavelength shifter, hybrid multipole wiggler, and undulator. The electron beam energy is lost through the bending magnet and the insertion devices where the synchrotron radiation is produced. The energy loss will be compensated when the electron passes through the RF cavity in the ring.

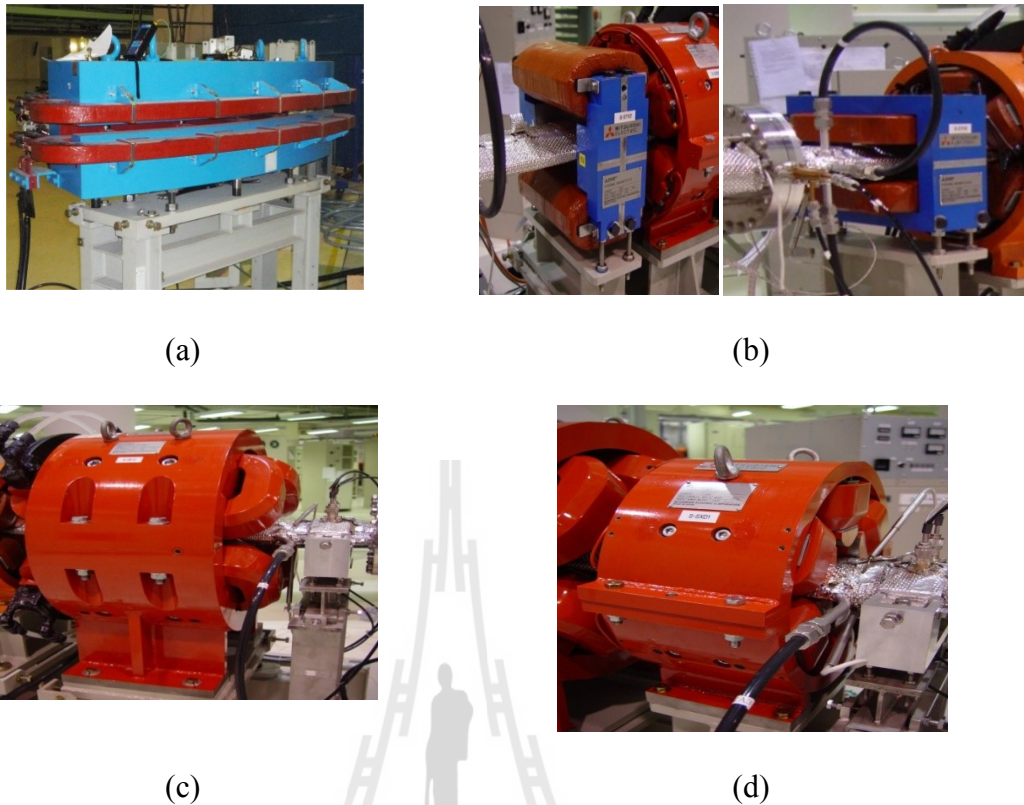


**Figure 1.3** (a) Bending magnet, (b) Steering magnet, (c) Quadrupole magnet, and (d) Sextupole magnet in the SPS storage ring (Taken from [www.slri.or.th](http://www.slri.or.th)).

There are eight bending magnets in the SPS storage ring. The bending magnets in the DBA are sector dipole magnets with a deflection angle of  $45.0^\circ$  ( $0.785398$  rad). The bending magnets field strength is 1.44 Tesla for 1.2 GeV SPS ring, corresponding to a bending radius of 2.78 m. There are four families of quadrupole magnets, QF1 and QD2 quadrupoles are original quadrupoles from SORTEC and the QF3 and QD4 are newly manufactured quadrupoles with mechanical dimensions equal to the original ones. The location of quadrupole magnet in the DBA is shown in Figure 1.2. Their parameters are listed in Table 1.1. The effective magnet lengths of all quadrupole magnets are 0.323 m.

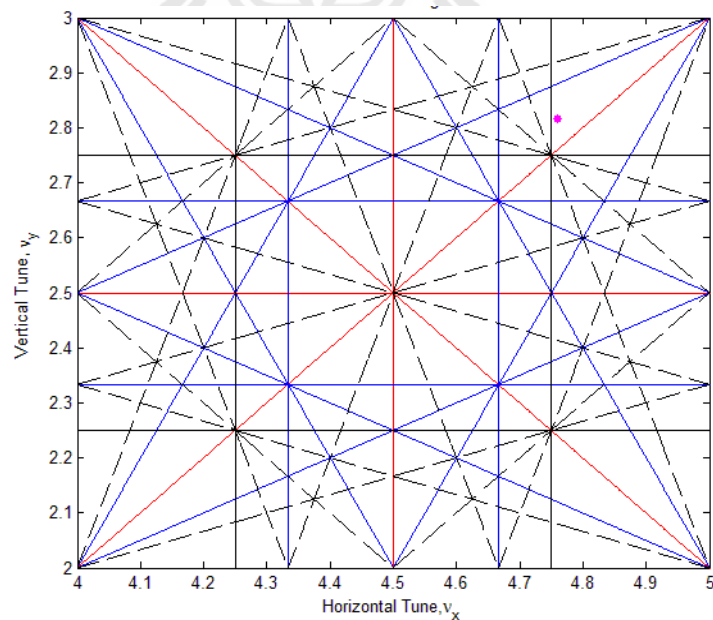
**Table 1.1** The quadrupole and sextupole magnet parameters for the bare lattice of the SPS storage ring with the emittance of 61 nm-rad.

Magnet	Number	Length	G/I slope	Strength magnet
<i>Quadrupole magnet</i>				
QF1	8	0.323 m	0.025738 T/m.A	2.4744 m <sup>-2</sup>
QD2	8	0.323 m	0.025745 T/m.A	-2.6299 m <sup>-2</sup>
QF3	8	0.323 m	0.026045 T/m.A	2.3175 m <sup>-2</sup>
QD4	4	0.323 m	0.026546 T/m.A	-1.6821 m <sup>-2</sup>
<i>Sextupole magnet, chromaticity of +2</i>				
SF	8	0.180 m	5.4733 T/m <sup>2</sup> .A	-11.446 m <sup>-3</sup>
SD	8	0.230 m	5.4885 T/m <sup>2</sup> .A	9.944 m <sup>-3</sup>

The important optical parameters of the SPS storage ring are summarized in Table 1.2. Tune diagram is a convenient way to map out the unstable tune areas as shown in Figure 1.4. In this figure, a tune diagram up to 4<sup>th</sup> order is presented and the working point of SPS storage ring is installed at the blue point 4.768 and 2.813 for the emittance of 61 nm-rad. The betatron function in a lattice is symmetric in the two planes, and reaches the maximum and minimum values in the center of the quadrupole magnets. The betatron function and dispersion function of SPS storage ring are shown in Figure 1.5.

**Table 1.2** Parameters of the SPS storage ring.

Electron energy, $E$	1.2 GeV
Circumferences, $C$	81.3 m
Lattice	DBA
Betatron tunes, $\nu_x, \nu_y$	4.768, 2.813
Betatron function in the middle of LSS, $\beta_x, \beta_y$	14.53, 2.98 m
Horizontal dispersion function, $\eta_x$	0.807 m
Natural energy spread	0.0006
Natural chromaticity, $\xi_x, \xi_y$	-8.475, -6.668
Natural emittance	61 nm-rad
Energy loss	66 keV/turn

**Figure 1.4** Tune diagram showing some resonance lines up to and including the 4th order and operating point with emittance of 61 nm-rad.



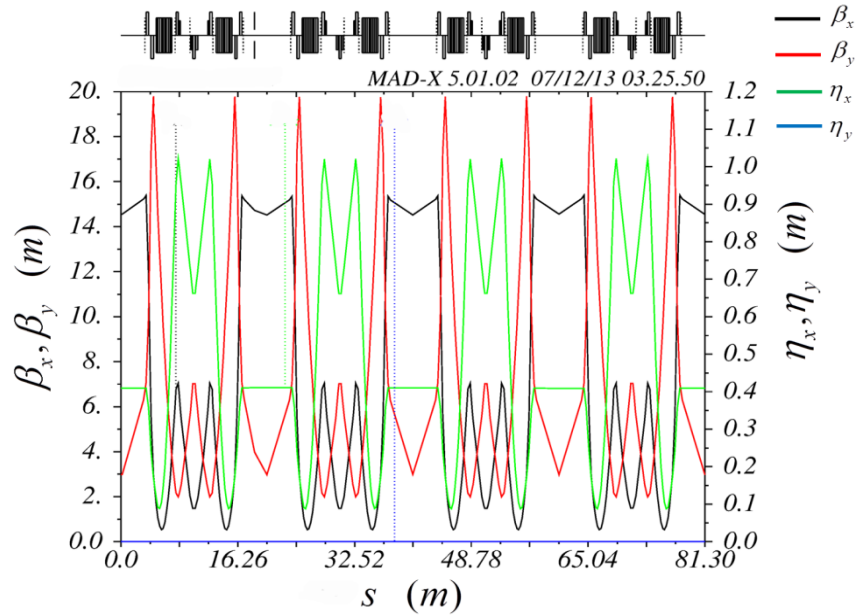


**Figure 1.5** Betatron and dispersion functions of bare ring lattice with electron beam emittance of 61 nm-rad for a 1.2 GeV SPS storage ring.

### 1.3 Insertion devices (IDs) at SLRI

An insertion device, such as wiggler and undulator has a periodic magnetic structure. The high spectrum synchrotron radiation is emitted by forcing a charged particle beam to pass through the device. A wiggler efficiently forms a continuous spectrum at higher photon energy higher than that from the bending magnets as it is a magnet with higher magnetic field. In an undulator, interference effects generates a quasi-monochromatic spectrum of the synchrotron radiation with high flux and brightness peak. Undulators have shorter periods and weaker fields. Advantages of the insertion devices (IDs) over the bending magnets include higher photon energy, higher flux, higher brightness, and different polarization characteristics. The demand of very high brightness synchrotron radiation ensures that the IDs will be used extensively in the dedicated light sources that are currently under construction.

Spectral flux from a bending magnet with 1.44 T peak field compared with a 2.18 Tesla hybrid multipole wiggler and a 6.5 Tesla superconducting wavelength shifter is shown in Figure 1.6.

High field insertion devices have been developed to obtain higher photon energy and increased photon flux of the synchrotron radiation. The critical energy of the radiation emitted from the IDs depends on the magnetic field and the beam energy of storage ring. On the other hand, the photon flux may be increased by using a large number of the magnet poles, which can be obtained in devices made from permanent magnets.

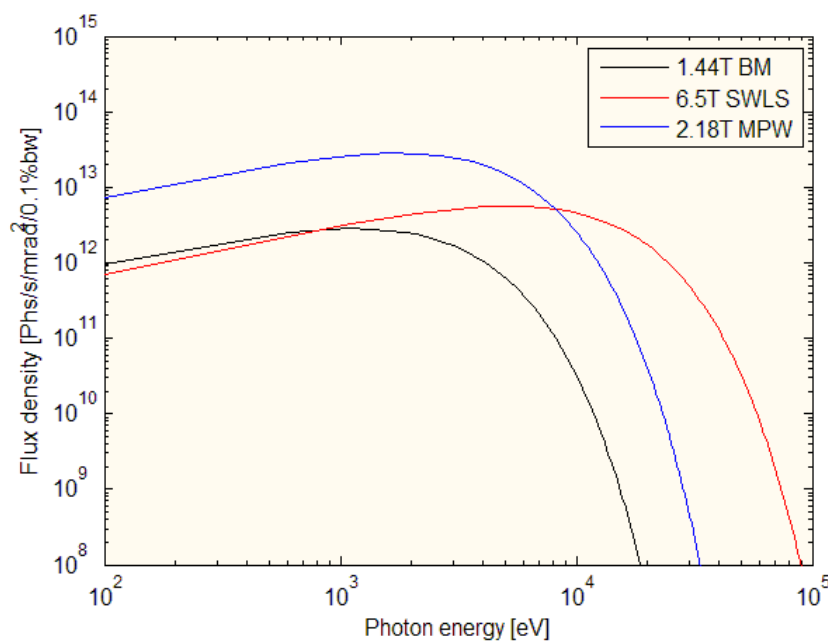


**Figure 1.6** Photon flux density generated by electron beams as a function of photon energy. The stored electron beam current is 150 mA at energy of 1.2 GeV.

Many high field insertion devices have already been installed in the synchrotron sources around the world. For example, a superconducting wiggler with 10T magnetic field was installed in SPRING-8 (Shoji *et al.*, 2003), a superconducting wiggler with 3.5T was installed in VEPP3 (Artamonov *et al.*, 1980), a 5 T superconducting wavelength shifter has been operated at SRS (Suller *et al.*, 1983), and a 6 T superconducting wavelength shifter was designed by Taiwan Light Source (Hwang *et al.*, 2005). Currently, there are two insertion devices being planned to be installed in the SPS storage ring; a 6.5 Tesla Superconducting Wavelength Shifter (Figure 1.7) and a 2.4 T Hybrid Multipole Wiggler (Figure 1.9).

The 6.5 Tesla Superconducting Wavelength Shifter (SWLS) was designed and assembled at Taiwan light source (TLS) (Hwang *et al.*, 2007). It composes of three poles. The peak field in the central pole at the maximum current of 308 A is 6.50 T while the two side poles give 4.07 T. The magnetic field profile of the device is shown in Figure 1.8. The magnetic field of several tesla can be obtained by using superconducting windings. One main power supply is connected to three pairs of the racetrack NbTi coils which are constructed with iron yokes of the three magnet poles. In addition, two low current power supplies are connected to the other two pairs of the trim coils at the side poles for field correction. Liquid helium is used for cooling of the magnet with the designed boil-off rate of 1.4 L/hr and temperature of 4.3 K.

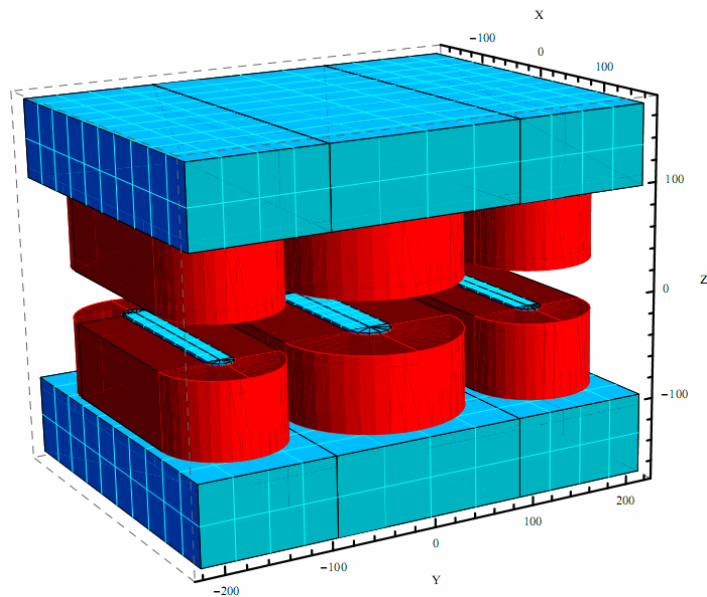
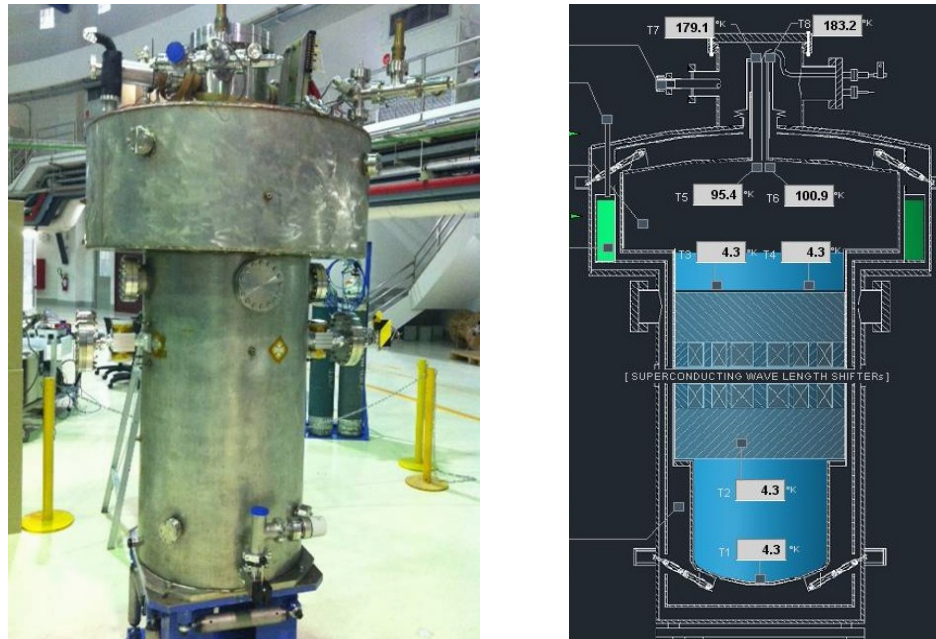
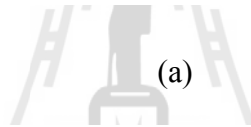
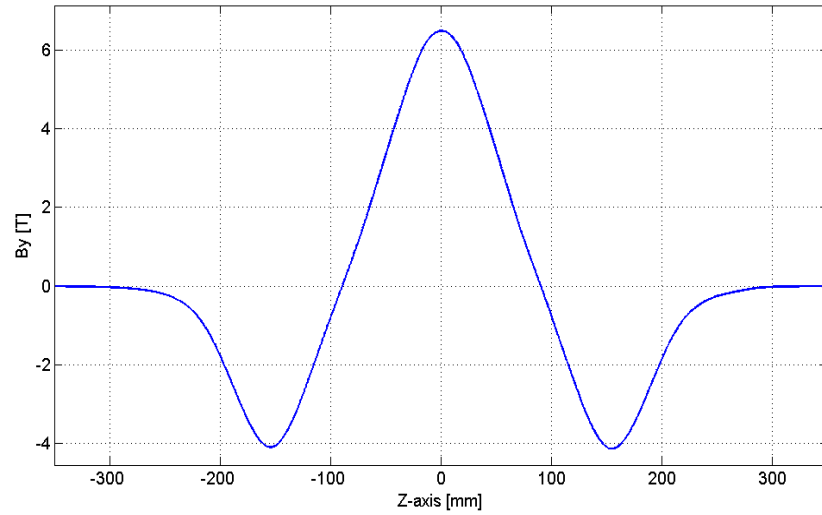


**Figure 1.7** The superconducting wavelength shifter from TLS.

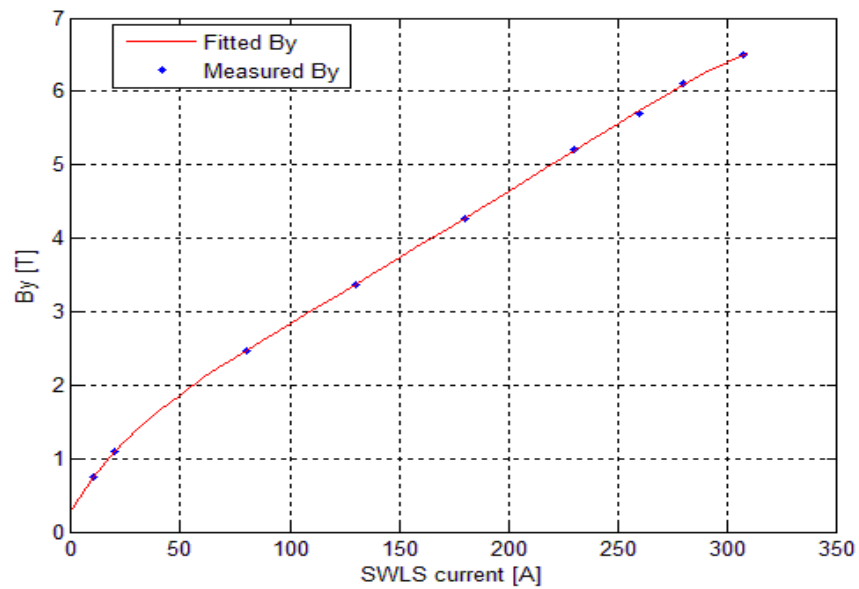
Moreover, the measured integrated quadrupole field strength is corrected by two magic finger correctors installed at each side of SWLS. Figure 1.8b shows the fitting curve in is described by

$$B(I) = -4.023E^{-14}I^6 + 4.202E^{-11}I^5 - 1.783E^{-08}I^4 + 3.923E^{-06}I^3 - 4.692E^{-04}I^2 + 4.678E^{-02}I + 0.324, \quad (1.1)$$

Where  $I$  is the SWLS current.



(a)



(b)

**Figure 1.8** (a) The measured vertical magnetic field ( $B_y$ ) at the SWLS current of 308

A along the SWLS and (b) B-I curve of SWLS.

**Table 1.3** The SWLS (Hwang *et al.*, 2005) and MPW (Clarke *et al.*, 2003) specifications.

<i>Superconducting wavelength shifter</i>	
Number of pole	3
Field at center pole, T	6.5
Field at two side poles, T	-4.1
Cu/Sc ratio	3:1
Number of filament	330
Filament diameter, $\mu\text{m}$	39
Inductance @ 6.5T, H	9.53
Total energy @ 6.5T, kJ	450
<i>Hybrid multipole wiggler</i>	
Number of pole	9
Field at nine center poles, T	2.4
Field at two side poles, T	1.29
Minimum gap, mm	20
Pole material	vanadium permendur
Permanent Magnet Material	NdFeB, Vacodym 633 HR
Pole Dimensions (W x L x H)	70 x 35 x 90 mm
Total Length of Magnet	1180 mm

The hybrid multipole wiggler (MPW) in Figure 1.9 was designed by the Synchrotron Radiation Source (SRS) and was installed in the SRS storage ring for operation at 2.0 T (Clarke, 1997). The designed peak magnetic field is 2.4 T at 20 mm magnet gap, with a magnetic period length of 220 mm. There are nine centre poles and two side poles made from vanadium permendur. NdFeB was used as permanent magnet material to achieve the maximum possible performance in terms of peak field strength, which is presented in Figure 1.10 and detailed in Table 1.3.

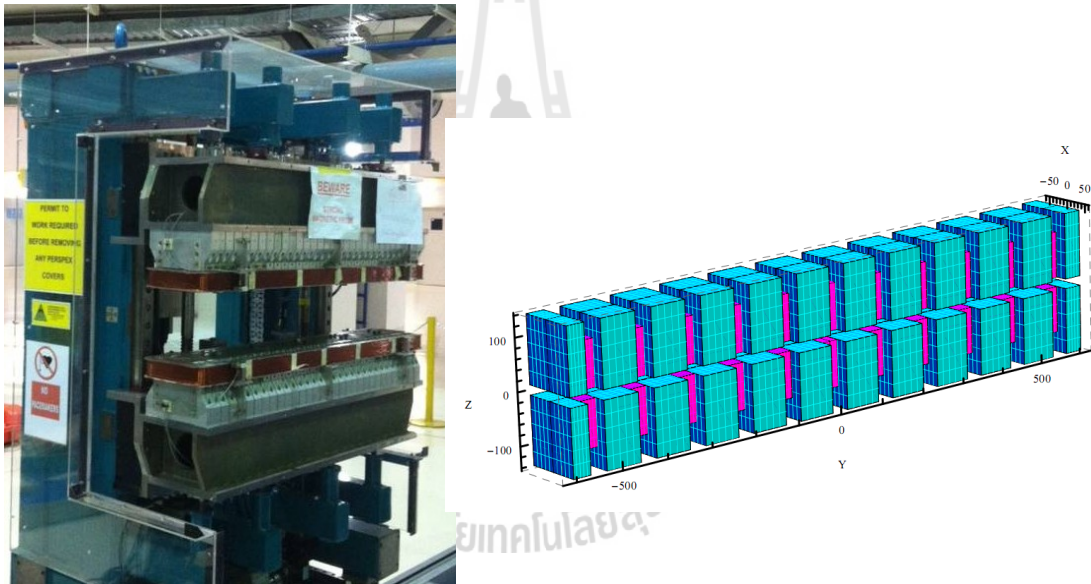


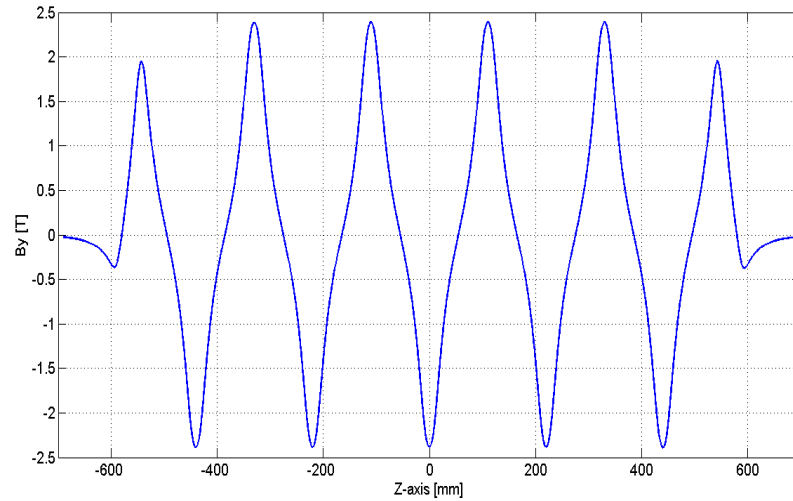
**Figure 1.9** The hybrid multipole wiggler from SRS.

The magnetic field errors, resulting from imperfect magnetic material, were minimized and compensated for shimming. The MPW had been installed into the 2 GeV SRS storage ring (Clarke *et al.*, 1999). The hard edge model was used to estimate the beam dynamics effect. The field error that cause orbit change after closing the gap is compensated for using the trim coils. The relation between magnetic field and pole gap of the MPW is shown in Figure 1.10b.

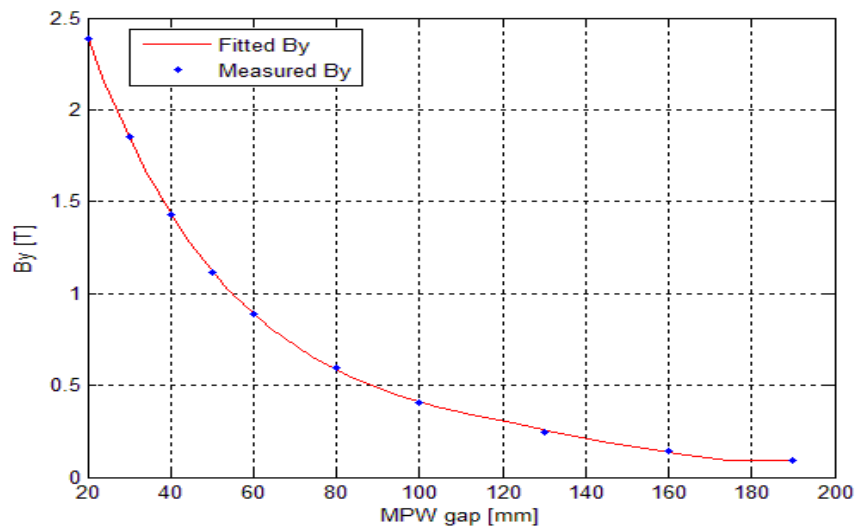
The fitted curve can be described by polynomial relation as

$$B(G) = 8.794E^{-09}G^4 - 4.761E^{-06}G^3 + 9.729E^{-04}G^2 - 9.329E^{-02}G + 3.893, \quad (1.2)$$

Where G is the MPW gap.



(a)



(b)

**Figure 1.10** (a) The vertical magnetic field ( $B_y$ ) of MPW at the gap of 20 mm along the MPW and (b) The peak magnetic field of MPW as a function of the pole gaps.



## 1.4 Review of the beam dynamics studied

The two IDs should be operated in the storage ring without disturbing the stored electron beam in the other parts of the orbit. Therefore, their effects during SPS operation are studied. Two types of the beam dynamics effects can be produced.

The linear effects include the closed orbit distortion, beam optics perturbation, breaking of the symmetry of betatron and dispersion functions, large vertical betatron shifts, increased emittance, and increased energy loss. Vertical focusing of the insertion devices will cause a tune shift and mismatch of the betatron function. For example, the vertical tune shift and beta-beating of the 2.18 Tesla multipole wiggler in 2.5 GeV PLS (Kim, 2005) were found to be 0.02 and 16%, calculated using MAD-8 program (Grote *et al.*, 1995). Changes in the emittance were found in the 3 GeV storage ring of the PLS-II where the emittance was compensated from 9.34nm-rad to 7.56 nm-rad (Hwang *et al.*, 2010) after including 20 devices. The energy loss per turn was found to increase by 23% (from 913 to 1124 keV/turn) with 7 wigglers in SPEAR3 (Corbett and Nosochkov, 1999). In this study, the vertical tune shift and emittance blow-up are investigated using the MAD-X program. Perturbations from the insertion devices will be compensated by adding and adjusting the quadrupole magnets.

The nonlinear effects (Safranek *et al.*, 2002) of the insertion devices will break the lattice symmetry of the storage ring and change the phase advances between the chromaticity correction sextupoles. These effects reduce the dynamics aperture. However, it can be compensated for by the sextupole magnets, where the compensation strengths can be calculated using programs such as BETA (Farvacque *et al.*, 1987) and TRACY-II (Bengtsson, 1997). The effects of IDs on dynamics

aperture arise from asymmetric lattice, distortion of the betatron/dispersion functions, field errors, nonlinear field effects and misalignment. In SPEAR 3, the vertical dynamics aperture reduced approximately by 20% without compensation of the vertical focusing (Corbett *et al.*, 1999). Both linear and nonlinear effects are stronger in the low energy ring.

Therefore, distortions of the lattice optics need to be compensated for and minimized in order to obtain a large dynamics aperture. The compensation schemes will be investigated using MAD-X and TRACY-II programs. Electron beam in the storage ring is also distorted by the field errors of the insertion device. In the ideal case, electrons have to exit the insertion device with the same displacement and angular deviation as they enter, meaning that the field errors of the insertion device are zero. In the case of non-zero field errors, the distortions can be compensated for by correction coils (Hwang *et al.*, 2007) or shimming technique (Clarke, 1997).

After installment, the high field insertion devices will also have an effect on the electron beam lifetime due to a high energy loss. So the method of tune scan (Laskar, 2003) will be used to analyze and used for improving the beam lifetime and dynamics aperture. Its technique is used to study working point optimization and correction resonances (Liuzzo *et al.*, 2012). This study can help in finding a better location for the betatron tunes. It is very important to achieve a large dynamic aperture and a stable electron beam orbit. The beam loss of particle is also affected by large amplitude of the tunes, and resulting of strong resonances (Riechel, 2007). For the lattices of the BEPCII storage ring (Jiao *et al.*, 2007); the operating points are 6.51/5.58 for the horizontal and vertical tunes, respectively. The horizontal operating tune is very close to the half integer resonance so the nonlinear optimization term or

dynamics aperture of the lattice is reduced. The working point of BEPCII lattice is moved to 6.57/5.61 of the horizontal and vertical tunes, respectively obtained with Frequency Map Analysis (FMA) (Reichet, 2007), which is located in a stable location, larger and better beam dynamic. This method can confirm that the dynamics aperture of BEPCII lattice is bigger than the lattice without optimization by using the SAD code (Oide, 1997). The dynamic aperture is also calculated using BETA and TRACY-II (Attal *et al.*, 2013; Chiu *et al.*, 2012). The optimizations of lattice with frequency map was found to be a good and effective tool of the beam dynamics and the resonance structure. The beam lifetime is effected by the tune location and the optics distortion caused by the insertion devices (Feikes *et al.*, 2003). In BESSY II, the beam lifetime are decreased after installing insertion devices so they have observed the tune location for increasing beam lifetime.



## **1.5 Research objectives**

In this thesis, a method for commissioning and operation of the high field insertion devices (superconducting wavelength shifter and hybrid multipole wiggler) for the Siam Photon Source (SPS) storage ring is presented. The three main goals were as follows:

- 1.5.1 To calculate and compensate for the beam dynamics effects introduced by high-field insertion devices in the SPS storage ring.
- 1.5.2 To find the operating conditions of SPS storage ring with the high field insertion devices.
- 1.5.3 To optimize and improve the SPS optics of the bare ring after installing the MPW and SWLS.

## **1.6 Scopes and limitations of the study**

- 1.6.1 This study focuses on the calculation and compensation scheme for the beam dynamics effects of the SPS storage ring after installing the Superconducting Wavelength Shifter (SWLS) and Hybrid Multipole Wiggler (MPW) using MAD-X, TRACY-II, and Matlab Middle Layer (MML) based on MATLAB.
- 1.6.2 Optimization and investigation of the SPS optics after installing the MPW and SWLS are performed to explore whether there is a better location in the tune space that may increase the beam lifetime.

## CHAPTER II

# THEORY OF ACCELERATOR BEAM DYNAMICS AND INSERTION DEVICES EFFECTS

This chapter introduces the accelerator beam dynamics theories which are used throughout this thesis. They are separated into four parts consisting of synchrotron light source, review of insertion device, effects of insertion devices on beam dynamics, and the effect due to the emission of synchrotron radiation.

### 2.1 Synchrotron light source

#### 2.1.1 Particle motion and accelerator magnets

The electron orbit in the storage ring, the synchrotron radiation (SR), is produced from bending magnets. The bending magnet is a two poles magnet that generates uniform magnetic field. From the Lorentz force law, relativistic electron circular path is bent by the bending magnet field. The SR beam was emitted from the accelerated electron particles in bunch. The force is perpendicular to the plane form by the electron motion and the magnetic field. The force is found by a charged particle when moving in a magnetic field. Electron moves with velocity  $\vec{v}$  in an electric field  $\vec{E}$  and a magnetic field  $\vec{B}$  as follows

$$\vec{F} = e(\vec{E} + \vec{v} \times \vec{B}) \quad (2.1)$$

Where  $e$  is the electron charge.

Therefore, it can be rewritten as

$$\frac{1}{\rho} = \frac{e}{P} B = \frac{ec}{\beta E} B, \quad \beta = v/c \quad (2.2)$$

with  $\rho$  is the bending radius in meter,  $B$  is the bending magnetic field in Tesla, and  $E$  is the beam energy in GeV.

For the storage ring, the main beam elements are the drift space, dipole magnet, quadrupole magnet.



1. *The drift space:* The drift space refers to parts of the storage ring vacuum chamber where there is no magnetic component. An electron which passes through the drift spaces can move without any force.

2. *Bending magnet:* The bending magnet (BM) is a general dipole magnet and the function of this magnet is to bend the electron beam in the storage ring. Electrons passing through a bending magnet experience a constant Lorentz force, and move along a circular path. The electron energy  $E$ , the magnetic field  $B$ , and the radius of curvature  $\rho$  are related by the equilibrium between the Lorentz force and the centrifugal force by

$$\frac{\gamma m v^2}{\rho} = e v B \quad (2.3)$$

$$E[\text{GeV}] = 0.2998 B \rho, \quad (2.4)$$

Where assume relativistic electron,  $v/c \approx 1$ . The term of  $B\rho$  is called beam rigidity in T.m.

3. *Quadrupole magnet:* The quadrupole magnet (QM) has four magnetic poles. It generates magnetic field with magnetic flux density varying along the distance from

the magnet center. According to the Coulomb's law, the forces among electrons can cause the beam to spread out far from the center. Thus, this magnet is used to focus the electron beam. The quadrupole therefore functions as a magnetic lens focusing electrons. There are two families of quadrupoles. One is called "a focusing quadrupole" and the other is called a "defocusing quadrupole".

In the center of QM, there is a magnetic field free region. The magnetic potential in QM is described by

$$V = -gxy \quad (2.5)$$

Where  $g$  is the quadrupole gradient,  $x$  and  $y$  are horizontal and vertical positions transverse to the beam path. The magnetic fields of QM in horizontal and vertical plane are defined by

$$B_x = -\frac{\partial V}{\partial x} = gy \quad (2.6)$$

$$B_y = -\frac{\partial V}{\partial y} = gx \quad (2.7)$$

The field gradient ( $g$ ) and focusing strengths ( $k$ ) of quadrupole are given by

$$g = 3.3355 \frac{E}{f \cdot L_{eff}}, \quad f = \frac{1}{k \cdot L_{eff}} \quad (2.8)$$

$$k = \frac{g}{B\rho} \quad (2.9)$$

Where  $f$  is the focal length and  $L_{eff}$  is the effective length of QM.

4. *The sextupole magnet:* The sextupole magnet (SM) is composed of six magnetic poles as presented in Figure 2.3. The magnetic field of the sextupole is quadratic along the transverse coordinates. It is designed to improve the chromatic aberration because electrons having different energies are focused differently by the

quadrupole field. The focusing of electron beam and correction of chromatic aberration are causes of the electron oscillation around the reference or ideal orbit.

The SM will focus higher energy electrons and defocuses lower energy electrons.

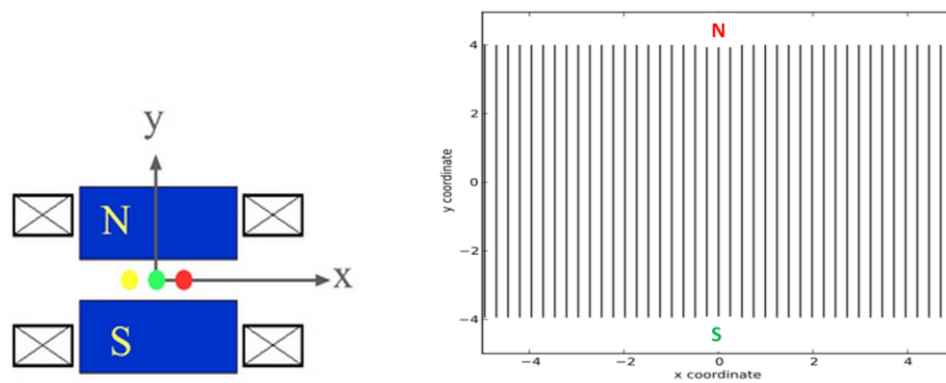


**Figure 2.1** Bending magnets.

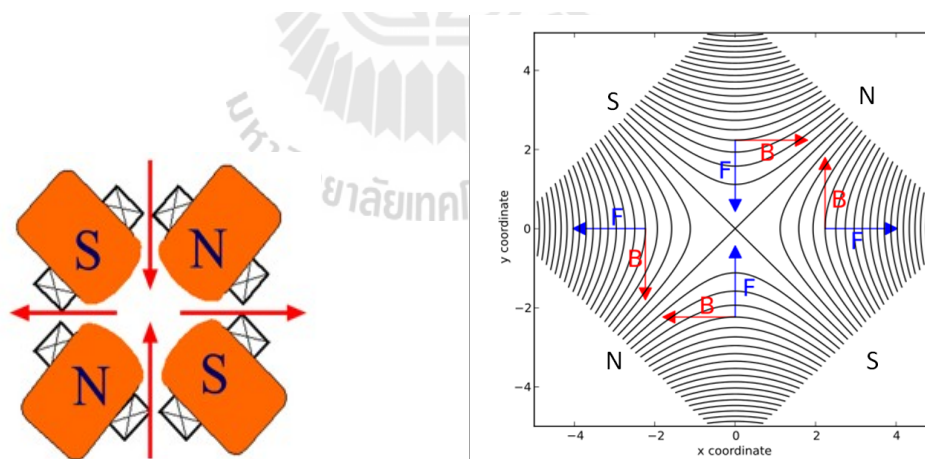


**Figure 2.2** Defocusing quadrupole magnets.



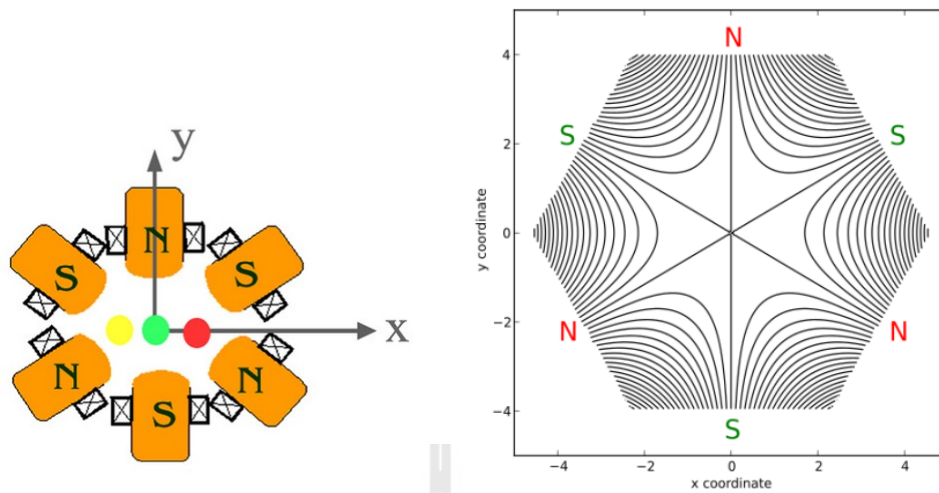


**Figure 2.3** Focusing sextupole magnets.

(The magnet pictures are adapted from <http://www.slri.or.th> and [www.wikipedia.org](http://www.wikipedia.org).)

The magnetic fields of sextupole magnet are given by

$$B_x = \frac{\partial^2 B_y}{\partial x^2} xy \quad (2.10)$$

$$B_z = \frac{1}{2} \frac{\partial^2 B_y}{\partial x^2} (x^2 - y^2), \quad (2.11)$$

## 2.1.2 Beam parameters

### Beam oscillation

This transverse oscillation is called *betatron oscillation* which occurs in the transverse plane to the electron beam trajectory. The betatron oscillations in horizontal and vertical planes will be defined from the equations of motion. In an ideal storage ring, all the magnets are perfectly aligned the orbit is the longitudinal path along the vacuum chamber of the storage ring. On the ideal orbit the beam therefore goes

through the centers of all the quadrupole and sextupole magnets. The only magnetic field experienced by the electrons moving along the ideal orbit is the dipole field of the bending magnets.

In case of the error is equal to zero  $\Delta p/p_0 = 0$ , the Hill differential equation describes beam oscillation as

$$x''(s) + K(s)x = 0 \quad (2.12)$$

From Equation 2.13, the betatron oscillation called the solution of beam position in storage ring can be expressed as

$$x(s) = \sqrt{\varepsilon} \sqrt{\beta(s)} \cos(\Phi(s) - \Phi_0) \quad (2.13)$$

Where  $\beta(s)$  is the betatron function with the length of the ring  $L$ ,  $\beta(s+L) = \beta(s)$  and  $\sqrt{\varepsilon} \sqrt{\beta(s)}$  describes an envelop and beam size of the beam oscillation.  $\Phi(s)$  is phase space of electron trajectory in the storage ring.

$$\Phi(s) = \int_s \frac{1}{\beta(s)} ds \quad (2.14)$$

The electron in phase space is called phase ellipse (see Figure 2.4). The phase ellipse can be defined by

$$\varepsilon = \gamma x^2 + 2\alpha x x' + \beta x'^2 \quad (2.15)$$

The  $\alpha, \beta, \gamma$  parameters are called the Twiss parameters and  $\varepsilon$  is the beam emittance.

Twiss parameters are related by

$$\alpha = -\frac{\beta'}{2}, \quad \gamma = \frac{(1 + \alpha^2)}{\beta} \quad (2.16)$$

In storage rings area in phase space is constant to be determined by Liouville's theorem. The betatron function is shape of phase ellipse parameter.

The beam size can be calculated from

$$\sigma_x = \sqrt{\varepsilon_x \beta_x + (\eta_x \Delta E / E)^2} \quad \text{and} \quad \sigma_y = \sqrt{\varepsilon_y \beta_y} \quad (2.17)$$

with the horizontal dispersion function  $\eta_x$ .

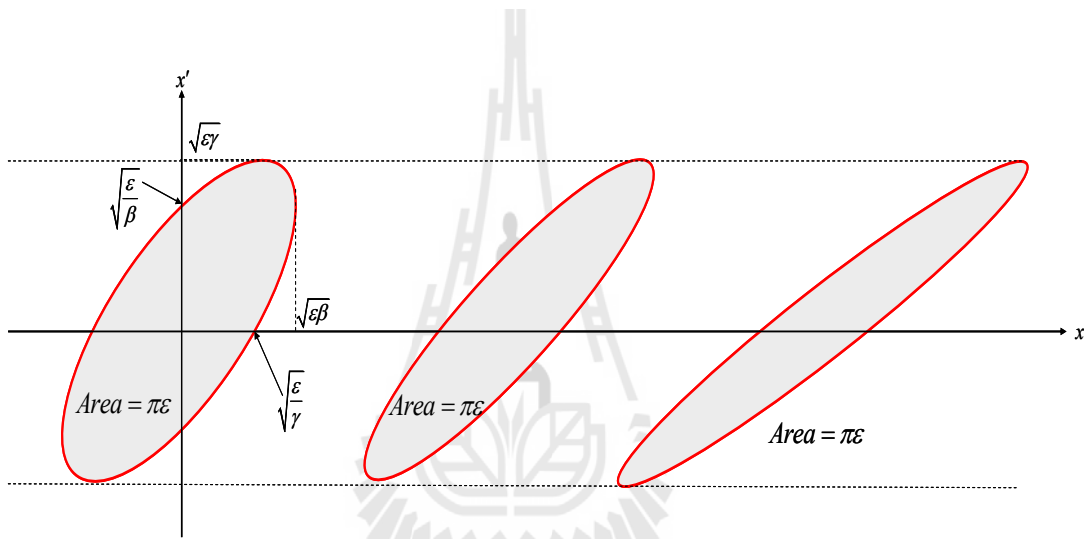


**Figure 2.4** Shape of the phase space ellipse depend on the Twiss parameters.

### Betatron tune

One important parameter is the number of oscillations per turn in a circular accelerator that the particle makes around the design trajectory. This is called the betatron tune or the operating point. The beam operating point is determined by the tune location in resonance diagram as presented in the chapter I. It can be given by

$$\nu_{x,y} = \frac{1}{2\pi} \int_0^s \frac{1}{\beta_{x,y}(s)} ds. \quad (2.18)$$

Where  $\beta(s)$  is betatron function.

The resonance lines on the tune diagram are given by below equation

$$mv_x + nv_y = k. \quad (2.19)$$

Where  $m$ ,  $n$  and  $k$  are integers,  $v_x$  and  $v_y$  are the horizontal and vertical tunes. If the integer  $k$  is a multiple of the machine periodicity then the resonance is called “systematic” and can be more risky than the others. Since the high order resonances are more out of the danger than that of small order, the integer, half-integer and third-integer resonance are the most serious ones which should be avoided. The resonance line in tune diagram can be drawn as the functions presented in Table 2.1.

**Table 2.1** Resonance lines and the driving forces up to 5<sup>th</sup> order.

Order	Driving multipole	Resonance line caused by normal multipole	Resonance line caused by skewed multipole
Integer	Dipole	$v_x = k$	$v_y = k$
Half integer	Quadrupole	$2v_x = k, 2v_y = k,$	$v_x \pm v_y = k$
Third integer	Sextupole	$3v_x = k, v_x \pm 2v_y = k$	$2v_x \pm v_y = k, 3v_y = k$
Fourth integer	Octupole	$4v_x = k, 2v_x \pm 2v_y = k$ $4v_y = k$	$3v_x \pm v_y = k$ $v_x \pm 3v_y = k$
fifth integer	Decapole	$5v_x = k, 3v_x \pm 2v_y = k$ $v_x \pm 4v_y = k$	$5v_x \pm v_y = k, 3v_x \pm 3v_y = k$ $v_x \pm 5v_y = k$

### Dispersion function

The dipole magnet sends the particles to different trajectories, according to their momentum if particles have different momentum (energy) ( $\Delta p/p$ ). The particles will require a large circumference with larger momentum, on which they can move inaccurately. A particle with  $\Delta p \neq 0$  satisfies the inhomogeneous Hill's equation in the horizontal plane

$$x'' + K(s)x = \frac{1}{\rho} \frac{\Delta p}{p} \quad (2.20)$$

The deviation of the particle is

$$x = \eta(s) \frac{\Delta p}{p} + x(\beta) \quad (2.21)$$

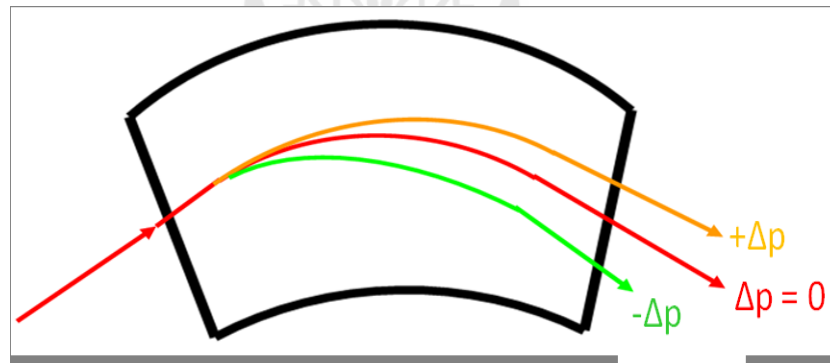


**Figure 2.5** The change momentum of electron particle when passes through the bending magnet.

The dispersion function  $\eta(s)$  is defined by the focusing properties of the ring lattice. An electron motion is similar to the ideal orbit with zero displacement for an arbitrary number of turns. Then the dispersion function can be satisfied by Hill's equation. It is given by

$$\eta'' + K(s)x = \frac{1}{\rho(s)} \quad (2.22)$$

with

$$\eta(s) = \frac{\Delta x}{\Delta p / p} = \frac{\Delta x}{\delta} \quad (2.23)$$

### Chromaticity

If electrons in a bunch do not have the same energy then QM could not focus all of them into the focusing point. Because the focusing and defocusing of each electron in the bunch is different the betatron oscillation of each electron is also different caused by the energy shift called “chromatic aberration” (Wiedemann, 1993). This is illustrated in the Figure 2.6.

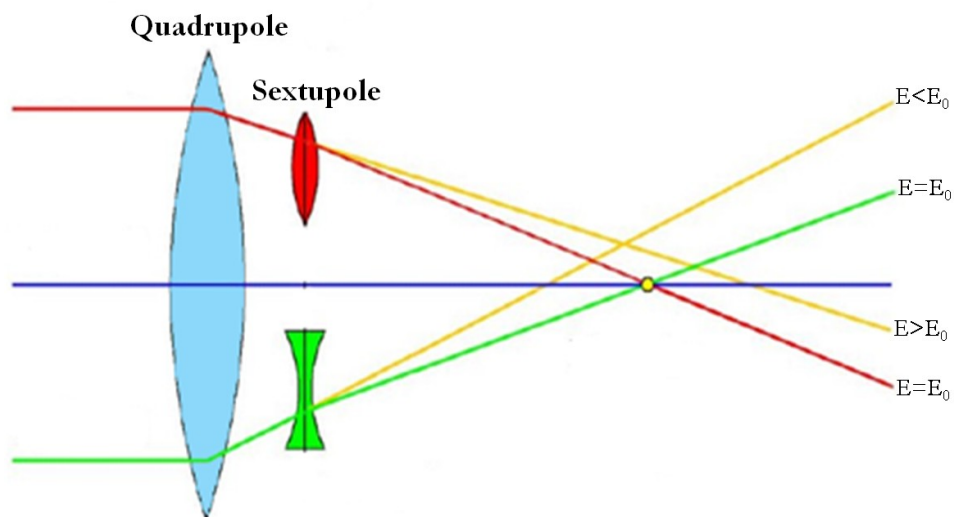


**Figure 2.6** The correction of chromatic effects.

If the electrons are not focused at the same point, it results in the betatron tune shift ( $\Delta\nu$ ). Therefore, the chromaticity can be calculated as shown in this equation

$$\xi = \Delta\nu \frac{p}{\Delta p_0} \quad (2.24)$$

The different tune ( $\Delta\nu$ ) is defined by

$$\Delta\nu = \frac{1}{4\pi} \oint k \quad \text{with} \quad k = \frac{\Delta g}{B\rho} \quad (2.25)$$

Where  $\Delta g$  is the change of field gradient of quadrupole magnet.

### 2.1.3 The transformation matrix

The transformation matrix (Wiedemann, 2003) is used to calculate and estimate the position and angle of electron motion in the storage ring. The solution of each element is

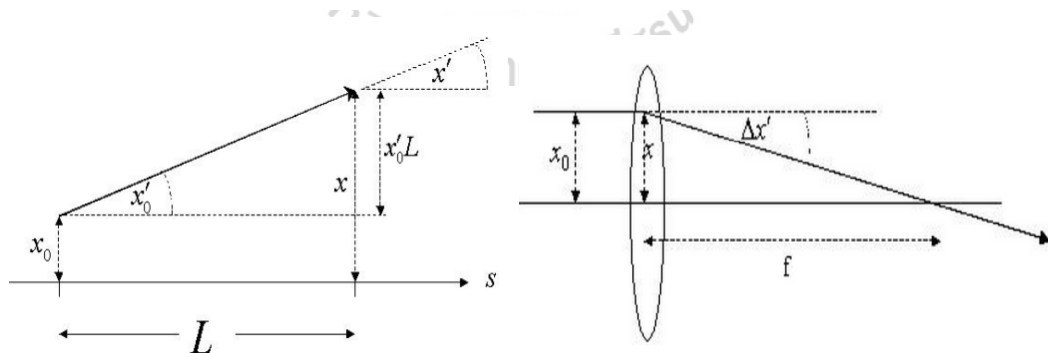


**Figure 2.7** An electron trajectory when pass through along the drift space (left) and quadrupole magnet (right) (From [www.slri.or.th](http://www.slri.or.th)).

1. *Drift space:* In a drift space of length  $L$ , the focusing parameter  $K(s) = 0$ .

From the figure 2 the solutions of electron position and deviation are given by

$$x = x_0 + x'_0 L \quad \text{and} \quad x' = x'_0 \quad (2.26)$$

The transformation can be written as

$$\begin{bmatrix} x(s) \\ x'(s) \end{bmatrix} = \begin{bmatrix} 1 & s \\ 0 & 1 \end{bmatrix} \begin{bmatrix} x_0 \\ x'_0 \end{bmatrix} \quad (2.27)$$

2. *Dipole magnet:* In case of dipole the transformation can be expressed as

$$\begin{bmatrix} x(s) \\ x'(s) \end{bmatrix} = \begin{bmatrix} \cos(s/\rho) & \rho \sin(s/\rho) \\ -1/\rho \sin(s/\rho) & \cos(s/\rho) \end{bmatrix} \begin{bmatrix} x_0 \\ x'_0 \end{bmatrix} \quad (2.28)$$

3. *Quadrupole magnet:* The transformation matrix of quadrupole magnets with strength  $K(s)$  are positive for focusing and negative for defocusing are given by

$$\begin{bmatrix} x(s) \\ x'(s) \end{bmatrix} = \begin{bmatrix} \cos \sqrt{K}s & 1/\sqrt{K} \sin \sqrt{K}s \\ -\sqrt{K} \sin \sqrt{K}s & \cos \sqrt{K}s \end{bmatrix} \begin{bmatrix} x_0 \\ x'_0 \end{bmatrix}, \quad \text{for } K = |K| \quad (2.29)$$

$$\begin{bmatrix} x(s) \\ x'(s) \end{bmatrix} = \begin{bmatrix} \cosh \sqrt{|K|}s & 1/\sqrt{|K|} \sinh \sqrt{|K|}s \\ \sqrt{|K|} \sinh \sqrt{|K|}s & \cosh \sqrt{|K|}s \end{bmatrix} \begin{bmatrix} x_0 \\ x'_0 \end{bmatrix}, \quad \text{for } K = -|K| \quad (2.30)$$

If the quadrupole magnet as thin lens, the electron trajectory can be simply obtained as

$$x = x_0 \quad \text{and} \quad x' = -\frac{x_0}{f} + x'_0 \quad (2.31)$$

With the focal length of  $f = \frac{1}{k \cdot l}$ , the quadrupole strength  $k$  and the thickness  $l$ .



### 2.1.4 Beam lifetime

In a storage ring, the stored electron beam current gradually decreases because of the limitation of aperture. There are four major phenomena outstanding to beam lifetime (Huang and Corbett, 2010; Wiedemann, 1999) consisting of the photon emission (quantum lifetime), the collisions between electrons in the same bunch (Touschek scattering), between electrons and residual gas atoms called the elastic collisions or Coulomb scattering, and inelastic collisions between electrons and residual gas atoms (Bremsstrahlung). The total beam lifetime can be taken from the four loss mechanisms according to

$$\frac{1}{\tau} = \frac{1}{\tau_{\text{touschek}}} + \frac{1}{\tau_{\text{quantum}}} + \frac{1}{\tau_{\text{elastic}}} + \frac{1}{\tau_{\text{inelastic}}} \quad (2.32)$$

1. *Intra-beam scattering (Touschek lifetime)*: The collision between the electrons in the beam cause momentums transfer between them. The particle will run into the aperture of the chamber and be lost, if the momentum deviation is much more than the limitation of RF acceptance. The low emittance results to the high bunch densities and it lead to a rate of collisions between electrons within the electron bunch. Because of the Touschek lifetime dependence on the electron density in the bunch. Therefore, it can be written in term of the bunch volume, the bunch current, and the energy acceptance and is given by

$$\tau_{\text{touschek}} = \frac{8\pi\sigma_x\sigma_y\sigma_z\gamma^2\delta_{RF}^3}{cNr_e^2D(v)} \quad (2.33)$$

Where  $\sigma_x, \sigma_y,$  and  $\sigma_z$  are the bunch average dimensions,  $\gamma$  is the relativistic factor,  $\delta_{RF}$  is the energy acceptance, N is number of particles per bunch,  $r_e = 2.82 \times 10^{-15}$  m is the

classical electron radius,  $c$  is the speed of light,  $D(\nu)$  is the smooth dimensionless function of  $\nu$ .

2. *Quantum lifetime:* The quantum lifetime is the emission of synchrotron radiation. The electron bunches have a three dimensional distribution as a result of quantum emission and radiation damping. Its distribution will be truncated by the beam acceptance, leading to beam losses. The electron beam lifetime due to the quantum character of synchrotron radiation can be computed using the following equations:

$$\tau_{\text{quantum}} = \frac{\tau_x}{2} \frac{e^{s^2}}{\xi^2}, \quad \xi_t = (A/\sigma)^2 / 2 \quad (2.34)$$

Where  $\tau$  is the damping time,  $A$  is the transverse acceptance of the beam for the transverse case and the RF acceptance for the longitudinal case,  $\sigma$  is the emittance and energy spread for the transverse and longitudinal cases, respectively. The RF amplitude is chosen to be high enough for the energy loss compensation and assigned energy acceptance for the stored electron beam.

3. *Elastic residual gas scattering (Coulomb Scattering):* This lifetime is determined by the scattering process of the electron beam by the residual gas molecules inside the chamber which depend on the pressure inside the vacuum chamber. In which the beam electron is deflected elastically by the nuclei of the gas molecules resulting in increasing the amplitudes of beam oscillation of the deflected electron. The electron beam is lost because of dynamic aperture limits. The beam lifetime for the residual gas pressure is given by

$$\frac{1}{\tau_{elastic}} = \frac{2\pi n_g r_e^2 Z^2 c}{\gamma^2} \left\{ \frac{\langle \beta_x \rangle \beta_{x,max}}{a^2} + \frac{\langle \beta_y \rangle \beta_{y,max}}{b^2} \right\} \quad (2.35)$$

Where  $c$  is the light speed,  $n_g$  is the residual gas density,  $r_e$  is the classical electron radius,  $Z$  is the atomic number of the residual gas,  $\langle \beta \rangle$  is the average beta function,

$\beta_{max}$  is the maximum betatron function,  $a$  and  $b$  are the limiting aperture.

4. *Inelastic scattering (Bremsstrahlung)*: Inelastic scattering is an effect of deceleration and photon emission due to beam collisions with the residual gas atoms or energy transfer to the other molecules. If the electron go out of the RF acceptance may also lead to the energy loss. The electron scattering will oscillate from the ideal closed orbit, which increases the betatron amplitudes in non-zero dispersion straight sections. The lifetime due to Bremsstrahlung is given by

$$\frac{1}{\tau_{inelastic}} = \frac{16r_e^2 Z^2 c \rho}{411} \ln \frac{183}{\sqrt[3]{Z}} \left( \ln \frac{1}{\delta_{RF}} - \frac{5}{8} \right) \quad (2.36)$$

## 2.2 Review of insertion device

### 2.2.1 Characteristics of insertion devices

An insertion device (ID) is a periodic magnetic field structure designed to produce the electron trajectory and generate intense synchrotron radiation. It is room into the long straight sections of storage ring. The motions of electron particles pass through insertion device are caused by the Lorentz force. Their trajectory oscillates in a transverse plane with movement stimulates the emission of synchrotron radiation. There are two types of device, which are known as wigglers and undulators, classified by the deflection parameter,  $K$  (Wiedemann, 2003),

$$K = \frac{eB_0}{mc} \frac{\lambda_p}{2\pi} = 0.934B_0[T]\lambda_p[cm] \quad (2.37)$$

Where  $\lambda_p$  and  $B_0$  are the period length of magnetic field and the peak magnetic field, respectively.

If  $K$  is small ( $K \ll 1$ ), the device is called undulator, if  $K$  is large ( $K \gg 1$ ), it is called wiggler. For a wiggler the critical photon energy of the emitted radiation depends on the strength of magnetic field, and is given by

$$\varepsilon_c[keV] = 0.665B \cdot E^2 \quad (2.38)$$

Where  $B$  and  $E$  are the magnetic field of the insertion device in Tesla and beam energy of the storage ring in GeV. A high field device can therefore produce hard X-ray for a low energy ring. The high photon flux (number of photon per second) can also be obtained with a multi-pole wiggler, since the flux is proportional to the number of the poles (Brown *et al.*, 1983). The maximum angular deflections angle are  $\pm K/\gamma$  and  $\pm K/\gamma\sqrt{N}$  for wiggler and undulator, respectively.

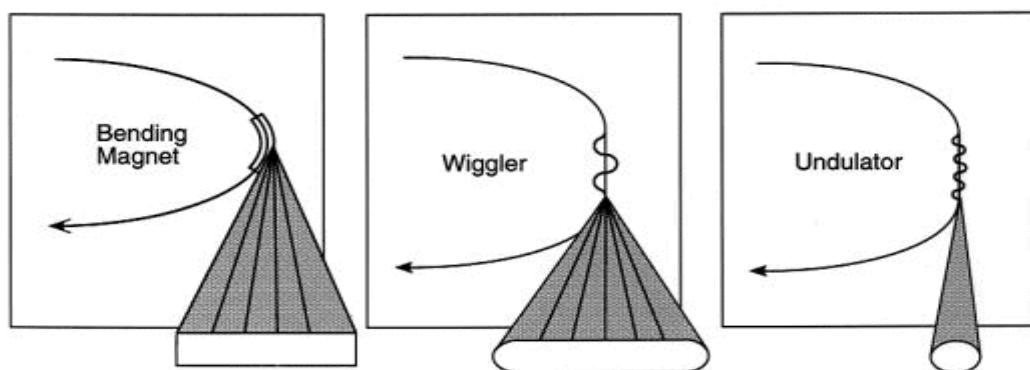


**Figure 2.8** The synchrotron radiation emitted from an electron beam by bending wiggler, and an undulator (Hitchcock and Neville, 1999).

In this research, two insertion devices which are the superconducting wavelength shifter and the hybrid multipole wiggler, will be detailed.

1. *Superconducting Wavelength Shifter:* This device magnet consists of a high field central pole and two side poles. This technology is used with superconducting magnet particularly in low energy rings. It can extend the photon energy in hard X-ray region. The critical photon energy can be chosen by adjusting the magnetic field of device magnet. The three-pole magnetic system (see Figure 2.9) consists of an iron yoke with three superconducting poles. They are placed above and below of the vacuum chamber. The important element of superconducting wavelength shifter is the central pole which has high field superconducting racetrack.

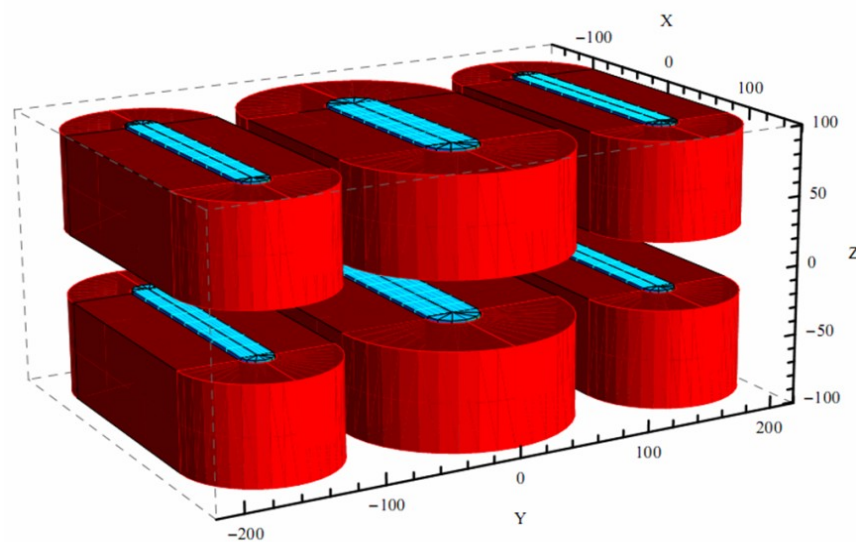


**Figure 2.9** The coils (red), iron pole (blue) on top view used in the superconducting wavelength shifter.

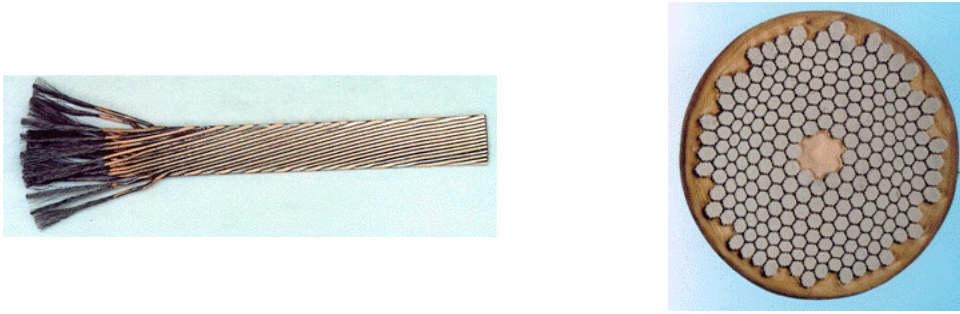


**Figure 2.10** The cable and cross-section of NbTi wires which are made superconducting coils (Taken from <http://www.cus.cam.ac.uk/~bag10/LHC.html>).

Normally, the superconductor is used in the superconducting magnets of NbTi. NbTi was selected because of it is not sensitive to stress although the Nb<sub>3</sub>Sn has higher magnetic field. The operating temperature of NbTi superconducting is 4.2 K in helium liquid. The superconductors are made in form of filamentary composites. They are embedded in the matrix of OFHC copper (see Figure 2.10). The filament diameter should be less than 60 μm due to dynamic stability (Wilson, 1983) and the critical temperature of NbTi conductor can be estimated from (Lubell, 1983)

$$d < \sqrt{8} \cdot \sqrt{\frac{k(T_c - T_0)(1 - \lambda)}{\lambda J_c^2 \rho}} \quad (2.39)$$

$$T_c = 9.2 \left[ 1 - \left( \frac{B}{14.5} \right) \right]^{0.59}, \quad (2.40)$$

Where the thermal conductivity  $k$ , the cryogenic temperature  $T_0$ , the volumetric proportion of superconductor in a composition  $\lambda$ , the resistivity  $\rho$ , the current density  $J_c$ , and the magnetic field of superconducting magnet  $B$ .

2. *Hybrid Multipole Wiggler*: The hybrid magnets consist of the permanent magnets and soft ferromagnetic materials, which was discovered by Dr. Klaus Halbach for accelerator applications (Onuki *et al.*, 2003). Then, the hybrid magnets

are designed to use in accelerator devices, such as undulators and wigglers. For very strong fields are generated a continuous spectrum from IR to hard X-rays. Compared to bending magnet radiation, wiggler radiation is enhanced by the number of magnet poles and is well collimated within an angle of  $K/\gamma$ .

Two types of structure magnets are drawn in Figure 2.11. The electron beam particles experience in the middle of the magnetic gap between the upper and the lower magnet arrays. The magnetic field gradient is formed by the combination of permanent magnets and soft ferromagnetic steel poles. Each array of magnet is alternately built soft ferromagnetic steel poles with blocks of permanent magnet material.

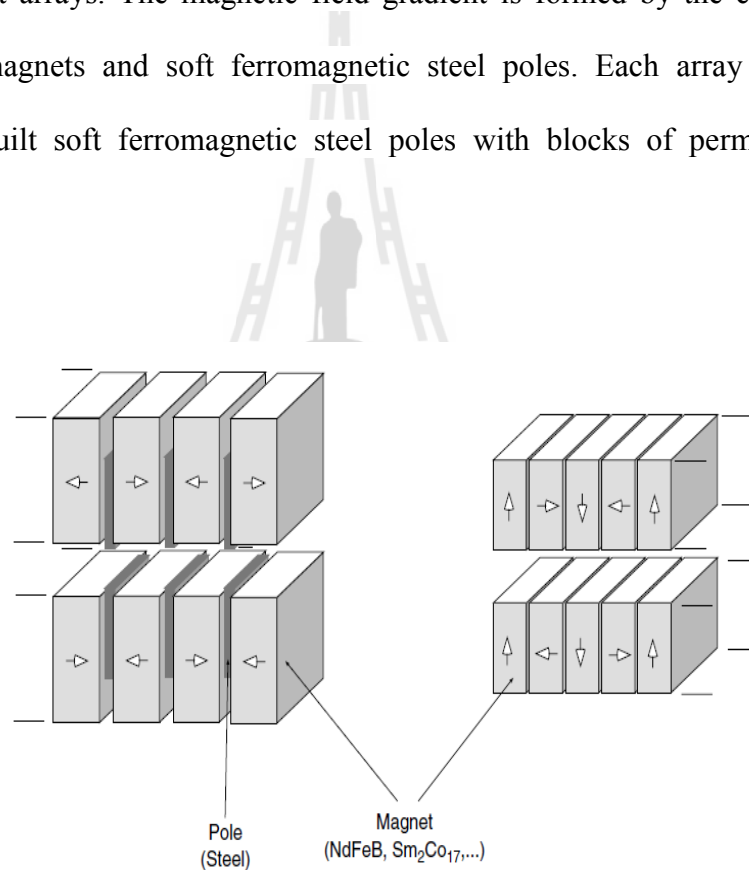


**Figure 2.11** Schematic of a hybrid (left) and pure permanent (right) magnets insertion devices (Onuki, Elleaume, 2003).

The soft ferromagnetic poles can be made from steel materials or from exotic materials such as vanadium permendur, which result in better and higher performance

magnets and cheaper. For the permanent magnet, the Neodymium Iron and Boron (NdFeB) magnet are considered to produce. The achievable peak field compared between hybrid and pure permanent magnets as plotted in Figure 2.12. They can be expressed by

$$B_y = 3.33 \exp[-g / \lambda_p (5.47 - 1.8g / \lambda_p)] \quad (2.41)$$

$$B_y = 1.55 \exp(-\pi g / \lambda_p) \quad (2.42)$$

Since the multipole gap and wavelength period are defined by  $g$  and  $\lambda_p$ .

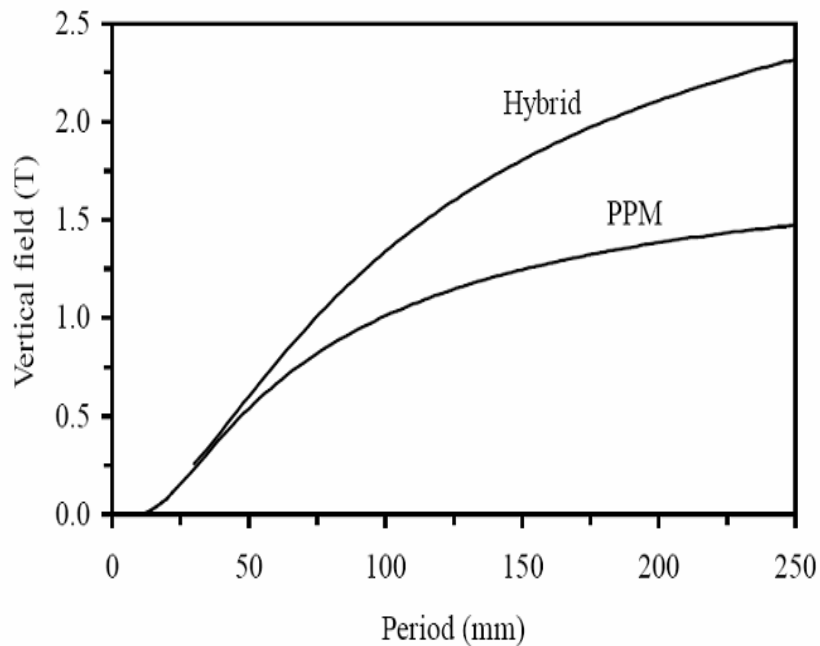


**Figure 2.12** Peak of the field as a function of the ratio of the magnetic gap to period for a pure permanent magnet structure and a hybrid structure with pole made of Vanadium Permendur (Assumes  $B_r = 1.1$  T and gap = 20 mm) (Clarke, 2013).



### 2.2.2 The motion of electron in insertion device

The IDs will introduce the vertical focusing property in the y-axis due to oscillating of the electron in the deflecting plane due to the periodic sinusoidal field distribution along the motion path (Wiedemann, 2007; Walker, 1995). As a result, a field gradient component appears to the electron deflecting in the vertical plane only and it is periodic along the electron beam motion. In the periodic of magnetic field is described by a sinusoidal distribution. The peak field is given by

$$B_x = 0, \quad (2.43)$$

$$B_y = B_0 \sin(k_w s), \quad (2.44)$$

Where  $k_w$  is  $2\pi/\lambda_w$  and  $\lambda_w$  is the insertion device period length.

The Lorentz force can be optioned to electron motion inside a device magnet with the field B. Thus we will only discuss the particle motion in the horizontal plane because the vertical motion is normally negligible. The equation of motion can be written as

$$x'' = \frac{d^2 x}{ds^2} = -\frac{e}{\gamma m_0 c} (B_y - y' B_s), \quad (2.46)$$

$$y'' = \frac{d^2 y}{ds^2} = -\frac{e}{\gamma m_0 c} (x' B_s - B_x) \approx 0, \quad (2.47)$$

with

$$\frac{dx}{dz} \frac{dz}{dt} = x', \quad \beta \approx 1, \quad (2.48)$$

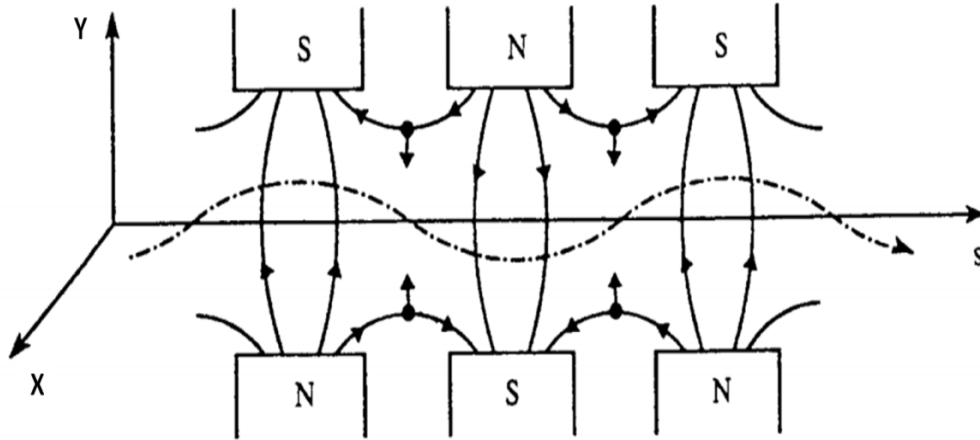


**Figure 2.13** Schematic principle of the creation of synchrotron radiation. An electron trajectory along s-axis passes through the device magnet (Walker, 1995).

The magnetic field has the vertical magnetic field component only, and the electron motion in horizontal plane as shown in Figure 2.13 can therefore be obtained by

$$x' = \frac{e}{\gamma mc} \int_0^s B_y(s') ds' = \frac{\cos(k_w s)}{\rho_w k_w}, \quad (2.49)$$

$$x = \frac{e}{\gamma mc} \int_0^s ds' \int_0^{s'} B_y(s'') ds'' = -\frac{\sin(k_w s)}{\rho_w k_w^2} \quad (2.50)$$

Since  $\frac{1}{\rho_w} = \frac{eB_w}{\gamma mc}$ .

### 2.3 Effects of insertion devices on beam dynamics

The vertical focusing from insertion device (ID) produces two leading deleterious effects (Robert, 1998; Liu, Zhang, 1999). The focusing shifts the tunes and alters the betatron function around the storage ring, which are shift produced by

focusing perturbation from ID resulting to beam loss and beam lifetime. We proceed by estimating the equivalent focusing parameter of the ID.

### 2.3.1 Tune shift

The tune shift is caused by the focusing force of the insertion device in the storage ring. The perturbation to the tune shift due to a focusing deflection is approximately

$$\Delta\nu = \frac{1}{4\pi} \int \Delta K \beta ds, \quad (2.51)$$

$\beta$  represents the amplitude of the betatron function and  $\Delta K$  denotes the deviation of focusing force in the region where the insertion device is installed.

The vertical focusing parameter is given by

$$k_0 = 0, \quad k_y = \left( \frac{e}{\gamma m_0 c} \right)^2 \frac{B_y^2}{2} = \frac{1}{2\rho_w^2} \quad (2.52)$$

$$\frac{1}{F_y} = \int k_y ds = \left( \frac{e}{\gamma m_0 c} \right)^2 \frac{B_y^2}{2} L_w \quad (2.53)$$

The tune shift can be calculated by

$$\Delta\nu_x = \frac{1}{4\pi} \int k_x \beta_x ds \approx 0, \quad (2.54)$$

$$\left. \begin{aligned} \Delta\nu_y &= \frac{1}{4\pi} \int k_y \beta_y ds = \frac{1}{4\pi} \int_0^{L_w} \frac{1}{2\rho_w^2} \beta_y ds \\ &\approx \frac{L_w \bar{\beta}_y}{8\pi\rho_w^2} \\ &\approx \frac{\bar{\beta}_y}{4\pi F_y} \end{aligned} \right\} \quad (2.55)$$

Where  $\bar{\beta}_y$  is the average of the vertical betatron function at position that insertion device is located and L is the length of the insertion device.

### 2.3.2 Beta-Beating

The distortion of beta function due to the insertion device in the ring is given by

$$\left(\frac{\Delta\beta_\phi}{\beta_\phi}\right) = -\left(\frac{\nu}{2\sin(2\pi\nu)}\right) \int_\phi^{\phi+2\pi} k\beta^2 \cos[2\nu(\pi + \phi - x)] dx \quad (2.56)$$

By the integral of Eq. (2.55) over the interval of the insertion device's displacement, the betatron function distortion can be obtained

$$\left(\frac{\Delta\beta_\phi}{\beta_\phi}\right) \approx -\left(\frac{kL\bar{\beta} \cos[2\nu(\pi - |\phi - \phi_1|)]}{2\sin(2\pi\nu)}\right) \quad (2.57)$$

Where  $\phi_1$  is the phase of the betatron function in the center position of insertion device. The conditions are considered as follow

$$\left(\frac{\Delta\beta_\phi}{\beta_\phi}\right)_y \approx \frac{-L\bar{\beta}_y \cos[2\nu_y(\pi - |\phi - \phi_1|)]}{4\rho^2 \sin(2\pi\nu_y)} \quad (2.58)$$

If we assume that  $k_x \approx 0$ ,  $k_y \approx \frac{\rho_w^2}{2}$ , and  $\left(\frac{\Delta\beta_\phi}{\beta_\phi}\right)_x \approx 0$ . Finally, the maximum of the beta-

beating can be expressed as

$$\left(\frac{\Delta\beta_y}{\beta_y}\right)_{\max} \approx \frac{\beta_y L_{\text{wiggler}}}{4\rho_w^2 \sin(2\pi\nu_y)}, \quad \frac{\Delta\beta_x}{\beta_x} \approx 0 \quad (2.59)$$

Where  $\beta_y$  is the average value of the betatron function at the position of insertion device,  $L_{\text{wiggler}}$  is the length of the insertion device, and  $\nu_y$  is the vertical betatron tune.

## 2.4 The effect due to the emission of synchrotron radiation

A high field insertion device will have a focusing effect on the stored electron beam in vertical axis. Integrals of magnetic field characteristic functions in a storage ring can be used to describe many of the important properties of the stored beam. Therefore, this will be started with the basic beam dynamic parameters and they can be described by the synchrotron radiation integrals, which are given by

$$\left. \begin{aligned}
 I_1 &= \int \frac{\eta(s)}{\rho} ds \\
 I_2 &= \int \frac{1}{\rho^2} ds \\
 I_3 &= \int \frac{1}{|\rho|^3} ds \\
 I_4 &= \int \frac{(1-2n(s))\eta(s)}{\rho^3} ds, \quad n(s) = \rho^2 \frac{\partial}{\partial x} (1/\rho) \\
 I_5 &= \int \frac{H(s)}{|\rho(s)|^3} ds, \quad H(s) = \frac{1}{\beta} [\eta^2 + \langle \beta\eta' - 0.5\beta'\eta \rangle]
 \end{aligned} \right\} \quad (2.60)$$

Where  $\eta$  and  $\beta$  are the dispersion function and the betatron function, respectively, and the integrals are taken along the circumference of the ring (Chao *et al.*, 2007). Many beam parameters can be calculated from the synchrotron radiation integrals (Bahrtdt, 1995). These parameters have been used to study effects of insertion devices in synchrotron light sources.

### 2.4.1 Momentum compaction

The momentum compaction factor  $\alpha_c$  has an effect on beam dynamics parameters like the synchrotron tune.

$$\alpha_c = \frac{I_1}{C_0} \quad (2.61)$$

with  $I_1 = \int \frac{\eta(s)}{\rho} ds$ ,  $C_0$  is circumference of the ring. Now let's calculate the synchrotron

integral of  $I_1$

$$I_{1w} = \int_0^{L_w} \frac{\eta_x}{\rho} ds \quad (2.62)$$

With the bending radius and quadrupole gradient, the dispersion is given by

$$\frac{d^2 \eta_x}{ds^2} + K \eta_x = \frac{1}{\rho}, \quad (2.63)$$

with  $K = \frac{1}{\rho^2} + k_1$  and  $\eta_x \approx \eta_0 \sin k_w s$

$$\frac{d^2 \eta_x}{ds^2} + \frac{B_w^2}{(B\rho)^2} \eta_0 \sin^2 k_w s = \frac{B_w}{B\rho} \sin k_w s \quad (2.64)$$

If  $k_w \rho_w \gg 1$ , The second term can be neglected

$$\eta_x \approx \frac{\sin k_w s}{\rho_w k_w^2}, \quad \rho_w = \frac{B\rho}{B_w} \quad (2.65)$$

Let's consider the wiggler contribution to  $I_1$

$$I_{1w} = \int_0^{L_w} \frac{\eta_w}{\rho} ds \approx - \int_0^{L_w} \frac{\sin^2 k_w s}{\rho_w^2 k_w^2} ds = - \frac{L_w}{2\rho_w^2 k_w^2} \quad (2.66)$$

Finally, the momentum compaction can be estimate by

$$\alpha_c = - \frac{L_w}{2\rho_w^2 k_w^2 C_0} \quad (2.67)$$

## 2.4.2 Energy loss

The IDs will rise up the particle energy loss from synchrotron radiation by contributing dipole fields. The total energy loss per turn in the storage ring by the device magnet can be written as ( $C_\gamma = 8.846 \times 10^{-5} \text{ m/GeV}^3$ )

$$U_0 = \frac{C_\gamma}{2\pi} E^4 I_2 \quad \text{with} \quad I_2 = \int \frac{1}{\rho^2} ds \quad (2.68)$$

Need to add the wiggler contribution

$$I_{2w} = \int_0^{L_w} \frac{1}{\rho^2} ds = \frac{1}{(B\rho)^2} \int_0^{L_w} B^2 ds = \frac{1}{(B\rho)^2} \frac{B_w^2 L_w}{2} \quad (2.69)$$

The energy loss by wiggler become

$$U_w = \frac{C_\gamma}{2\pi} \frac{E^4}{(B\rho)^2} \frac{B_w^2 L_w}{2} \quad (2.70)$$

### 2.4.3 Energy spread

The energy spread depends on the contributions to the synchrotron radiation integral of  $I_3$  and  $I_2$  as follows

$$\sigma^2 = C_q \gamma^2 \frac{I_3}{J_z I_2} \quad (2.71)$$

With 
$$I_3 = \int \frac{1}{\rho^2} ds \quad (2.72)$$

The bending radius in the wiggler is

$$\frac{1}{\rho} = \frac{B}{B\rho} = \frac{B_w}{B\rho} \sin k_w s = \frac{1}{\rho_w} \sin k_w s \quad (2.73)$$

The third synchrotron radiation integral term can be estimated as

$$I_{3w} = \frac{1}{\rho_w^3} \int_0^{L_w} |\sin^3 k_w s| ds = \frac{4L_w}{3\pi\rho_w^3} \quad (2.74)$$

We know the  $I_2$  is  $\frac{1}{(B\rho)^2} \frac{B_w^2 L_w}{2}$  so the energy spread can be written as

$$\sigma^2 \approx \frac{8}{3\pi} C_q \frac{\gamma^2 (B\rho)^2}{B_w^2 \rho_w^3} \quad (2.75)$$

Where  $\rho_w = \frac{mc\gamma}{eB_w}$  and  $C_q = \frac{55}{32\sqrt{3}} \frac{\hbar}{mc} \times 10^{-13} \text{ m}$ . The energy spread increases if

$\rho / \rho_w > 3\pi/8$  when the ID field is higher than that of the bending magnets.

#### 2.4.4 Emittance

Let us consider the variation in the emittance due to the emission radiation from insertion devices. The beam emittance relates with the beam size and divergence in order to maintain the beam brightness of synchrotron radiation emitted from ID. The emittance in the storage ring can be written in term of the contribution  $I_2$  and  $I_5$  of the insertion device as

$$\varepsilon = C_q \gamma^2 \frac{I_5}{J_x I_2} \quad (2.76)$$

$$I_{2w} = \int_0^{L_w} \frac{1}{\rho^2} ds = \frac{1}{(B\rho)^2} \int_0^{L_w} B^2 ds = \frac{1}{(B\rho)^2} \frac{B_w^2 L_w}{2} \quad (2.77)$$

$$I_5 = 0 \quad (2.78)$$

with  $H_x = \gamma_x \eta_x^2 + 2\alpha_x \eta_x \eta'_x + \beta_x \eta_x'^2$ . We assume  $\alpha_x \approx 0$  and  $k_w \gg$  then we can get

$$\eta'_x \approx \frac{d\eta_x}{ds} = k_w \eta_0 \cos k_w s \quad (2.79)$$

$$H_x \approx \frac{\beta_x}{\rho_w^2 k_w^2} \cos^2 k_w s \quad (2.80)$$

This the term of  $I_5$  can be written as



$$\begin{aligned}
 I_{5w} &\approx \frac{\langle \beta_x \rangle}{\rho_w^2 k_w^2} \int_0^{L_w} \frac{\cos^2 k_w s}{|\rho|^3} ds \\
 &= \frac{\langle \beta_x \rangle}{\rho_w^5 k_w^2} \int_0^{L_w} |\sin^3 k_w s| \cos^2 k_w s ds
 \end{aligned}
 \quad \left. \vphantom{\int_0^{L_w}} \right\} \quad (2.81)$$

$$\text{Using } \langle |\sin^3 x| \cos^2 x \rangle = \frac{4}{15\pi}$$

$$I_{5w} \approx \frac{4}{15\pi} \frac{\langle \beta_x \rangle L_w}{\rho_w^5 k_w^2} \quad (2.82)$$

From  $I_{2w}$  and  $I_{5w}$ , the emittance of a storage ring with IDs can be expressed as

$$\varepsilon_w = C_q \gamma^2 \frac{8}{15\pi} \frac{\langle \beta_x \rangle}{\rho_w^3 k_w^2} \quad (2.83)$$

Where  $C_q$  is the quantum constant,  $3.84 \times 10^{-13}$  m.

If the ID is inserted in locations with non zero dispersion, it will be increased the beam size at high energy.



# **CHAPTER III**

## **MAGNETIC FIELD MEASUREMENT OF TWO INSERTION DEVICES**

This chapter discusses how the magnetic fields of two insertion devices are measured, calculated, and compensated. Shows also are the techniques and instruments which are used for the field measurements. The maximum field of 6.5 Tesla was produced at the SWLS of 308 A. The MPW gap of 20 mm generates the magnetic field of 2.38 Tesla. The flipping coil and hall probe were used to measure the field integral of SWLS and MPW, respectively. The magnetic field error can be compensated by correction coil and shimming method to give smaller errors for SWLS and MPW, respectively. At the maximum field of two insertion devices, the electron orbits are shifted to 11.24 mm and 0.72 mm from the center position. Moreover, the maximum angle deviations are changed from the middle plane to 85.09 and 12.53 mrad by 6.5 Tesla SWLS and 2.18 Tesla MPW, respectively.

### 3.1 Measuring tools

#### 3.1.1 Hall probe

In this magnetic field measurement, the Hall Probe Model 460 3-axis Hall Effect Gaussmeter – Lake Shore shown in the Figure 3.1 is used and controlled by using the LabVIEW program.

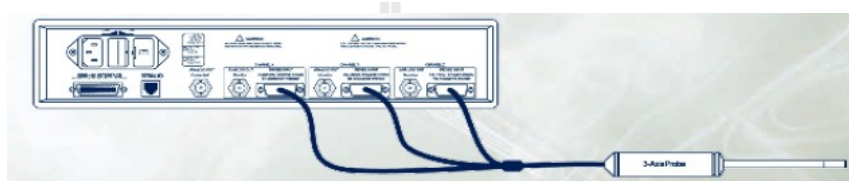


**Figure 3.1** Model 460 configured as a 3-axis gaussmeter (From <http://www.lakeshore.com/Documents/460.pdf>).

The Hall Probe is used to measure the magnetic field mapping of SWLS and hybrid MPW. And then the magnetic field integral of MPW is also assessed by Hall Probe scanning as shown in Figure 3.2. The magnetic field forces the charged particles and pushes the electric current to one side of the conductor when it flows through a conductor in the Hall Probe. The charged particles which are built up at the sides of the conductors will balance this magnetic influence by generating a transverse voltage between the two sides of the conductor. This phenomenon in Hall Probe is called the Hall Effect. The Hall voltage is given by

$$V_H = \frac{IB}{ned} \quad (3.1)$$

Where  $n$  is the density of charge carriers,  $d$  the plate thickness,  $I$  the current and,  $B$  the normal component of magnetic field.

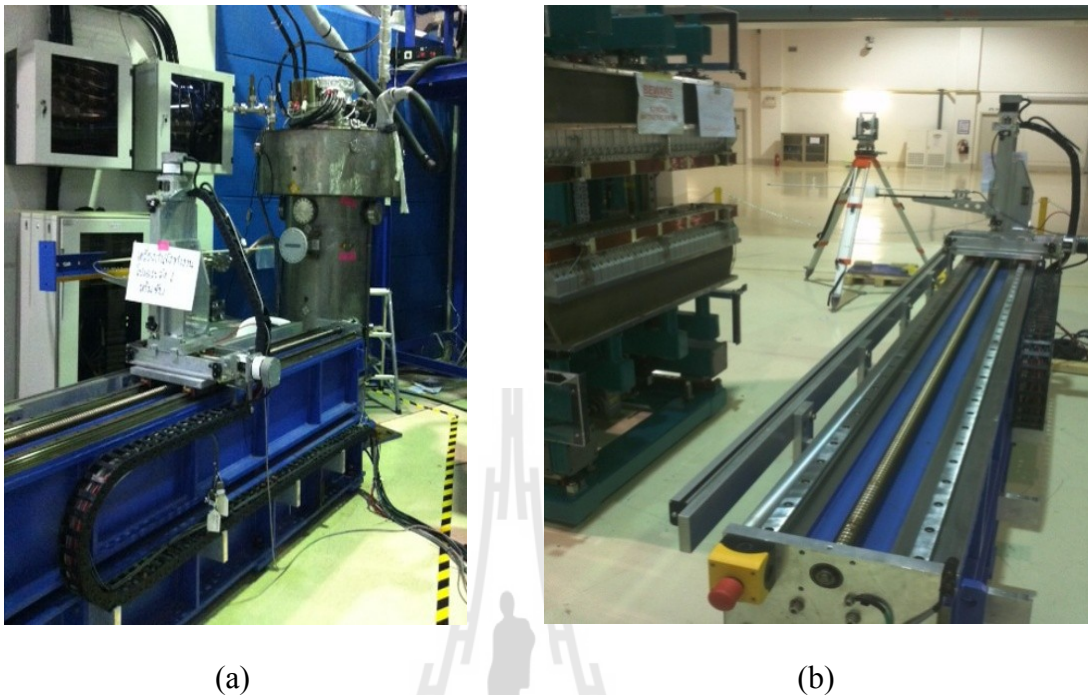


**Figure 3.2** Hall probe setup for measurement of a magnetic field of (a) SWLS and (b) MPW. (From [www.slri.or.th](http://www.slri.or.th))

### 3.1.2 Flipping coil

The flipping coil (see Figure 3.3) is used to measure the first and second field integral of the several magnets as, for instance, the insertion device magnets. In this work, the flipping coil is used to measure the magnetic field of superconducting wavelength shifter. The system diagram of flipping coil is set up as shown in Figure 3.4. The measuring coil has to be longer than the device magnet length. The square configuration is performed to measure first field integral measurement. The long coil is shaped in an 8-shape configuration. The flipping coil can be controlled to rotate with LabVIEW software.

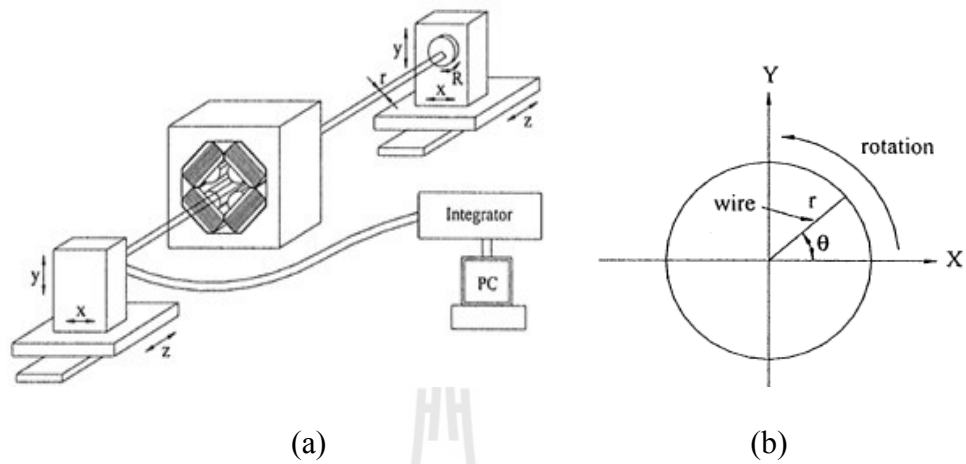


**Figure 3.3** (a) The flipping coil diagram and (b) the moving method for measuring the field integral (Hwang *et al.*, 2003).



**Figure 3.4** The flipping coil setup for measuring first and second field integral of SWLS.

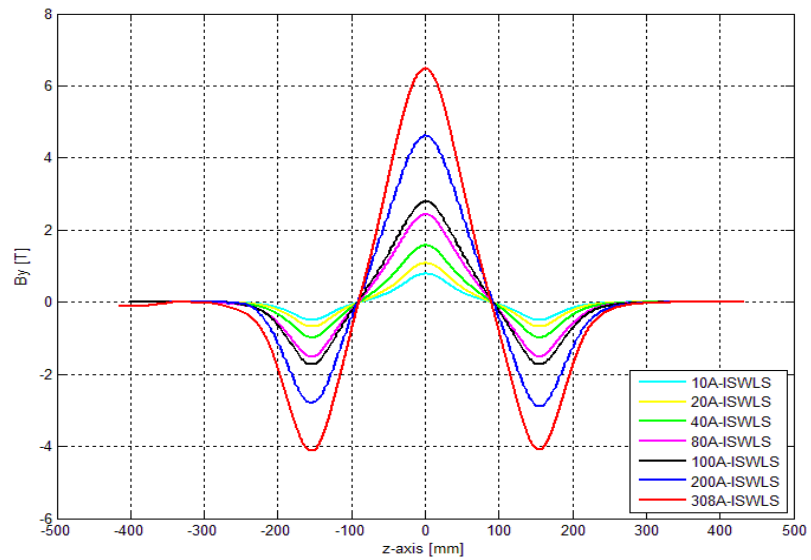
### 3.2 Magnetic field mapping of two insertion devices

Detailed magnetic field measurements were performed by a field measurement system which consists of the three-axis test bench with a Hall probe. In the measurements, the surfaces of the Hall probe were fixed on the same plane as those of the magnets. The fields were mapped on a 1 mm interval. These procedures were operated by LabVIEW software. The results of measurement will be also detailed in this chapter. Longitudinal magnetic field distribution along the z-axis is presented in Figure 3.5. There are three processes to find the center position of magnetic field before the magnetic field mappings along z-axis are started to measure.

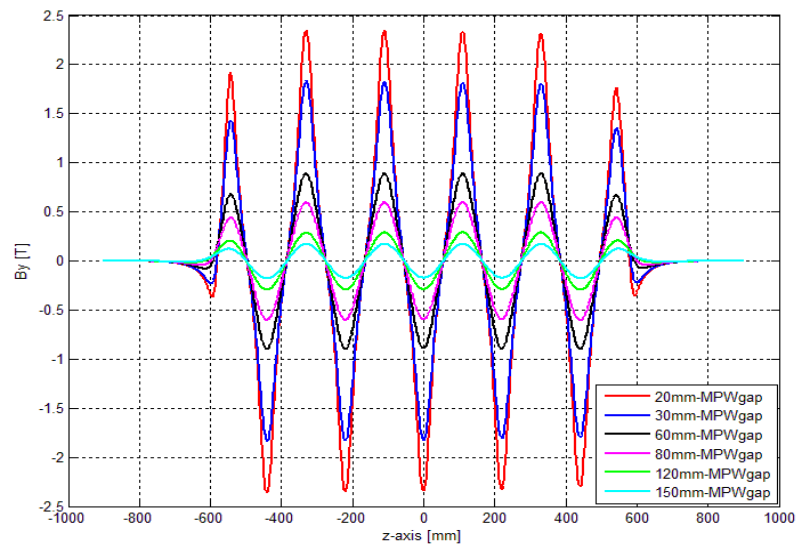
- i. Scan in y-axis for finding y center.
- ii. Scan in x- axis for finding x center.
- iii. Set hall probe at x, y center and scan in z-axis from upstream to downstream of SWLS or MPW for field mapping measurement.

The first is superconducting wavelength shifter mapping measurement, the magnetic field at three peaks corresponding to the three poles, one central pole and two side poles. The SWLS currents consisting of 10, 20, 40, 80, 100, 200, and 308A are measured and shown in Figure 3.6a. The magnetic field will be measured in ranges of - 400 to 400 mm. In the distribution along the z-axis at the magnetic current of 308 A exceeds 6.5 Tesla at middle plane and 4.17 T for two side poles. For the second is hybrid multipole wiggler field mapping measurement. The MPW gap can be adjusted in ranges of 20 to 180 mm. There are eleven poles consisting of nine central poles and two side poles. In this study, the magnetic fields were measured at 20, 30,

60, 80, 120, and 150 mm as shown in Figure 3.6b. The gap of 20 mm generates the maximum magnetic field of 2.38 T in middle plane ( $x = y = z = 0$ ).

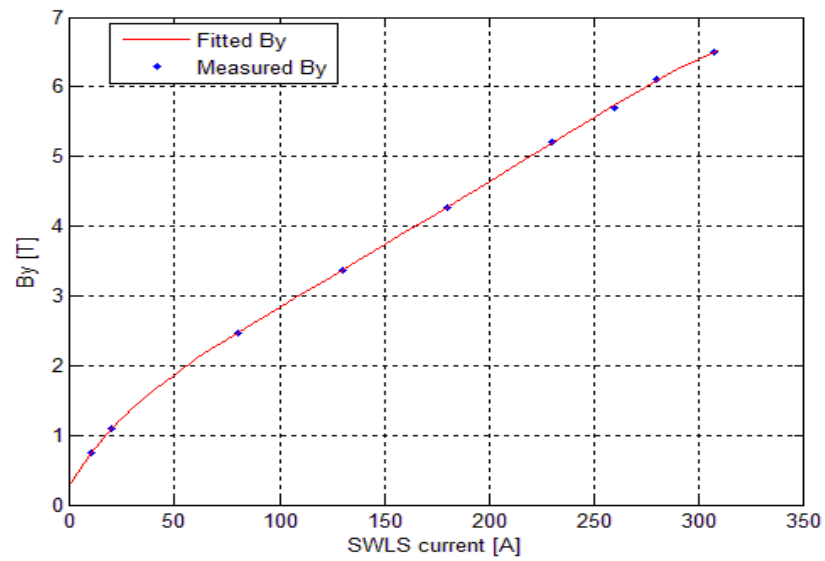


(a)

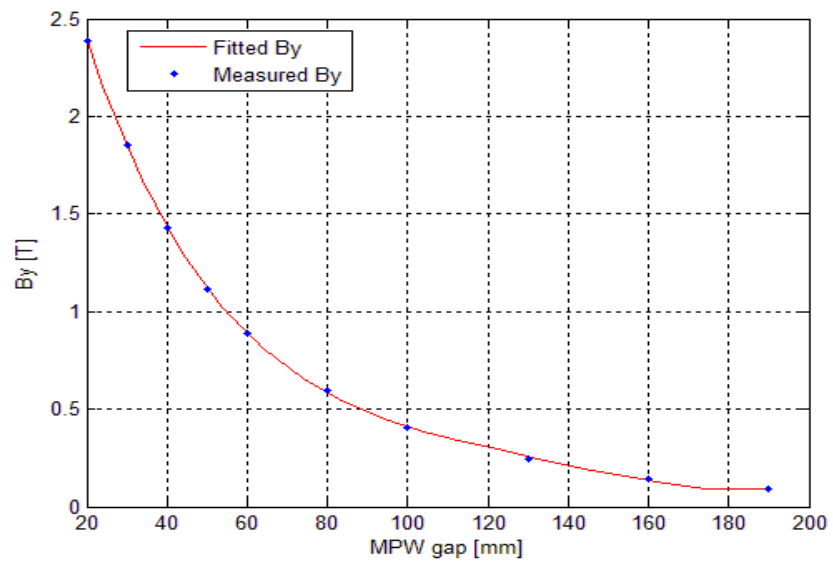


(b)

**Figure 3.5** Measured vertical field component along the longitudinal axis of (a) SWLS and (b) MPW.



(a)



(b)

**Figure 3.6** Peak magnetic field ( $B_y$ ) with different excited current of (a) SWLS and (b) MPW gap at center position  $x = y = z = 0$ .



The peak magnetic field at center position ( $x = y = z = 0$ ), the associated equations approximating the curves between magnetic field, SWLS current, and pole gap of the MPW are shown in Figure 3.6. The maximum magnetic fields are produced from SWLS and MPW to be 6.5 Tesla and 2.38 Tesla, respectively. The polynomial functions were fitted and can be written as

$$B(I) = 4.202E^{-11}I^5 - 1.783E^{-08}I^4 + 3.923E^{-06}I^3 - 4.693E^{-04}I^2 + 4.678E^{-02}I + 0.324 \quad (3.2)$$

$$B(G) = 8.795E^{-09}G^4 - 4.762E^{-06}G^3 + 9.729E^{-04}G^2 - 9.329E^{-02}G + 3.893 \quad (3.3)$$

Where I is superconducting wavelength shifter current in Ampere and G defines the MPW gap in mm.

### 3.3 Measurement and compensation of magnetic field integral

The magnetic field in insertion devices at the path of the electron beam must have only a y component, and the electrons oscillate around a straight line in the z direction. There are two measurements in this section. One is for measuring the first field integral of the insertion device to determine the electron beam angle deviation. The second is for measuring the second field integral of the insertion devices to determine the electron trajectory. (Aslaninejad *et al.*, 2007)

$$\text{The first field integral} \quad I_x = \int B_x dz \quad \text{and} \quad I_y = \int B_y dz \quad (3.4)$$

$$\text{The second field integral} \quad II_x = \iint B_x(z') dz dz' \quad \text{and} \quad II_y = \iint B_y(z') dz dz' \quad (3.5)$$

The multipole field errors of IDs have effects on the beam dynamics of the SPS storage rings. The field integrals can be expressed in terms of multipole field components consisting of the angle deviation and position of an electron at the exit of the insertion device. The quadrupole and sextupole field terms are used to calculate the effects on the betatron tune and chromaticities of the storage ring, respectively. And the effects on betatron coupling are approximated by the octupole term. The multipole terms of the magnetic field integrals content by using the fitting data to a polynomial fit function as following

$$B_0 + B_1x + B_2x^2 + B_3x^3 + \dots \quad (3.6)$$

Where  $B_0$  is the dipole field,  $B_1$  is the integrated quadrupole term,  $B_2$  is the integrated sextupole term, and  $B_3$  is the octupole field component.

The effects on electron beam dynamics and quality of the emitted synchrotron radiation arise from magnetic field errors. Ideally, the first and second field integrals should be zero. But in reality, these magnetic integrals are shift from zero. The non-zero field integrals along optical axis result to the change in closed orbit. The effects of quadrupole field errors can be compensated by correcting linear tunes and coupling using normal and skew quadrupole magnets. The multipole field errors can reduce the dynamic aperture and decrease life time of the beam. However, the imperfect magnetic system resulting to the magnetic field errors will be almost perfectly minimized and compensated by correction coils and trim coils for SWLS and MPW, respectively.

### 3.3.1 Superconducting wavelength shifter (SWLS)

For a SWLS, the flipping coil is used to measure the field integral (Thananchai, 2008). Figure 3.7 shows the flipping coil system diagram in the superconducting wavelength shifter.

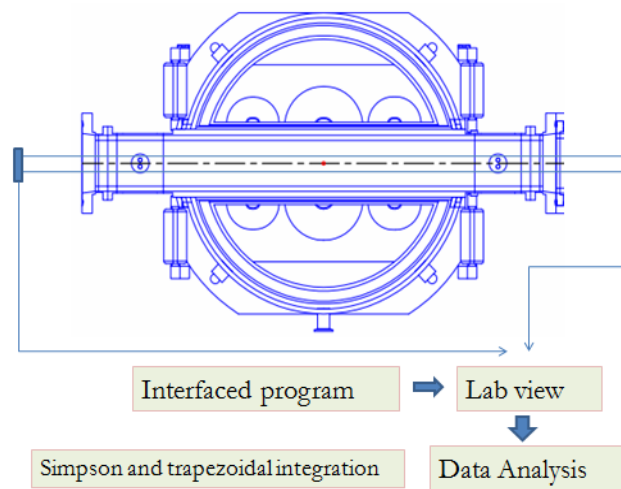


**Figure 3.7** The flipping coil system diagram.

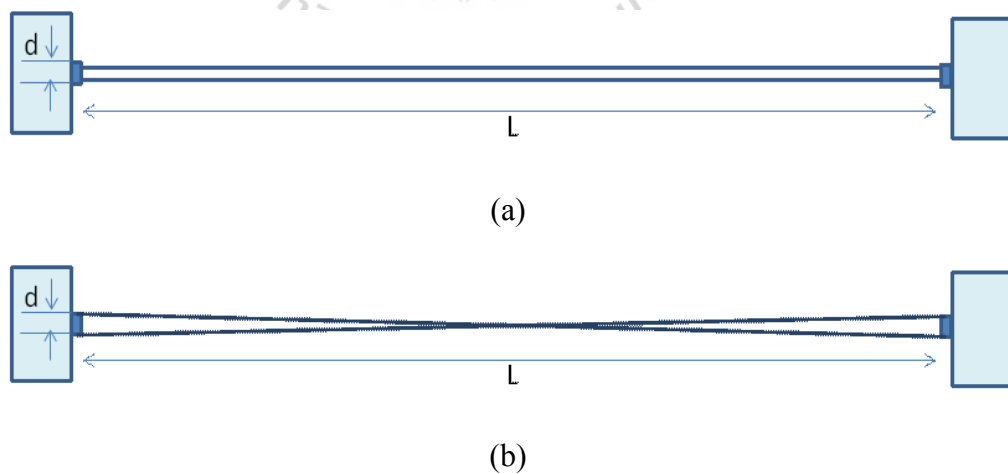


**Figure 3.8** The configuration coil for (a) first and (b) second field integral measurements of SWLS.

A close long coil consisting of N-turn coils as shown in Figure 3.8 is used to pick up the voltage induced from the magnetic flux variation as shown

$$V = -N \frac{d\phi}{dt} \quad (3.7)$$

Where  $\phi$  is the magnetic flux and N is number of coil turns. The magnetic flux can define to be given as

$$\phi = N \int_s \vec{L} \cdot \vec{n} \quad (3.8)$$

Where  $\vec{L}$  is wavelength shifter magnetic field  $\vec{L} = L_x \hat{x} + L_y \hat{y}$

$\vec{n}$  is normal vector and to be written in x-y plane (Figure 3.9)  $\vec{n} = \sin\phi \hat{x} + \cos\phi \hat{y}$

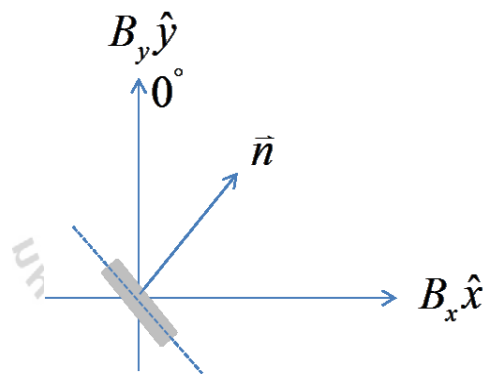


**Figure 3.9** Side view of the magnetic field vector along the longitudinal axis.

From Equation 3.8, the magnetic flux becomes

$$\phi = \phi_x + \phi_y = N \int_s B_x \sin\theta ds + N \int_s B_y \cos\theta ds, \quad (3.9)$$

The voltage V in Equation 3.9 can be written as

$$V = -N \left[ \frac{d\phi_x}{dt} + \frac{d\phi_y}{dt} \right] \quad (3.10)$$

By substituting the magnetic flux into the induced voltage equation and the coil is therefore formed with dimension  $L \times d$  as shown the result becomes

$$V = -Nd \left[ \int_0^L B_x(z) dz \sin \theta \frac{d\theta}{dt} + \int_0^L B_y(z) dz \cos \theta \frac{d\theta}{dt} \right] \quad (3.11)$$

Where  $d$  is the displacement between two coils measurements on the transverse axis.

From Equation 3.7 the voltage can form in first field integral as follow

$$V = -Nd \left[ I_x \sin \theta \frac{d\theta}{dt} + I_y \cos \theta \frac{d\theta}{dt} \right] \quad (3.12)$$

The coil is displaced as indicated in Figure 3.7b.

$$I_y = \frac{\int V dt}{Nd}, I_x = \frac{\int V dt}{Nd} \quad (3.13)$$

The second field integral measurement is similar to the first field integral measurement except the configuration of coil as shown in Figure 3.7b. We can start from Equation 3.11, and the magnetic flux for second field integral can be given as

$$\phi = \phi_x + \phi_y = \frac{2ND}{L'} \left[ \int_0^{L'} B_x z \cos \theta dz + \int_0^{L'} B_y z \sin \theta dz \right] \quad (3.14)$$

In term of  $\int_0^{L'} B_x z dz$  integrates by part and it becomes

$$\int_0^{L'} B_x z dz = \frac{L'}{2} \int_0^{L'} B_x(z) dz - \int_0^{L'} \int_0^{z'} B_x(z') dz' dz'' = \frac{L'}{2} I_x - II_x, \quad (3.15)$$

Therefore, the magnetic flux is formed in term

$$\phi = \phi_x + \phi_y = \frac{2ND}{L'} \left[ \frac{L'}{2} (I_x - II_x) \cos \theta + \frac{L'}{2} (I_x - II_x) \sin \theta \right] \quad (3.16)$$

The induced voltages at the coil is integrated, it will then be written as

$$V = -\frac{d\phi}{dt} = -\frac{2ND}{L'} \left[ \frac{L'}{2} (I_x - II_x) \cos \theta \frac{d\theta}{dt} + \frac{L'}{2} (I_x - II_x) (-\sin \theta) \frac{d\theta}{dt} \right] \quad (3.17)$$

Finally, the vertical second field integrals for SWLS are defined as

$$H_y = -\frac{L}{2} \left[ \frac{\int V dt}{Nd} + I_y \right], \quad H_x = -\frac{L}{2} \left[ \frac{\int V dt}{Nd} + I_x \right] \quad (3.18)$$

Before measuring the field integral, the coil must be formed in the square shape configuration. The schematic view is shown in Figure 3.10.

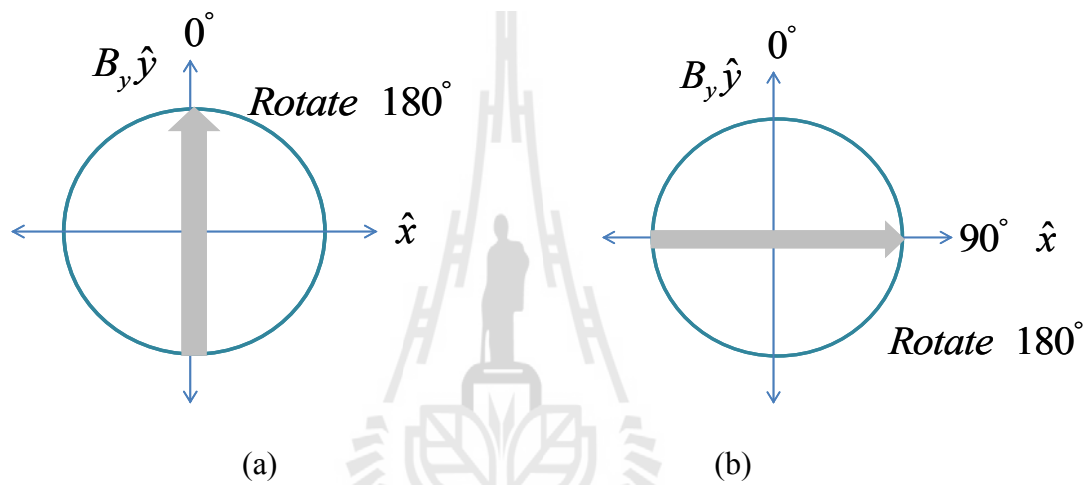


**Figure 3.10** The schematic views for (a) vertical and (b) horizontal field integrals measurements.

The flipping coil system is set up as follows

1. The long coil is made from 20 turns of copper wire with 0.04 mm diameter and 2 meters in length.
2. In the first vertical field integral measurement, the coil is started with configuration in Figure 3.9. It is then rotated from  $0^\circ$  to  $180^\circ$  and next it is rotated from  $180^\circ$  to  $360^\circ$ . Later, it is reversely rotated from  $0^\circ$  to  $-180^\circ$  and it is finally rotated from  $-180^\circ$  to  $-360^\circ$ .

3. During the first horizontal field integral measurement, the coil will be started to flip at  $90^\circ$  as detailed in Figure 3.10. First, the coil is flipped from  $90^\circ$  to  $270^\circ$ . Next, it is flipped from  $270^\circ$  to  $450^\circ$ . Later, the coil is flipped back from  $90^\circ$  to  $-270^\circ$ . Finally, it is flipped from  $-270^\circ$  to  $-450^\circ$ .
4. All data must be record and calculated as follow Equation 3.7 to Equation 3.13 for both planes and the measured signals for the first field integral are introduced in Figure 3.11.

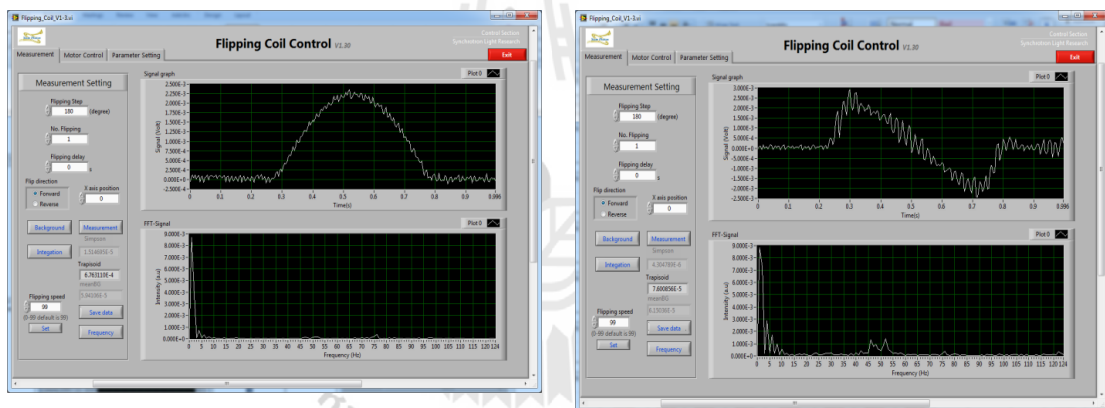


**Figure 3.11** The signals by using the flipping coil for vertical (left) and horizontal (right) field integrals.

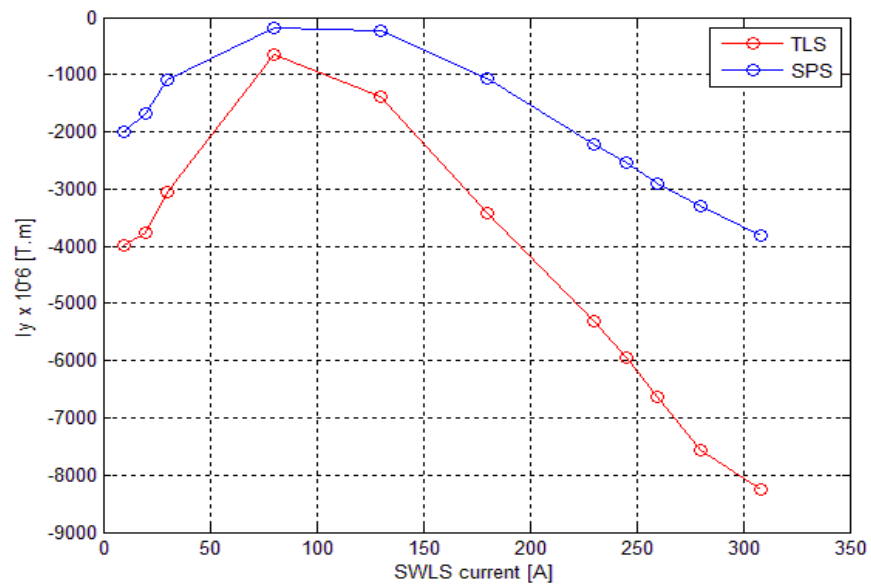


**Figure 3.12** Measured first integral field distribution along different SWLS current; the field integral were measured at TLS in red and SPS in blue at  $x = y = z = 0$ .



**Figure 3.13** The correction coils of SWLS.



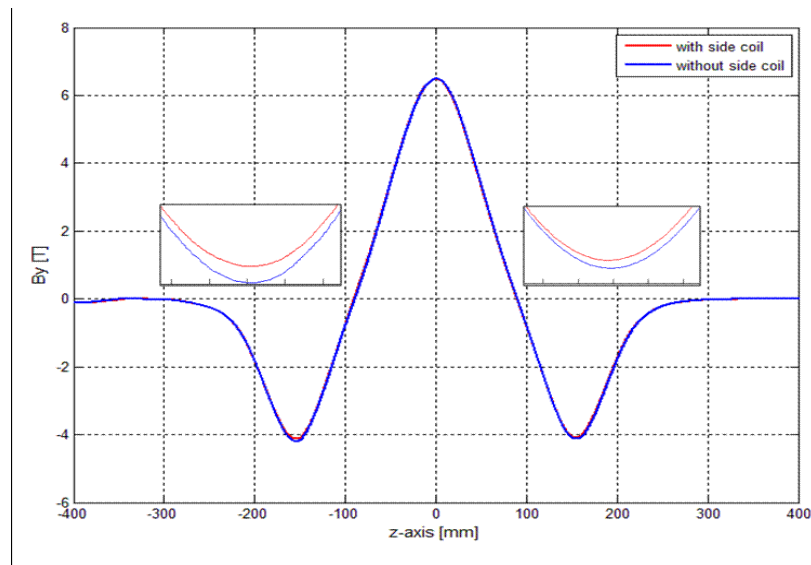
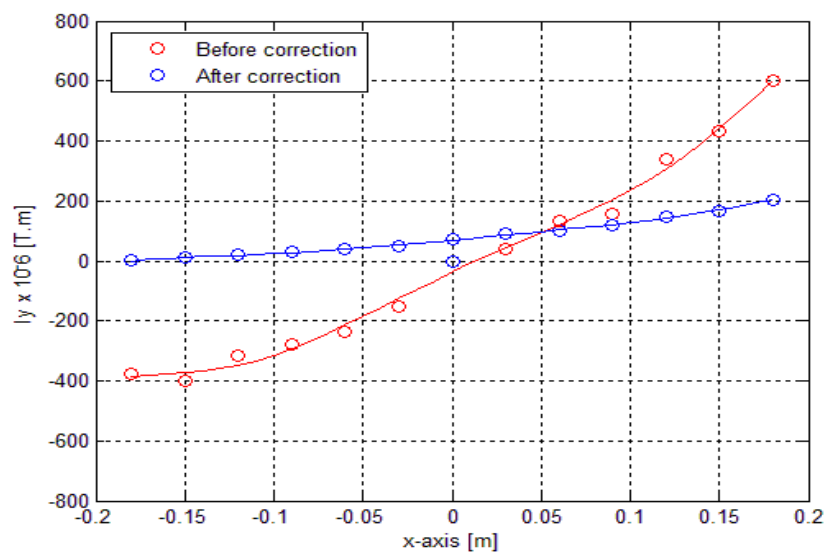
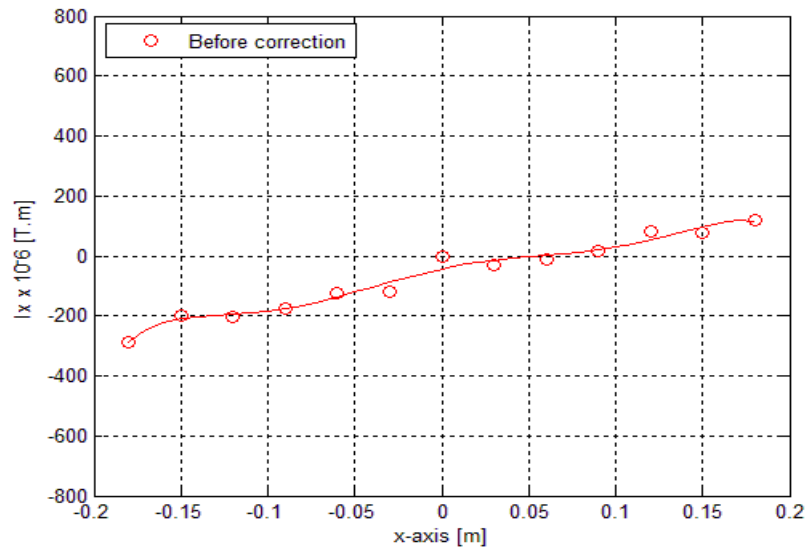


**Figure 3.14** The vertical magnetic field without and with side coil along the magnet in z-axis.



(a)

**Figure 3.15** Measured (a) vertical and (b) horizontal first integral field distribution along different trajectory on the transverse x-axis at SWLS current of 308 A.



(b)

**Figure 3.15** (Continue) Measured (a) vertical and (b) horizontal first integral field distribution along different trajectory on the transverse x-axis at SWLS current of 308 A.

The vertical field integral before correction is measured and shown in Figure 3.12. The results of the SWLS first horizontal field integrals are compared between at TLS and SPS measurement. This shows at 80 A the SWLS current has smallest error in both of two cases (SPS and TLS) after that it rises up SWLS current. At 308 A the SWLS current shows the field error has largest field error. The correction coil (see Figure 3.13) was applied to compensate the field error in quadrupole term. The magnetic field mapping along longitudinal axis after correction is shown in Figure 3.14. The data as presented in Figure 3.16 is analyzed and fitted to the polynomial functional form various restricted ranges. The multipole results of before correction are compared to after correction in Table 3.1. The range was restricted to -18 to 18 mm. The effect on the multipole values of the number of averages were used and also examined in the analysis. The vertical first field error associates to electron angle

distribution that passes through the device. These integrals can be expressed as polynomial expansion in both planes and integrated over its length. Before and after correction integral field results are detailed in function as

*Before correction:*

$$Iy(x) = -6.443E^6x^6 + 2.304E^4x^5 + 4.860E^3x^4 - 9.820x^3 - 0.452x^2 + 2.815E^{-2}x - 3.698E^{-5} \quad (3.19)$$

$$Ix(x) = -1.349E^7x^6 + 5.845E^4x^5 + 6.627E^3x^4 - 22.400x^3 - 0.859x^2 + 1.228E^{-2}x - 4.414E^{-5} \quad (3.20)$$

*After correction:*

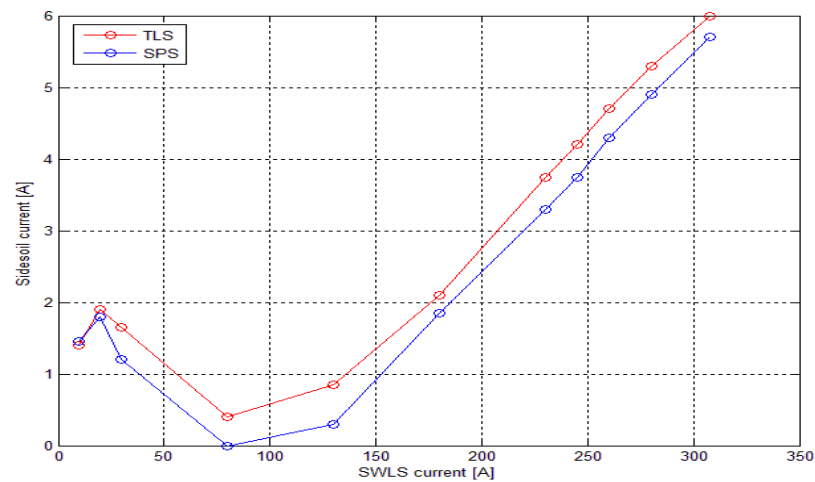
$$Iy(x) = -6.989E^5x^6 + 1.668E^4x^5 + 4.446E^2x^4 - 4.941x^3 + 0.320E^{-03}x^2 + 0.05540E^{-3}x - 2.244E^{-6} \quad (3.21)$$

**Table 3.1** The measured results at 6.5 Tesla SWLS magnetic field of the dipole corrector, quadrupole, and sextupole magnet.

Field integral	Before correction	After correction
<i>Vertical magnetic field integral</i>		
Dipole, T.m	$3.698 \times 10^{-5}$	$0.224 \times 10^{-5}$
Quadrupole, T	$2.815 \times 10^{-2}$	$0.00554 \times 10^{-2}$
Sextupole, T.m <sup>-1</sup>	0.452	$0.320 \times 10^{-03}$
Octupole, T. m <sup>-2</sup>	9.820	4.941
<i>Horizontal magnetic field integral</i>		
Dipole, T.m	$4.414 \times 10^{-05}$	-
Quadrupole, T	$1.228 \times 10^{-2}$	-
Sextupole, T.m <sup>-1</sup>	0.859	-
Octupole, T. m <sup>-2</sup>	22.400	-

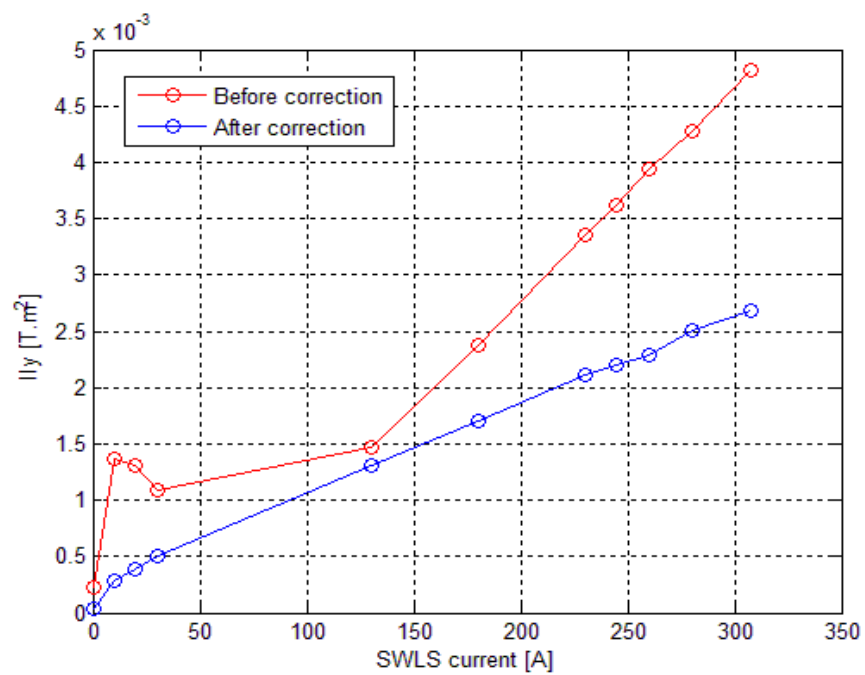
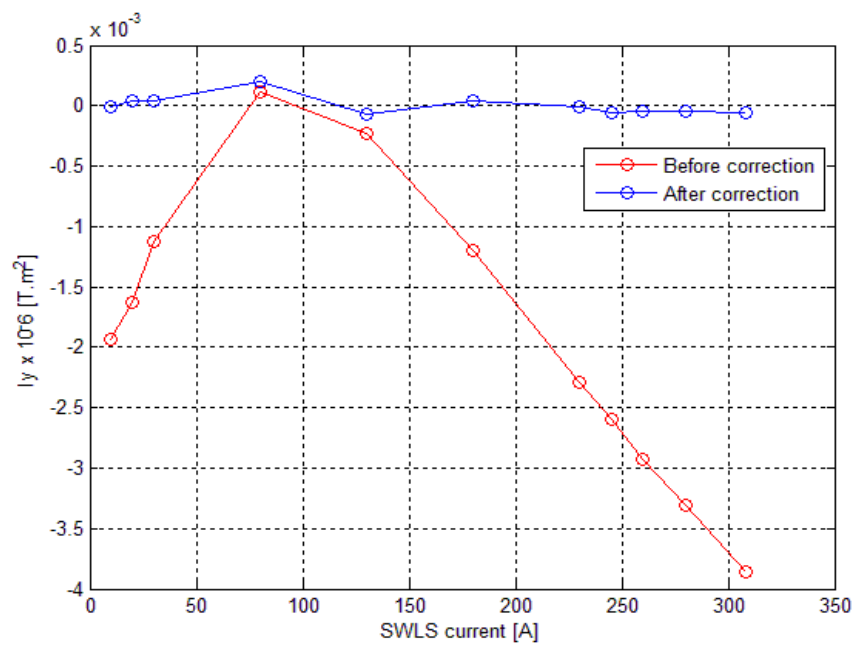
**Table 3.2** The currents of correction coil are used to compensate field error of SWLS.

SWLS current [A]	Correction coil currents [A]	
	at TLS	at SLRI
0.00	0.08	0.25
10.00	1.40	1.45
20.00	1.90	1.80
30.00	1.65	1.20
80.00	0.40	0.00
130.00	0.85	0.30
180.00	2.10	1.85
230.00	3.75	3.30
245.00	4.20	3.75
260.00	4.70	4.30
280.00	5.30	4.90
308.00	6.00	5.70



**Figure 3.16** The correction current coils different SWLS current; the field integral were measured at TLS in red and SPS in blue.

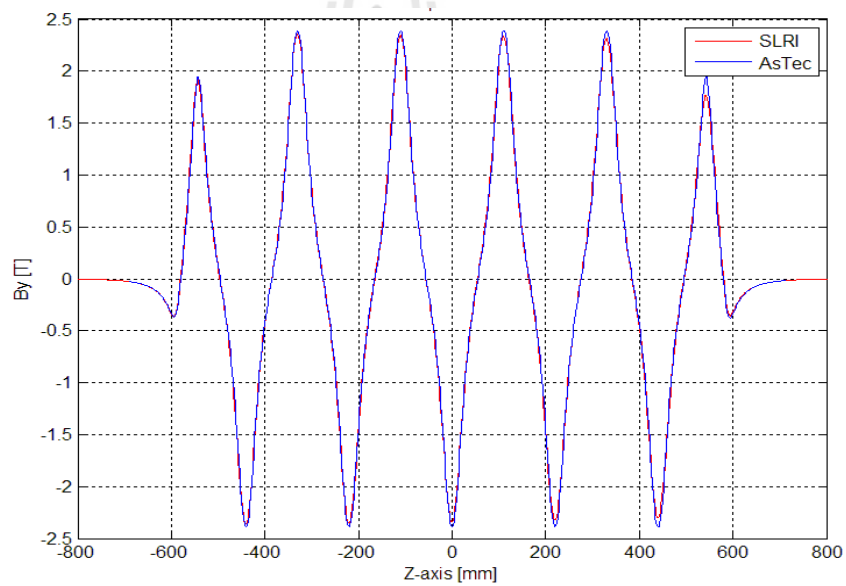
The correction coils current which are used to compensate the SWLS field error are plotted in Figure 3.16 and summarized in Table 3.2. The field integral in the blue line is the field integral that was measured at TLS and the red line is the measured result at SPS. The correction coils which are used to compensate field error at SLRI are smaller than at TLS due to the field error value. From field errors show that the magnet system of SWLS at SPS was aligned better than magnet alignment at TLS. Therefore, the correction coils current at TLS were then used to compensate field error much more than at SLRI. The second field integrals are only measured at the longitudinal axis,  $y = x = 0$ . The integrating signal in each SWLS current are measured at various the SWLS current from 0 to 308A and then the integrated field was obtained in Figure 3.17. After the correction coil was applied, the vertical quadrupole field error is reduced from  $2.815 \times 10^{-2}$  to  $0.00554 \times 10^{-2}$  Tesla. The betatron tune is shifted by this error term. This chapter develops a procedure for compensating field error due to misalignment of devices.



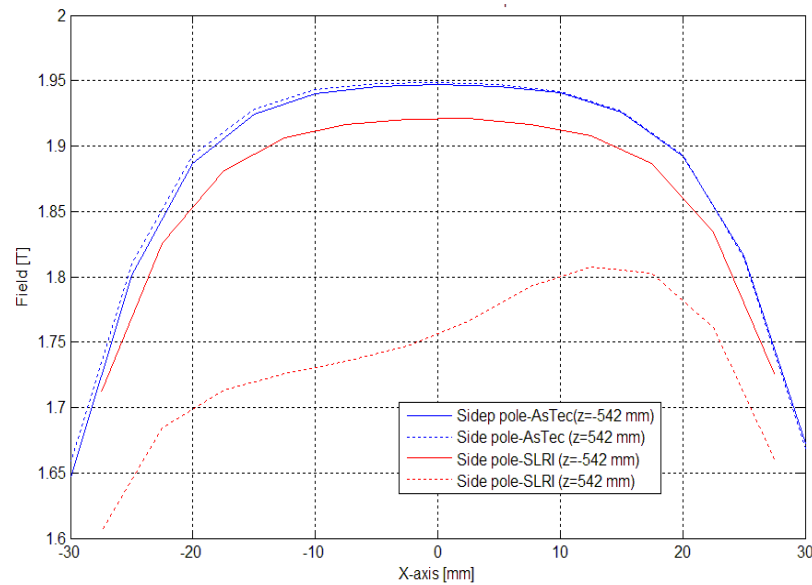
**Figure 3.17** The first (top) and second (bottom) magnetic field integrals of vertical plane.

### 3.3.2 Hybrid multipole wiggler (MPW)

The maximum peak magnetic of the MPW is 2.4 Tesla, the magnetic fields were measured by using Hall probe and compared to the measured data at ASTEC. Figure 3.18 presents the results of magnetic field before shimming along the electron direction pass through in z-axis in range of -800 to 800 mm at gap of 20 mm. The measured magnetic fields of two side poles are compared in Figure 3.15. This shows the side pole field at  $z = -542$  mm are higher than the side pole field at  $z = 542$  mm by 0.02 Tesla.



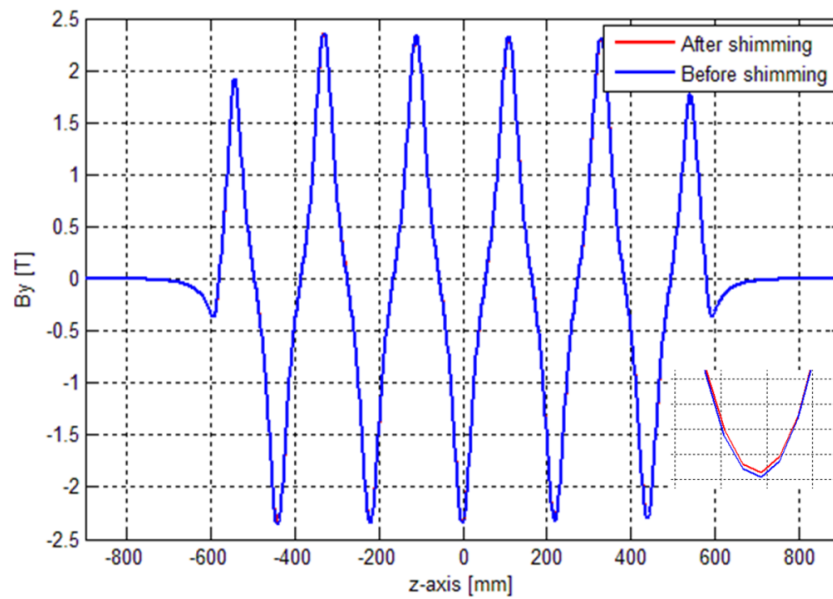
**Figure 3.18** The comparison of the measured magnetic field as a function of length ( $z$ ) at the centre of the wiggler, Red-measured by SLRI and Blue- measured by ASTEC.



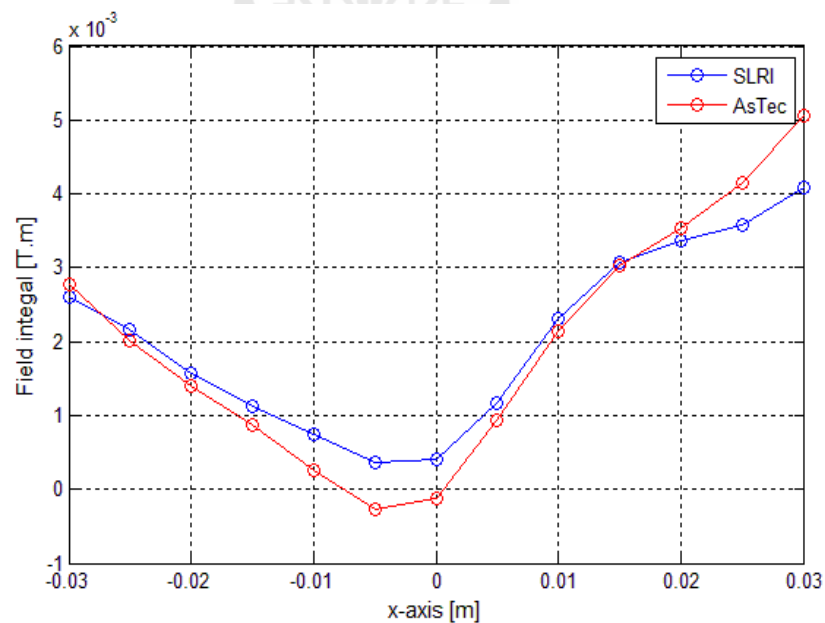
**Figure 3.19** The pole cross section of two side poles magnetic field for  $y = 0$ ,  $z = -542$  and  $542$  mm along  $x$  positions.

Figure 3.20 shows the magnetic field of two side poles between measured at ASTEC and SLRI. A comparison of the field profile across the two side poles were measured at SLRI and ASTEC. The measured result at SLRI shows that the roll off is not symmetrical because the magnet array is broken on one side at  $z = 542$  mm. They also have the effects from the discontinuity pole resulting to the magnetic field which have no symmetry compared to red line and red dot along  $x$  positions. The sextupole field error can be compensated by shimming. The shim plates are made from the thin vanadium (see Figure 3.20). They consist of 53.5% Co, 44.5% Fe, 1.75% V, 0.135% Cr, 0.03% Mn, and 0.01% Br. Their thicknesses are 0.43 mm and 0.2 mm. The field integrals are corrected by placing 0.2 mm thick (at  $x = 15$  mm) and 0.43 mm thick (at  $x = -10$  mm). The shim plate helps to reduce the field error in sextupole component in non linear term. Figure 3.20 compare the data between before and after shimming.





**Figure 3.20** Measured vertical field integral distribution along z direction as shown the data of before and after shimming at the gap of 20 mm.



**Figure 3.21** The comparison of the filed integral between ASTEC (red line) and SLRI (blue line) along the horizontal axis at the gap of 20mm.

Figure 3.21 presents the measured field integral to be compared between ASTEC and SLRI. The fitting functions can be fitted the dipole, quadrupole, sextupole and octupole components as a function of the MPW gap in x-axis.

*ASTEC:*

$$I_y(x) = 1.13465E^7 x^6 - 12.7191E^4 x^5 - 18.535E^3 x^4 + 193.169x^3 + 11.9477x^2 - 0.11195x - 3.25259E^{-5} \quad (3.22)$$

*SLRI:*

$$I_y(x) = 1.0051E^7 x^6 - 9.6525E^4 x^5 - 1.7032E^4 x^4 + 165.0712x^3 + 10.3333x^2 - 0.0950x + 5.2865E^{-4} \quad (3.23)$$

The distribution of magnetic fields and the field integrals of the MPW, which are compensated by shimming method, are compared in Figure 3.22. It is important to know how this sextupole component will affect the stability of the beam. This wiggler, sextupole terms are reduced from 10.494 T/m to 2.0209 T/m. The sextupole component has effect on the chromaticity in nonlinear effect. The following equations are fitted and compared between before and after shimming. The distribution fields are also used to calculate the electron trajectory and angle deviation. The multipole components, obtained from field integral, were used to analyze the effects of each component on the electron beam as listed in Table 3.3.

*Before shimming:*

$$I_y(x) = 1.0080E^7 x^6 - 9.5486E^4 x^5 - 1.7084E^4 x^4 + 163.5013x^3 + 10.4942x^2 - 0.0938x - 1.5786E^{-3} \quad (3.24)$$

*After shimming:*

$$I_y(x) = -1.1671E^7 x^6 + 6.8297E^4 x^5 + 1.6864E^4 x^4 - 94.7210x^3 - 2.0209x^2 + 6.4440E^{-3}x - 1.6897E^{-3} \quad (3.25)$$

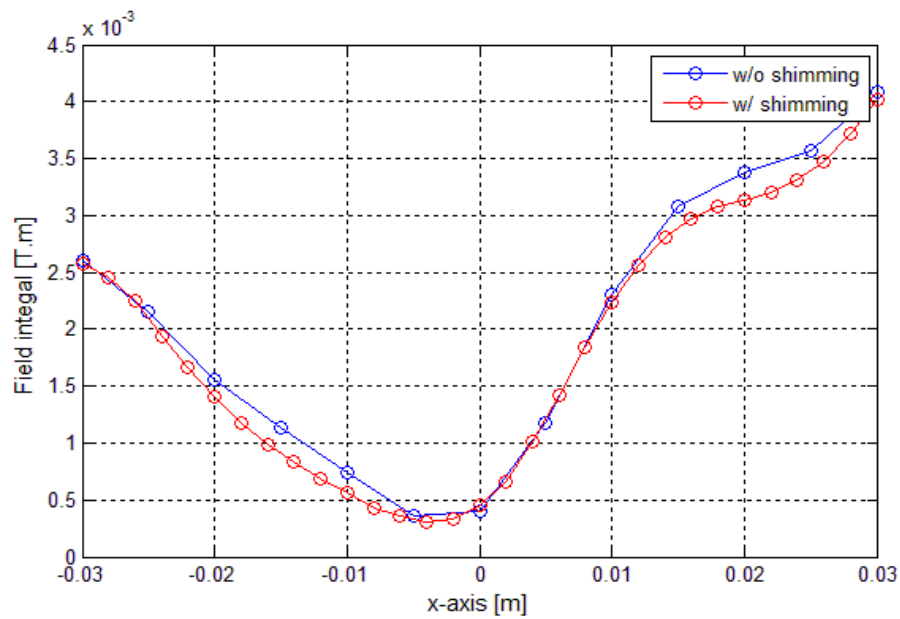


**Figure 3.22** The comparison of the first field integral along the horizontal axis at the gap of 20 mm, before shimming (blue line) and after shimming (red line).

**Table 3.3** The measured results at 2.18 Tesla MPW magnetic field of the multipole components.

Field integral	Before correction	After correction
<i>Vertical magnetic field integral</i>		
Dipole, T.m	$1.5786 \times 10^{-03}$	$1.6897 \times 10^{-03}$
Quadrupole, T	0.0938	$6.4440 \times 10^{-3}$
Sextupole, T.m <sup>-1</sup>	10.4942	2.0209
Octupole, T. m <sup>-2</sup>	163.5013	94.7210

### 3.4 Electron trajectory

As an electron beam passing through the insertion device, the force acting on the electrons is given by the Lorentz force (Rossbach and Schmuser, 1992). The electron displacement and angle associate with the first and second magnetic field integrals along the insertion device. The first and second field integral can be measured by using the Hall probe and flipping coil (Hwang *et al.*, 2003). For the vertical magnetic field, the horizontal angle of motion can be obtained by the simple integration

$$x'(z) = \frac{e}{\gamma mc} \int_{-z}^z B_y(z') dz' \quad \text{or} \quad x'(z) = \frac{0.3}{E[\text{GeV}]} I_y(z) \quad (3.26)$$

Where  $I_y(z)$  and  $B_y(z)$  are the vertical first field integral and the vertical magnetic field, respectively. And then the electron beam displacement can be calculated by

$$x(z) = \frac{e}{\gamma mc} \int_0^z dz' \int_0^{z'} B_y(z'') dz'' \quad \text{or} \quad x(z) = \frac{0.3}{E[\text{GeV}]} II_y(z) \quad (3.27)$$

Where  $II_y(z)$  is the vertical second field integral.

The electron beam trajectories are calculated by the magnetic field integral of insertion devices (SWLS and MPW). The electron is gradually kicked out from the ideal orbit because of the magnetic field error of IDs. The electron changes are presented in Figure 3.23 and 3.24 when pass though device magnets. They also show that at the exit of the devices the electron transverse positions are not zero. The results of electron trajectories are summarized in Table 3.4. The synchrotron radiation source point of the central pole are offset 11.24 mm and 0.72 mm at SWLS current of 308 A and the MPW gap of 20 mm, respectively away from the center. The results show that

the electron beam exits the devices with a finite angle, depending on the magnetic field. The maximum angle deviations are 85.09 mrad for SWLS and 12.53 mrad for MPW at the maximum magnetic field of device magnets. The electron trajectory is not zero at the end of insertion devices. The electron displacements are 2 mm and 0.1 mm at the maximum peak field of SWLS and MPW. This orbit deviation for trajectory and angle can be corrected by steering magnets adjacent to IDs will be discussed in the next chapter.

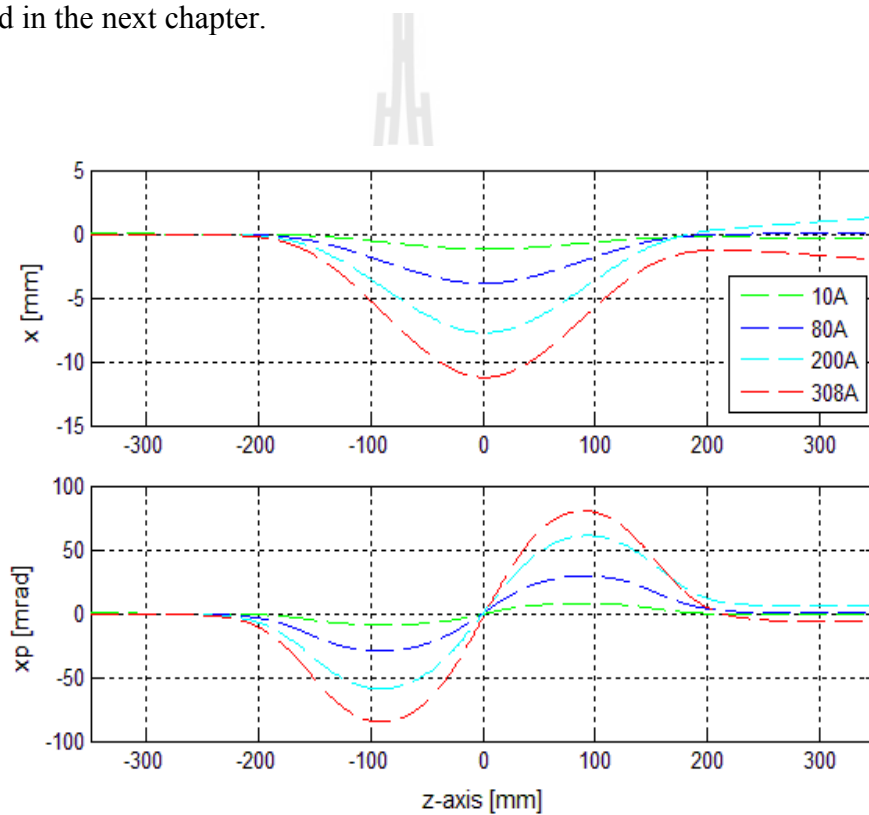


**Figure 3.23** The trajectories in the x-z plane (upper) and y-z plane (lower) of an electron beam passing through the SWLS compared different SWLS current.

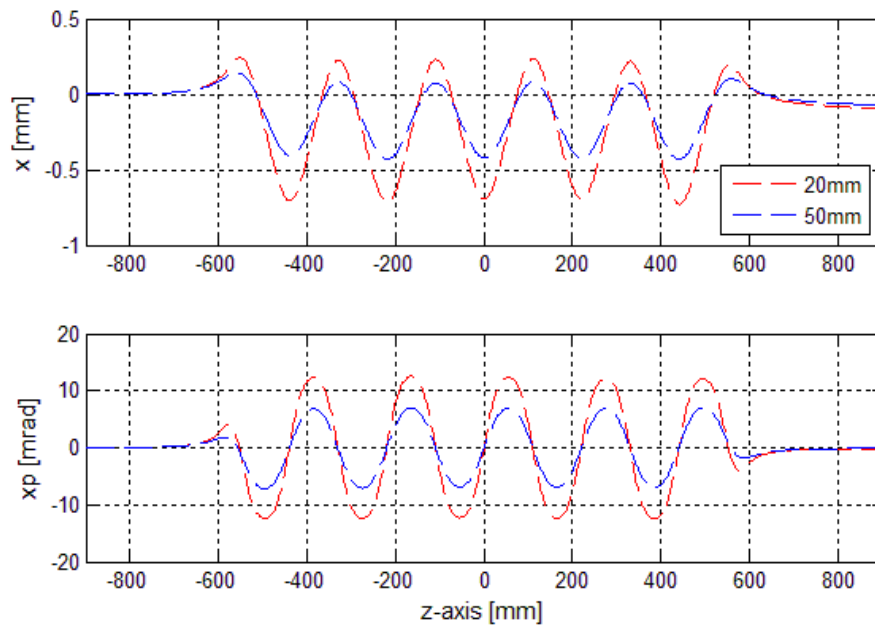


**Figure 3.24** The trajectories in the x-z plane (upper) and y-z plane (lower) of an electron beam passing through the MPW compared between gap of 20 and 50 mm.

**Table 3.4** The electron's trajectories pass through the SWLS and MPW.

	B-field [T]	Displacement [mm]	Angle deviation [mrad]
<i>Superconducting wavelength shifter</i>			
I = 10 A	0.78	1.2015	8.8759
I = 80 A	2.43	3.8836	29.4099
I = 200 A	4.62	7.7436	60.9199
I = 308 A	6.48	11.2455	85.0986
<i>Hybrid multipole wiggler</i>			
Gap = 20 mm	2.38	0.7288	12.5329
Gap = 50 mm	0.86	0.4312	7.1990

## **CHAPTER IV**

### **RESEARCH METHODOLOGIES**

This chapter explains the research methodologies of optimization, simulation, and commissioning of two insertion devices at the SPS storage ring. The aim is to study and minimize the effects of these insertion devices on the beam dynamics. It is divided into three main topics; the optimization of the operating point using Frequency Map Analysis (FMA), the beam optics correction and the beam optics correction commissioning process. This methodology is important for the successful operation of the electron beam with the two insertion devices for beamline users.

#### **4.1 Operating point optimization**

The operating point is chosen away from the dangerous resonance lines so that both fractional tunes are not integers. With the operating point held constant during operation, the nonlinear optics can be set to compensate the chromaticity dependent tune shifts and beta beating. Some techniques can be used to improve the lifetime are

- i. Increase the betatron coupling by observing the operating point.
- ii. Increasing the RF voltage which is used to compensate for the energy lost by the emitted synchrotron radiation.
- iii. The ultimate lifetime improvement is obtained by using a full energy injection mode of operation.

For the SPS storage ring, full energy injection and an upgrade of the RF voltage will be done soon. At present, increased coupling can be possibly used to increase the beam lifetime. Tune scanning is useful for beam lifetime optimization together with luminosity optimization. To do this there are two processes that need to be studied:

1. Observation of the operation point (Frequency Map Analysis).
2. New operation point selection.

#### **4.1.1 Observation of the operation point (Frequency Map Analysis, FMA)**

The betatron tunes of the SPS storage ring are observed by changing the quadrupole magnets' strengths in the SPS storage ring. The nominal operating point is located at  $\nu_x = 4.768$  and  $\nu_y = 2.813$  on the tune diagram, figure 4.1. The horizontal tune will be scanned in the ranges of 4.7 to 4.9 and the vertical tune will be scanned in the ranges of 2.7 to 2.9. To get high machine performance represented by high brilliance, high beam stability and long lifetime, optimization of the beam optics parameters will be carried out using a tune scan at the normal operating beam energy of 1.2 GeV with the SWLS and MPW. Observation of the operating point is started with the SPS storage bare ring. The Matlab Middle Layer, MML program (Gregory *et al.*, 2006) is used to connect magnet parameters to real machine setting. The tunes are scanned using two families of quadrupole magnets, QF1 and QD2, using the following method. This method is called "Tune response".



1. The tune response of a bare ring is measured for fitting the tune to the target tune ( $v_x, v_y$ ).

**Table 4.1** The tune response procedure of adjusting the QF1 and QD2 magnet currents.

Step	QF, Focusing Quadrupoles Current [A]	QD, Defocusing Quadrupoles Current [A]	Measured betatron tune
1	$I_{QFi}$	$I_{QDi}$	$v_{xi}, v_{yi}$
2	$I_{QF1} = I_{QFi} - 0.5A$	$I_{QDi}$	$v_{x1}, v_{y1}$
3	$I_{QFi}$	$I_{QD2} = I_{QDi} - 0.5A$	$v_{x2}, v_{y2}$

Where  $I_{QFi}$  and  $I_{QDi}$  are the initial quadrupole currents at the set operating point.

The response matrix tune method is useful for the approximation of quadrupole magnet currents to achieve the target tune, as follows

$$\begin{bmatrix} a & b \\ c & d \end{bmatrix} \begin{bmatrix} I_{QF} \\ I_{QD} \end{bmatrix} = \begin{bmatrix} v_x \\ v_y \end{bmatrix} \quad (4.1)$$

Where the operating currents of the quadrupole magnets are determined by  $I_{QF0}$  and  $I_{QD0}$  that are used in the real machine, and  $a, b, c,$  and  $d$  are defined by

$$\left. \begin{aligned} a &= \frac{v_{x1} - v_{xi}}{I_{QF1} - I_{QFi}} = \frac{\Delta v_x}{-0.5}, & b &= \frac{v_{x1} - v_{xi}}{I_{QD2} - I_{QDi}} = \frac{\Delta v_x}{-0.5} \\ c &= \frac{v_{y1} - v_{yi}}{I_{QF1} - I_{QFi}} = \frac{\Delta v_y}{-0.5}, & d &= \frac{v_{y1} - v_{yi}}{I_{QD2} - I_{QDi}} = \frac{\Delta v_y}{-0.5} \end{aligned} \right\} \quad (4.2)$$

The matrix 4.1 can be reformed into the equations

$$\begin{aligned} aI_{QF} + bI_{QD} &= v_x \\ cI_{QF} + dI_{QD} &= v_y \end{aligned} \quad (4.3)$$

Then the quadrupole currents are estimated the betatron tune,

$$I_{QD} = \frac{av_y - cv_x}{(ad - bc)} \quad (4.4)$$

$$I_{QF} = \frac{vx - b \left[ \frac{av_y - cv_x}{(ad - bc)} \right]}{a} \quad (4.5)$$

2. The tunes are scanned in steps and for each step a frequency map is calculated by setting the focusing and defocusing quadrupole magnets from the tune response. With the horizontal working point in the range 4.7 to 4.9 and the vertical working point in the range 2.7 to 2.9, as shown in Figure 4.1, the resonance lines up to the 4th-order are drawn out.

- a. The horizontal tune is scanned in steps of 0.01
- b. The vertical tune is scanned in steps of 0.01

Each step of tune scan will adjust the quadrupole magnets' currents in order to change the tune. It will control the electron orbit as well.

3. Wait for 15 minutes.
4. The betatron tune is measured and then the beam lifetime and beam loss monitor values are recorded.

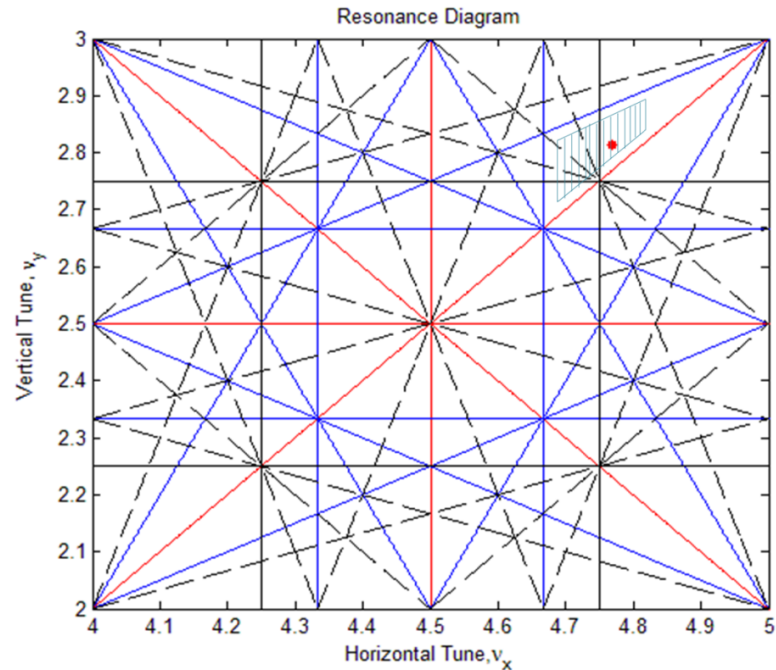


**Figure 4.1** Tune diagram; the green area is the studied location.

#### 4.1.2 Operation point selection

After the betatron tune and beam lifetime have been observed, there are 80 points within the green area to investigate. And then the operating point has to be chosen. It is chosen with respect to beam lifetime and beam stability. The tune shifts caused by the insertion devices (IDs) will cross some dangerous resonance lines when the magnetic field of the IDs is increased and the beam will be lost. To avoid this risk, the operating point has to be chosen to be far away from dangerous resonance lines. The optics should be well optimized by going through these different optimization steps.

1. Choose the operating point: This first step should be a good choice for the machine tunes. The point should be chosen in a region, on the tune diagram, where the beam has a long lifetime. The tunes have to achieve the minimum sensitivity to

field errors. The new operating point should be positioned where the amplitudes of the 3<sup>rd</sup> order resonance terms are as small as possible - aspects that guarantee high brilliance and beam stability. A good point choice prevents any tune coupling. That means avoiding the 2<sup>nd</sup> resonance line would produce the beam stability.

2. Calculate the optical beam parameters for the chosen operating point tune which has a longer beam lifetime. The beam optics has a small vertical betatron function in the insertion device section (to minimize the beam dynamic effects caused by the IDs). It should have a low dispersion function in the long straight. The dynamic aperture, which is corrected with a chromaticity of +2 should be larger than the physical one. This optimization will result in increasing the transverse stable area available for beam oscillations. Measure the coupling to estimate the emittance ratio of the new lattice that has a longer beam lifetime. The beam size should also be observed to check the beam intensity. Then the new strengths of the quadrupole magnets are calculated by converting from the quadrupole magnet currents.

## 4.2 Beam optics calculation

In the 1.2 GeV SPS storage ring, the insertion devices were installed for the production of hard X-rays. The IDs will have a vertical focusing effect on the stored electron beam. Without further correction this causes a vertical tune shift and vertical beta-beating. These perturbations of the design optics can lead to a reduction of the beam dynamic aperture and lifetime.

### 4.2.1 Calculating model

In general, the magnetic fields of insertion devices can be approximated by a Hard Edge Model (Wiedemann, 1999), but in this study, we can calculate the effects of inserting the IDs, using a piecewise hard-edge model (Chao, 2010) implemented by simulation programs such as MAD-X and TRACY-2 (Bengtsson, 1997), to calculate and match the effects on the beam dynamics. In this model, each magnetic pole of the ID is separated into 5 discrete dipole magnets as shown in Figure 4.2. The approximate value of the ID's focusing field is shown by Equations 4.6 to 4.8. The beam's betatron tunes, emittance and energy spread in the presence of IDs can be derived directly from the results of the program.

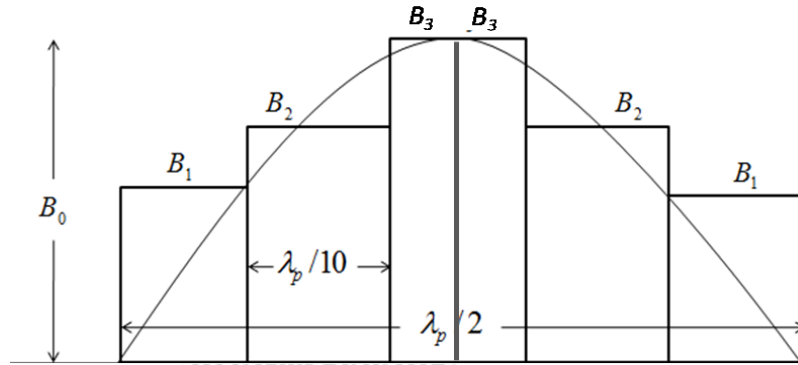


**Figure 4.2** The piecewise hard edge model of an insertion device.

The deflection angle of pieces hard edge model can be defined by

$$\theta_1 = \frac{0.309B_w L}{3.356E} \frac{L}{5}, \quad (4.6)$$

$$\theta_2 = \frac{0.809B_w L}{3.356E} \frac{L}{5}, \quad (4.7)$$

$$\theta_3 = \frac{B_w L}{3.356E} \frac{L}{10}. \quad (4.8)$$

Let  $B_w$  be the magnetic field of a magnet in T,  $E$  is the beam energy of the storage ring in GeV, and  $L$  is the length of the ID in meters, (it can be defined as  $\lambda/2$ ). The pole lengths of MPW are 0.111 and 0.1 meter for nine center poles and two side poles. The SWLS length of main pole and two side poles magnets are constant 0.1615 and 0.143, respectively. The piecewise hard edge model parameters of the MPW and SWLS as summarized in Table 4.2.

**Table 4.2** The angle parameters of the insertion devices at a beam energy of 1.2 GeV.

Parameters	2.18 T MPW	4.0 T SWLS	4.6 T SWLS	6.5 T SWLS
<i>Main poles</i>				
$\theta_1$ , rad	0.0045	0.0136	0.0154	0.0216
$\theta_2$ , rad	0.0117	0.0355	0.0402	0.0564
$\theta_3$ , rad	0.0072	0.0220	0.0249	0.0349
<i>Side poles</i>				
$\theta_1$ , rad	0.0033	0.0068	0.0077	0.0108
$\theta_2$ , rad	0.0088	0.0178	0.0201	0.0282
$\theta_3$ , rad	0.0054	0.0110	0.0124	0.0174

#### 4.2.2 Beam optics calculation and compensation

The beam dynamics effects of the SWLS and MPW are calculated and compensated by using MAD-X codes and then the quadrupole and sextupole strengths are corrected. This is illustrated in Figure 4.4. From the operating point optimization procedure above, we will know the new quadrupole magnet strengths. They will be

the initial values for the beam optics correction. In this work, the optical function changed by effects of the IDs were corrected to give the same optical functions as the unperturbed lattice. In order to find the best solution for the matching conditions using MAD-X program as the flow chart in Figure 4.3. To correct the effects from IDs, we propose to minimize the optic functions in the ID location. This procedure can apply to local/global compensation for any given set of two IDs. MAD-X consists of the input and output files. The input files are included “.seq” and “.madx”. The SPS lattice and initial magnets parameters (bending magnets, quadrupole magnets, steering magnets, and RF cavity) will be put in “filename1.seq”. The “filename2.madx” contains the insertion device parameters, matching betatron function/tune codes, calculating beam optics codes. It can run in command prompt on Windows.

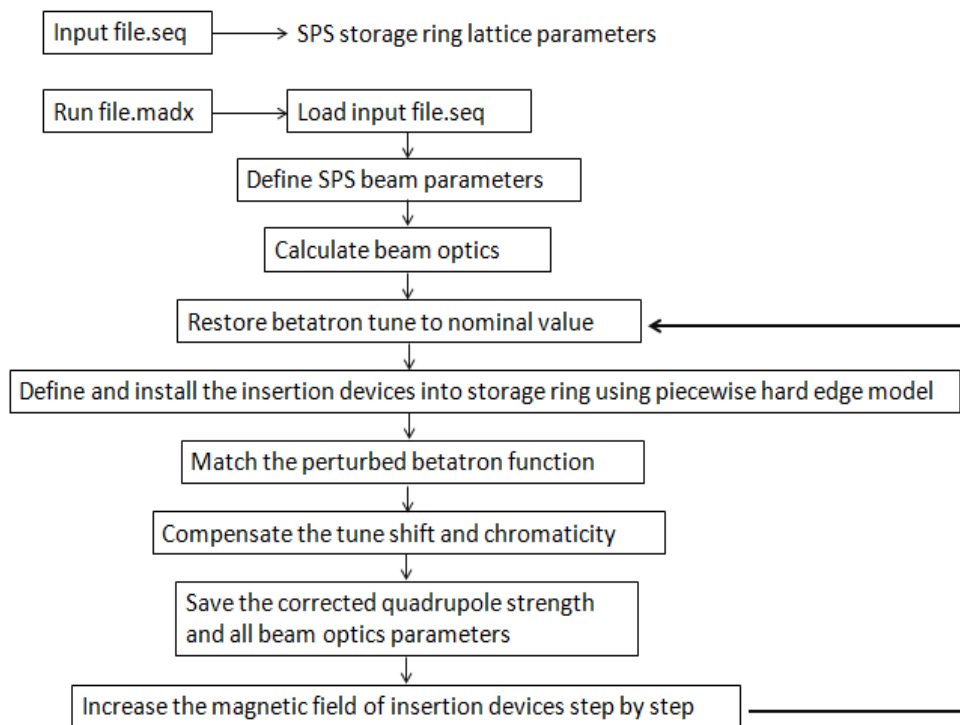


**Figure 4.3** Flow chart of the MAD-X calculation.

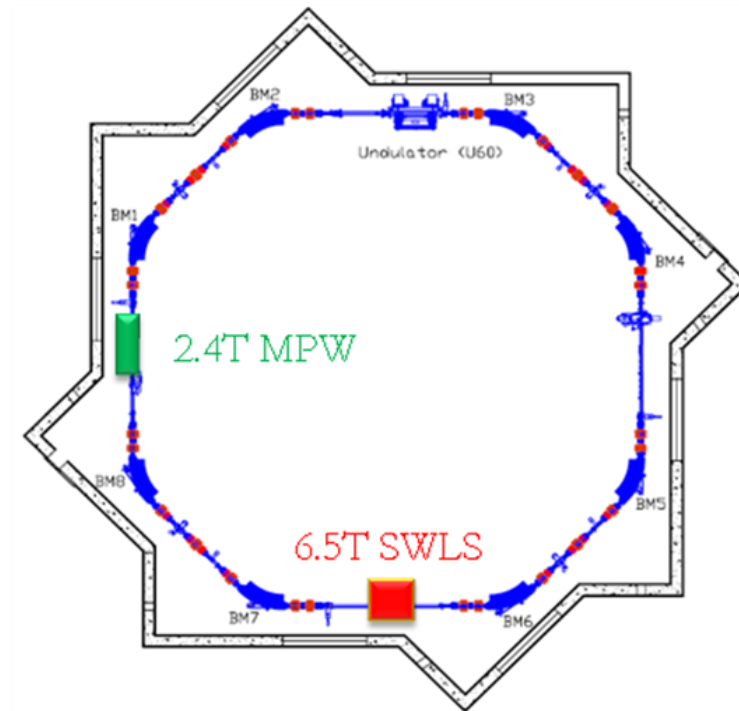


Figure 4.4 The SPS storage ring layout.

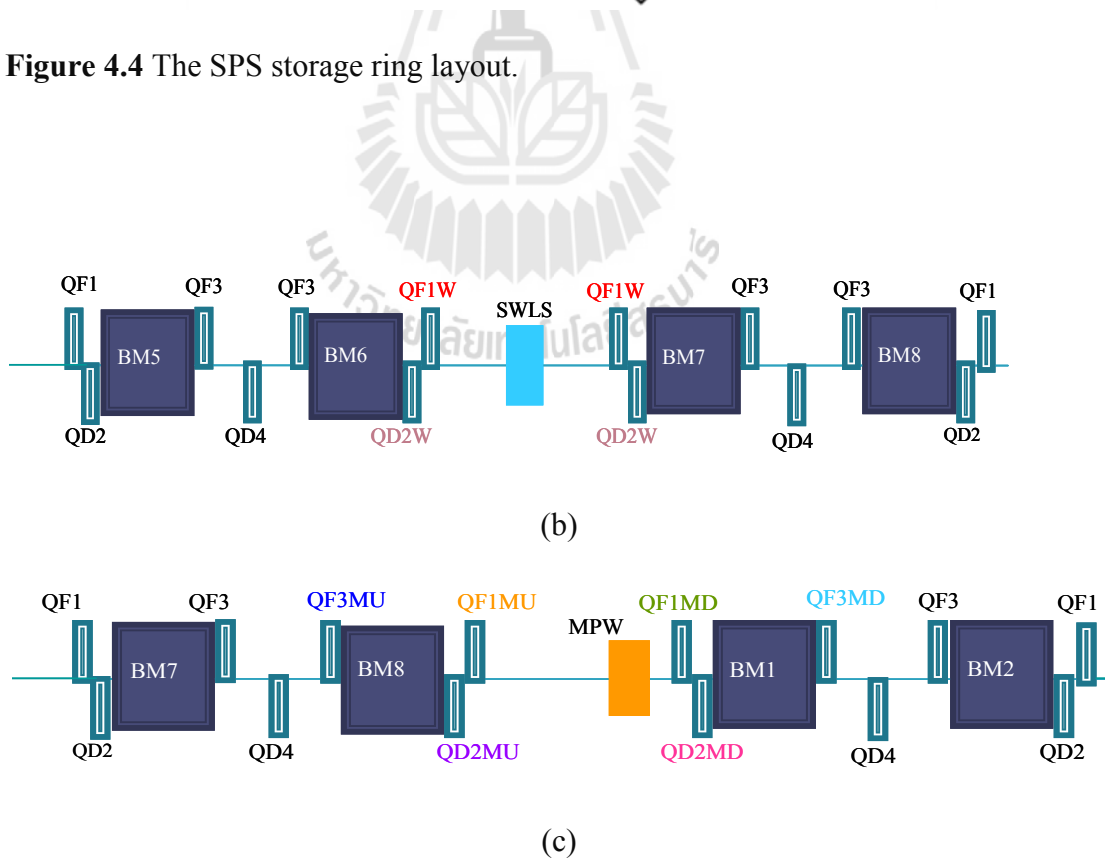


Figure 4.5 (a) SWLS installation and (b) MPW installation.



### **Betatron function matching**

Local corrections to the lattice functions are made with the quadrupole magnets nearest to the insertion devices. The SWLS was installed in the middle of a long straight section between BM06 and BM07. The local corrections are performed using the two pairs of quadrupole magnets, QF1W and QD2W, adjacent to the SWLS in Figure 4.5(a). The MPW was inserted in right part of the long straight section 1 between BM08 and BM01. It is shifted from the center of section 1 toward BM01 by 1.168 m. The location of the MPW is therefore not at the middle of the straight section due to limitation of space in the SPS storage ring. There are six independent quadrupole magnets, QF1MU, QD2MU, QF3MU, QF1MD, QD2MD, and QF3MD, adjacent to the MPW, which can be used to match the betatron function in Figure 4.5(b). The matching betatron function can be calculated by the MAD-X program. Therefore our goal is to change the quadrupole magnet strengths bounding the ID straight section in order to minimize the perturbation in the optics.

### **Betatron tune correction and chromaticity compensation**

The betatron tune correction is called the global correction and uses the MAD-X code. It is used to restore the betatron tunes back to their original values and is done using the two families of QF1 and QD2 quadrupole magnets for both insertion devices. The two families of sextupoles, SF, SD can also be used to correct the chromaticities during the commissioning. If the two IDs are used without any corrections, the effects will produce a beam instability because the tune is located close to a resonance line.

### Dynamic aperture simulation

The TRACY-2 program is chosen to estimate the dynamic aperture (DA) following the flow chart tracking procedure as summarized in Figure 4.6. As has been mentioned in the beam corrections section above, the DA is affected by perturbations of the optics functions in the storage ring. Therefore, the corrected quadrupoles and sextupoles magnets form beam optic corrections after the IDs have been included into the SPS storage ring. The tracking procedure is summarized in Figure 4.6. The input file of SPS beams lattice, IDs parameters, and magnets values setting were defined in “inputfiles.lat”. The TRACY-II will generate the output files of ‘outputfile.out’. All beam optics parameters are included in the output file.

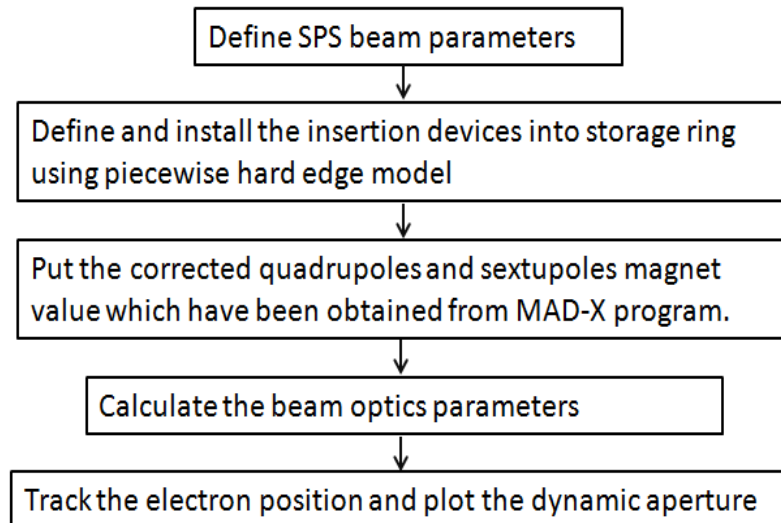


**Figure 4.6** Flow chart of the TRACY-II tracking.

### Electron orbit correction

The deflected angle and position of an electron beam at the exit of the IDs in chapter 3 were compensated for in both planes by steering magnets, shown in Figure 4.7, located at both ends of the two IDs. The calculation of field error and the magnetic field of the steering magnets are determined by Figure 4.8.

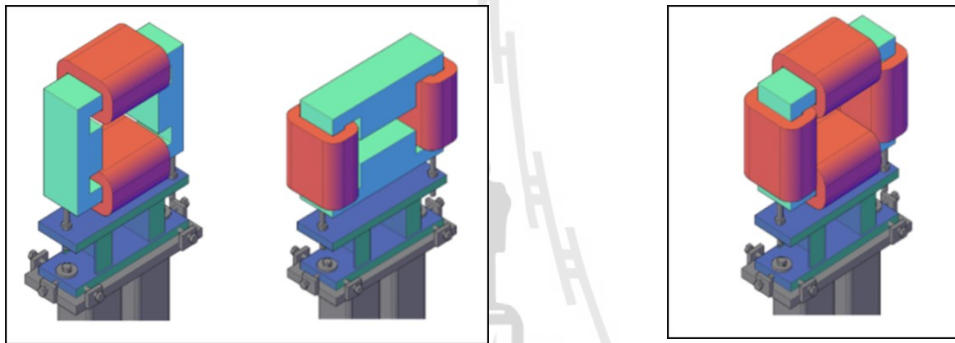


**Figure 4.7** The steering magnets adjacent to two IDs. SWLS (left) and MPW (right) steering magnets.

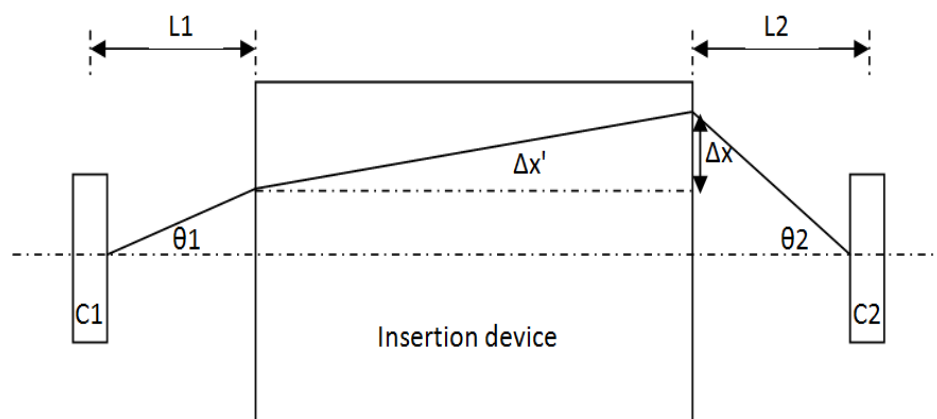


**Figure 4.8** The top view layout for the deviated angle and position deviation of an electron passing through an insertion device.

The deflection angle and position of an electron as it passes through an insertion device can be written as

$$\left. \begin{aligned} \Delta x' &= 0.2498 \int_{-L}^L B_y ds \\ \Delta x &= -0.2498 \int_{-L}^L s B_y ds \end{aligned} \right\} \quad (4.9)$$

Where  $\int_{-L}^L B_y ds$  and  $\int_{-L}^L s B_y ds$  are the first and second magnetic field integrals.

Then the angle by which the electron is shifted from the central orbit in Figure 4.8 can be given by

$$\theta_1 = \frac{-(\Delta x + \Delta x' L_2)}{L_1} \quad (4.10)$$

$$\theta_2 = -(\theta_1 + \Delta x')$$

From Equations 4.9 and 4.10, the magnetic fields of the corrector magnets, adjacent to the insertion devices and used to correct the electron trajectory are defined by

$$b = \frac{B \rho \theta}{l_{eff}} \quad (4.11)$$

The calculated steering magnet's current in amps becomes

$$I = \frac{b}{B - \text{slope}} \quad (4.12)$$

**Table 4.3** Steering magnet parameters for the SWLS and MPW.

Magnet	B-I slope (T/A)	$B_0$ (T)	$L_{\text{eff}}$ (mm)
STH-SWLS	0.004288	0.05591	183.405
STV-SWLS	0.001447	0.01861	242.933
STV-MPW	0.001071	0.01366	314.474
STH-MPW	0.001315	0.01683	284.004

### 4.3.3 Beam compensation process

The effects of the SWLS and MPW on beam dynamics such as betatron function changes, tune shifts, increased energy loss, dynamic aperture reduction, and emittance blow up are evaluated using programs such as MAD-X (Grote, 2011) as follows:

1. Starting with a 1.0 GeV SPS ring, the SWLS current is increased, until the SWLS current reaches its maximum value of 308 A (6.5 Tesla). The corrected strengths of the quadrupole magnets, betatron/dispersion function, tune shift, emittance, and energy loss are now calculated which correspond to SWLS current values of

- i. 0 to 10 A in steps of 1 A,
- ii. 10 to 300 A in steps of 10 A,
- iii. 300 to 308 A in steps of 2 A.

2. The beam energy is then ramped up from 1.0 to 1.2 GeV using all magnet currents including the SWLS. During each beam energy ramping step, the effects on beam dynamics are corrected to the original bare ring value
  - i. with 170 A SWLS current,
  - ii. with 200 A SWLS current,
  - iii. with 308 A SWLS current.
  
3. At a beam energy of 1.2 GeV using the SWLS, the perturbation and compensation were investigated as a function of MPW gap by decreasing the MPW gap in the SWLS current ranges of
  - i. 170A: close the MPW gap to 23.5 mm,
  - ii. 200A: close the MPW gap to 23.5 mm,
  - iii. 308A: close the MPW gap to 23.5 mm.

The linear effects include closed orbit distortion (COD), mismatch betatron/dispersion, tune shifts, and increased energy loss per turn. The non-linear effects result in a reduction of the dynamic aperture. Due to the SWLS and MPW installations, all perturbations should be compensated for by adjusting the strengths of the nearby quadrupole magnets. Non-linear effects can be compensated for by adjusting the nearby sextupole magnets. In this work, the optical functions changed by the effects of the IDs were corrected to give the same optical functions as the unperturbed lattice. In order to find the best solution for the matching conditions the MAD-X program is used as per the flow chart in Figure 4.2. To correct the effects from IDs, we propose to minimize the optic functions in the ID locations. This procedure can be applied to local/global compensations for any given set of IDs.

### 4.3 Commissioning of insertion devices at SPS

The two IDs were installed successfully in the SPS ring (see Figure 4.9). This section will explain how the commissioning of the two insertion devices at the electron storage ring of the Siam Photon Source (SPS) was carried out. The betatron/dispersion function and betatron tune was measured, after installing the insertion devices, and the COD correction was performed by using the steering magnets. The COD was compensated by adjusting the global steering magnets. It is controlled by the Slow Orbit Feedback (SOFB) system. The SOFB system was developed to control the orbit in SPS storage ring (Klinkhiew *et al.*, 2012) and is very important for the stable provision of light to the beamlines.

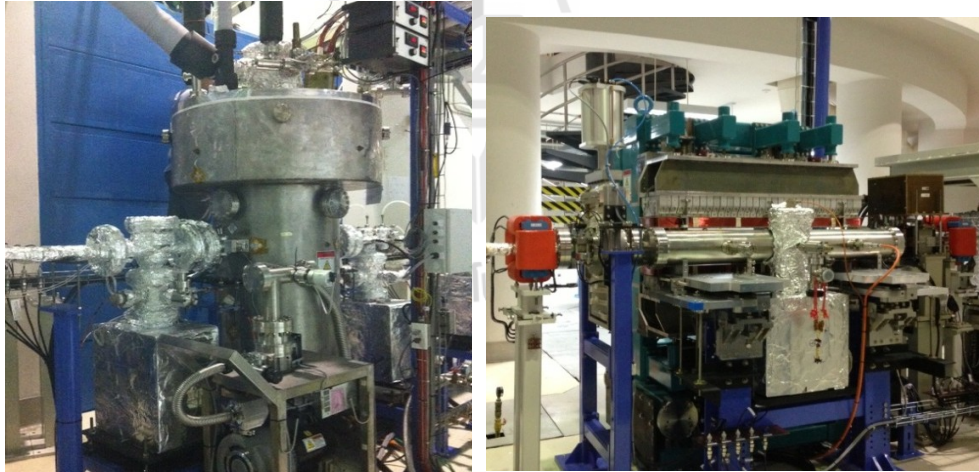


**Figure 4.9** The SWLS (left) and the MPW (right) installed in the SPS ring.

This procedure prevents damage caused by the field errors, including any misalignment of the two IDs and the effects on the beam dynamics caused by the two IDs. Finally, the beam dynamic effects of the IDs were also measured as a reference for adjusting the beam optics. The beam parameters were measured, corrected, and

commissioned by setting the corrected strength of the quadrupole magnets in the real machine. The Matlab Middle Layer (MML) program is used to set all the magnets parameters in the machine. In the real machine, the corrected quadrupole magnet strengths are converted to quadrupole magnet currents using

$$k = \frac{g}{B\rho} I \quad (4.13)$$

Where  $k$  is the focusing strength of the quadrupole magnet in  $m^{-2}$ ,  $g$  is the G/I slope of quadrupole magnets (T/m/A) as shown in chapter I,  $I$  is the quadrupole current, and  $B$  and  $\rho$  are the magnetic field and radius of the bending magnet, respectively. From Equation 4.13, the quadrupole current is defined by

$$I = \frac{B\rho}{g} k \quad (4.14)$$

For the lattice without IDs, the strengths of the quadrupoles ( $k$ ) at beam energies of 1.0 GeV and 1.2 GeV are equal, but the magnetic field of the bending magnets is different. The factor,  $B\rho/g$  of the quadrupole magnets as a function of SPS beam energy,  $E$  in GeV, is as follows

$$F_{QF1} = 386.1750E^3 - 1,277.5481E^2 + 1,530.3888E - 512.6963 \quad (4.15)$$

$$F_{QD2} = -462.3593E^3 + 1,511.9019E^2 - 1,771.5623E + 594.9436 \quad (4.16)$$

$$F_{QF3} = 414.1728E^3 - 1,353.13075E^2 + 1,606.4125E - 539.7451 \quad (4.17)$$

$$F_{QD4} = -302.4070E^3 + 967.3480E^2 - 1,162.5657E + 371.6756 \quad (4.18)$$



**Table 4.4** The factors  $B\rho/g$  of the quadrupole magnets for converting the strength,  $k$  ( $\text{m}^{-2}$ ) to current (A) for a bare ring.

QM	Factor, $B\rho/g$ [ $\text{m}^2.\text{A}$ ]	
	1.0 GeV	1.2 GeV
QF1	122.942	150.870
QD2	-123.669	-152.177
QF3	124.118	154.528
QD4	-122.577	-152.380

All beam parameters have to be recorded during commissioning. There are three main steps to commissioning as listed below.

#### 4.3.1 Beam injection with IDs at a beam energy of 1.0 GeV

The MPW gap is fully opened. The commissioning of the SWLS is done at a beam energy of 1.0 GeV by increasing the SWLS current from 0 to 308 A using the following method:

Step 1: Inject a beam current of 50 mA and store the beam at 1.0 GeV with the MPW gap fully open.

Step 2: Observe and measure the vertical tune shift.

Step 3: Increase the SWLS current.

Step 4: Correct the COD by using the global steering magnets and the corrector magnets adjacent to the SWLS.

Step 5: Correct the betatron function and tune shift by using local and global quadrupole magnets. This correction has to be done in small steps.

Step 6: Observe and measure the vertical tune shift.

Step 7: Repeat steps 5-6 until the tune is as close as possible to the nominal tune.

Step 8: Repeat steps 2-7 until the SWLS current is 308A (current from 0 to 10 A, in steps of 0.1A, current from 10 to 308 A in steps of 10 A).

Step 9: Test the beam injection to the storage ring at the SWLS currents of 170 A, 200 A, and 308 A by adjusting the kicker magnet which is used to kick the electron beam into the storage ring during injection.

#### **4.3.2 Ramping up energy to 1.2 GeV**

After increasing the SWLS current, the beam can be filled into the storage ring without any optical perturbation at 1.0 GeV. Then the electron beam can be ramped up to 1.2 GeV in steps of 0.02 GeV. The process of ramping up the energy is as follows

Step 1: Beam injection at 1.0 GeV with 170A SWLS current.

Step 2: Ramp up the beam energy to 1.02 GeV.

Step 3: Observe and measure the vertical tune shift.

Step 4: Correct the betatron function and tune shift by using local and global quadrupole magnets. This correction has to be done in small steps, adjusting the quadrupole currents by factor of 0.05 each time.

Step 5: Repeat steps 3-4 until the tune is as close as possible to the nominal tune.

Step 6: Repeat steps 2-5 until the beam energy reaches 1.2 GeV (in steps of 0.02 GeV).

Step 7: Wait for 15 minutes and then record the beam lifetime.

Step 8: Repeat steps 1-7 with 200A SWLS current and then again with 308A SWLS current.

#### **4.3.3 Closing the MPW to a minimum gap of 23.5 mm**

The commissioning of both insertion devices at the same time is started by injecting the electron beam at a beam energy of 1.0 GeV, with the SWLS operating. The energy will then be ramped up to 1.2 GeV. The commissioning of the MPW is done at that 1.2 GeV beam energy by adjusting the gap from 180 mm to 23.5 mm stepwise using the following process:

Step 1: Inject and store a beam at 1.2 GeV with the SWLS operating normally.

Step 2: Observe and measure the vertical tune shift.

Step 3: Correct the COD by using the global steering magnets and the corrector magnets adjacent to the MPW.

Step 4: Correct the betatron function and tune shift by using local and global quadrupole magnets. This correction has to be done in small steps, adjusting the quadrupole currents by factor of 0.05 each time.

Step 5: Repeat steps 2-4 until the tune is as close as possible to the nominal tune.

Step 6: Adjust the MPW gap in small steps until the gap is 23.5 mm.

Step 7: Repeat steps 1-6.

Step 8: Wait for 15 minutes and then record the beam lifetime.

During the commissioning process, the effects of the MPW and SWLS on the beam dynamics, and the correction of these effects, have been studied as a function of the magnetic field and beam energy. This has been done in order to implement automatic operation of the machine by including the MPW and SWLS correction data in a ‘Look-forward table’ stored in a Programmable Logic Controller (PLC) program. The PLCs directly control all SPS parameters during machine operation. All the corrected quadrupole current values are set in the real machine using this method. After commissioning, the electron beam is stored with the insertion devices operating and at a beam energy of 1.2 GeV for about 11 hours to observe and record the beam lifetime and beam profiles. Figure 4.10-4.16 show the commissioning procedures and the measured data before machine operation were successfully operated the beam with SWLS and MPW.

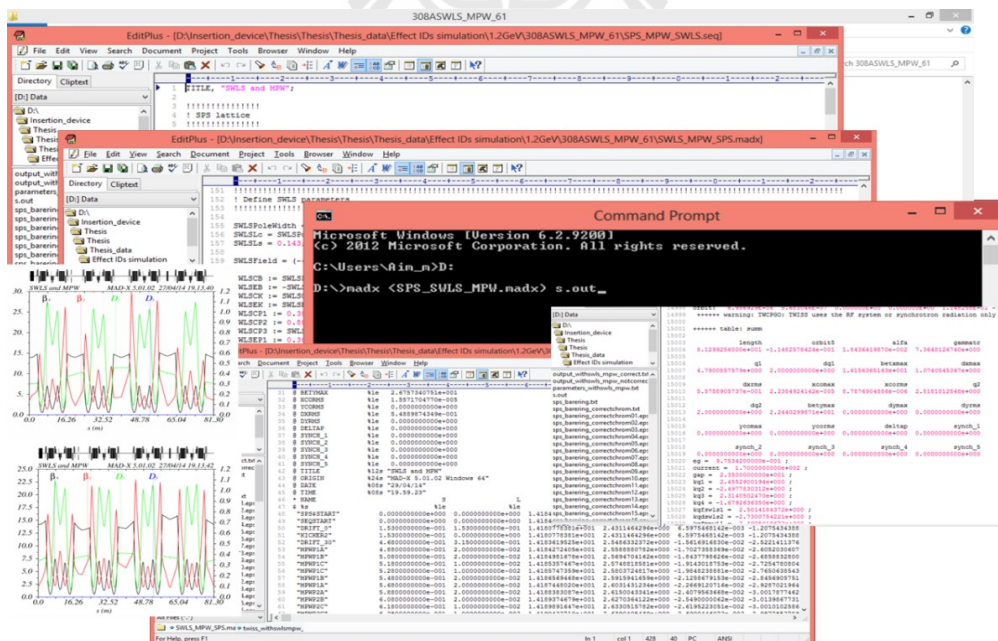


**Figure 4.10** The steps were used to correct beam optics distortion using MAD-X program.

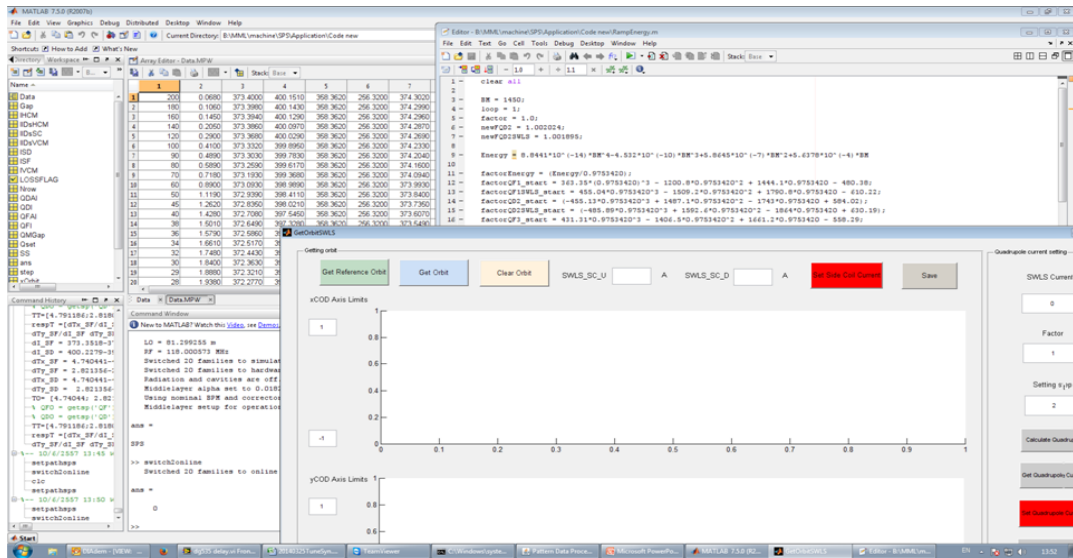


Figure 4.11 The corrected quadruples and steering magnets setting in the machine using MML based on Matlab program for orbit and beam optics correction after including these insertion devices.

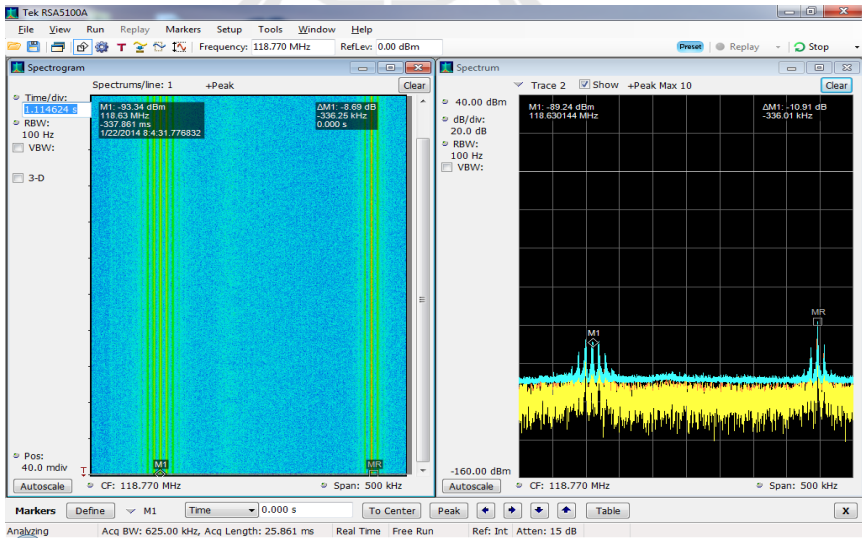
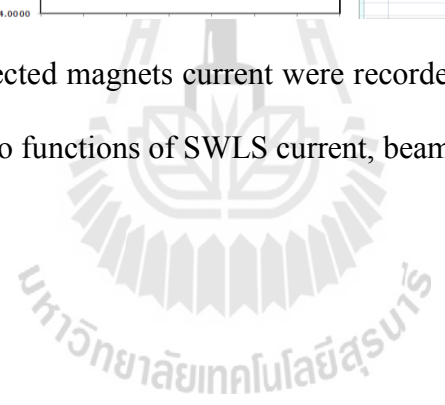
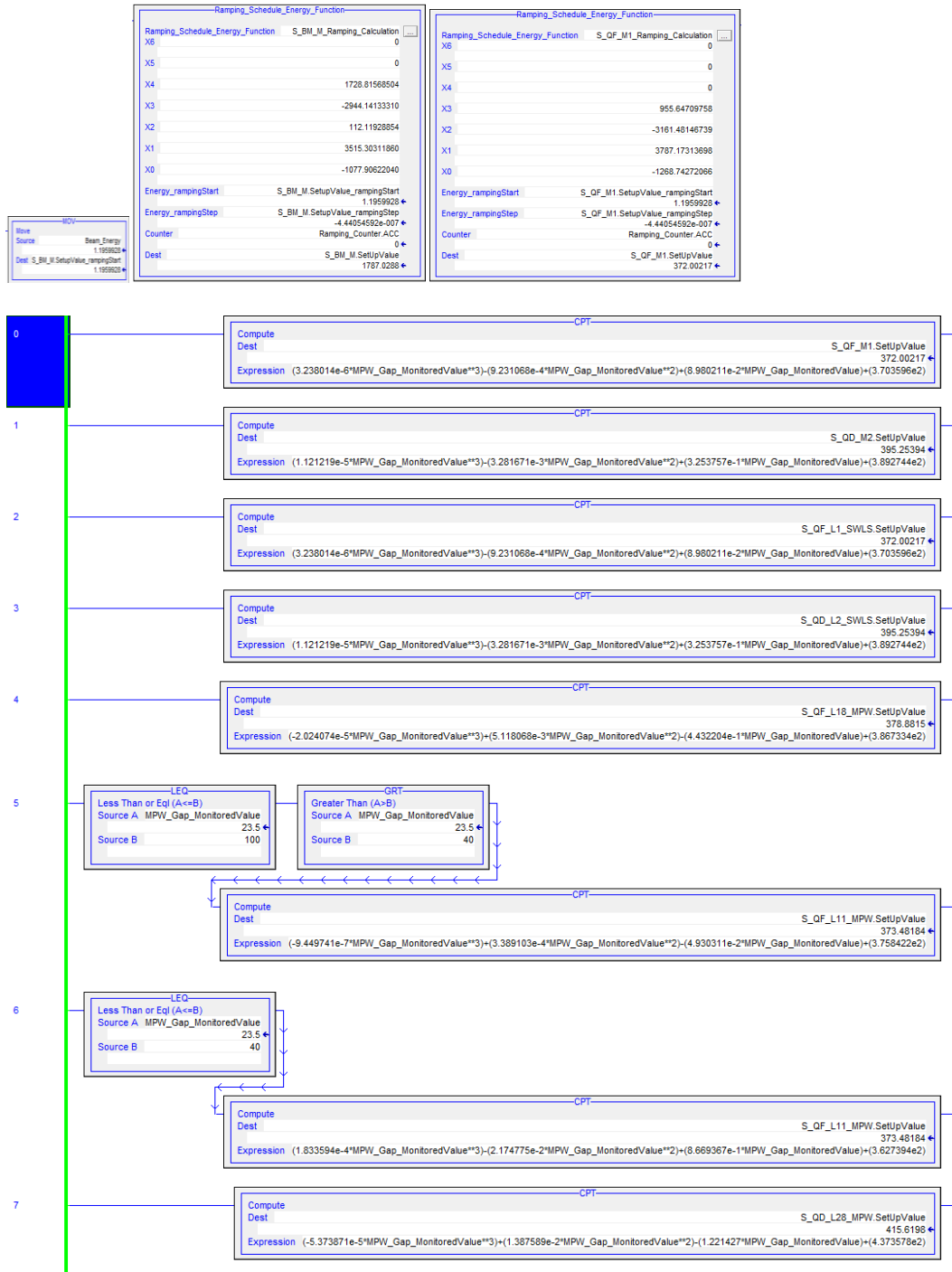


Figure 4.12 The measured and recorded betatron tune during commissioning processes by using the spectrum analyzer. The MR is horizontal and M1 is the vertical frequency oscillations.

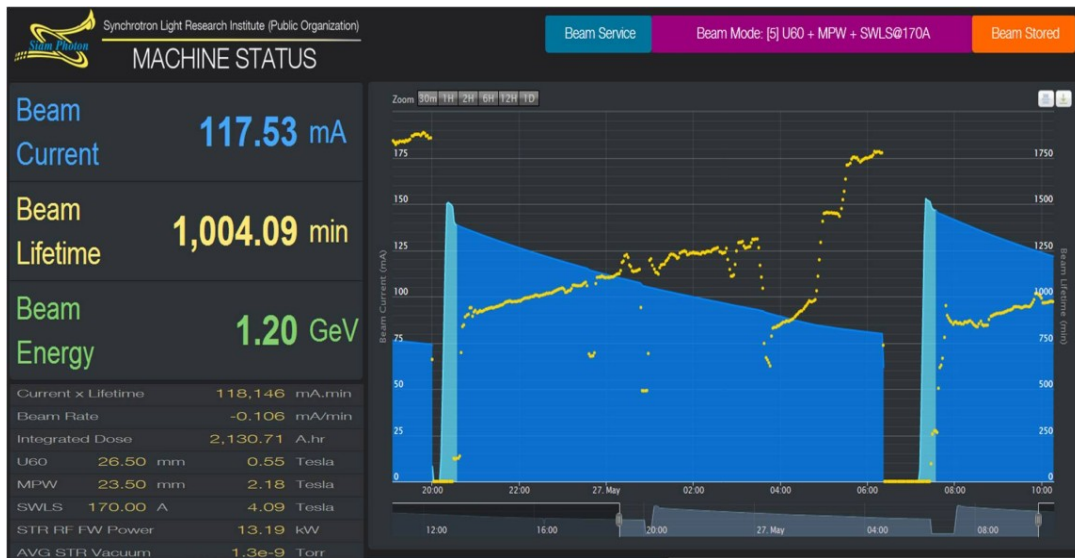
Energy [GeV]	I_SWLS [A]	MPW [mm]	fx	fy	Tunex	Tuney	dTunex	dTuney		BM	QF1	QD2	QF3	QD4	QF1_SWLSQD2_SWLSF11_M			
3																		
4	1.195904	170	120	118.834125	118.698625	4.7738	2.81054	0.0000	0.0000	1787.020020	374.868	396.0005	357.5878	255.8879	377.6152	410.8488	374.83	
5	1.195904	170	100	118.834125	118.70188	4.7738	2.80966	0.0000	-0.0009	1787.020020	374.868	396.0005	357.5878	255.8879	377.6152	410.8488	374.83	
6	1.195904	170	90	118.83588	118.69888	4.7733	2.81047	-0.0005	-0.0001	1787.020020	374.868	396.0005	357.5878	255.8879	377.6152	410.8488	374.83	
7	1.195904	170	80	118.83850	118.69538	4.7726	2.81142	-0.0012	0.0009	1787.020020	374.868	396.0005	357.5878	255.8879	377.6152	410.8488	374.83	
8	1.195904	170	70	118.84425	118.68988	4.7711	2.81292	-0.0027	0.0024	1787.020020	374.868	396.0005	357.5878	255.8879	377.6152	410.8488	374.83	
9	1.195904	170	60	118.8515	118.68113	4.7691	2.81529	-0.0047	0.0047	1787.020020	374.868	396.0005	357.5878	255.8879	377.6152	410.8488	374.83	
10			60a	118.8455	118.68900	4.7707	2.81315	-0.0031	0.0026	1787.020020	374.8378	395.7688	357.7774	256.0775	377.6655	410.7395	374.92	
11			60a	118.83713	118.69625	4.7730	2.81119	-0.0009	0.0006	1787.020020	374.8249	395.6700	357.8582	256.1583	377.6870	410.6929	374.96	
12	1.195904	170	55	118.84075	118.69063	4.7720	2.81271	-0.0018	0.0022	1787.020020	374.8249	395.67	357.8582	256.1583	377.687	410.6929	374.96	
13			55a	118.83625	118.69688	4.7731	2.81102	-0.0007	0.0005	1787.020020	374.7904	395.4575	357.9964	256.2965	377.7246	410.6115	375.02	
14			55a	118.83425	118.70100	4.7738	2.80990	0.0000	-0.0006									
15	1.195904	170	50	118.83975	118.69225	4.7723	2.81227	-0.0015	0.0017	1787.020020	374.7757	395.3669	358.0553	256.3555	377.7406	410.5768	375.05	
16			50a	118.834625	118.70363	4.7737	2.80919	-0.0001	-0.0014	1787.020020	374.7099	395.0433	358.1989	256.4992	377.784	410.4947	375.12	
17			50a	118.833375	118.705875	4.7740	2.80858	0.0002	-0.0020	1787.020020	374.6923	394.9562	358.2376	256.5378	377.7956	410.4726	375.14	
18	1.195904	170	46	118.8385	118.6975	4.7726	2.81085	-0.0012	0.0003	1787.020020	374.6923	394.9562	358.2376	256.5378	377.7956	410.4726	375.14	
19			46a	118.837125	118.70125	4.7730	2.80983	-0.0008	-0.0007	1787.020020	374.6622	394.8293	358.2724	256.5726	377.809	410.4568	375.16	
20	1.195904	170	40	118.844625	118.684	4.7709	2.81451	-0.0028	0.0040	1787.020020	374.6622	394.8293	358.2724	256.5726	377.809	410.4568	375.16	
21			40a	118.843	118.68775	4.7714	2.81349	-0.0024	0.0029	1787.020020	374.6	394.5942	358.3037	256.6039	377.8304	410.462	375.21	
22			40a	118.841	118.695625	4.7719	2.81136	-0.0019	0.0008	1787.020020	374.4936	394.1922	358.3572	256.6575	377.867	410.4709	375.30	
23			40a	118.840125	118.69725	4.7722	2.81092	-0.0016	0.0004	1787.020020	374.4482	394.0208	358.3801	256.6803	377.8827	410.4747	375.33	
24			40a	118.83925	118.702375	4.7724	2.80953	-0.0014	-0.0010	1787.020020	374.4073	393.8665	358.4006	256.7008	377.8967	410.4781	375.37	
58																		
59	QF1			$y = 2.410618E-05x^3 - 4.936060E-03x^2 + 3.313828E-01x + 3.674925E+02$						60	1787.020020	374.8126	395.6351	357.8468	256.1469	377.687	410.7035	374.97
60	QD2			$y = 8.588882E-05x^3 - 1.698951E-02x^2 + 1.137272E+00x + 3.700090E+02$						55	1787.020020	374.7976	395.4554	358.0359	256.3361	377.7328	410.5891	375.02
61	QF3			$y = -4.803376E-06x^3 + 8.388476E-05x^2 + 2.093760E-04x + 3.585698E+02$						50	1787.020020	374.7348	395.1349	358.1896	256.4898	377.7751	410.4876	375.09
62	QD4			$y = -4.808996E-06x^3 + 8.443105E-05x^2 + 1.892351E-04x + 2.568703E+02$						46	1787.020020	374.6378	394.7338	358.2894	256.5896	377.8152	410.4419	375.18
63	QF1_SWLS			$y = -1.721335E-05x^3 + 2.773328E-03x^2 - 1.570712E-01x + 3.808493E+02$						40	1787.020020	374.3929	393.8135	358.405	256.7052	377.901	410.4796	375.39
64	QD2_SWLS			$y = -5.224075E-05x^3 + 8.875836E-03x^2 - 4.793566E-01x + 4.187859E+02$						38	1787.020020	374.2801	393.4054	358.4353	256.7356	377.9398	410.5305	375.48
65	QF11_MPW			$y = -2.528261E-05x^3 + 4.664692E-03x^2 - 2.951182E-01x + 3.813511E+02$						32	1787.020020	373.8321	391.8189	358.505	256.8052	378.0983	410.8335	375.85
66	QD21_MPW			$y = -8.002031E-05x^3 + 1.575969E-02x^2 - 9.287277E-01x + 4.119543E+02$						28	1787.020020	373.4305	390.4183	358.536	256.8362	378.2473	411.1858	376.18
67	QF31_MPW			$y = -9.430922E-06x^3 - 6.586787E-04x^2 + 1.306562E-01x + 3.544052E+02$						26	1787.020020	373.1954	389.6027	358.5475	256.8478	378.3374	411.1415	376.3
68	QF18_MPW			$y = -1.443370E-05x^3 + 4.852444E-03x^2 - 4.039490E-01x + 3.847476E+02$						23.5	1787.020020	372.8669	388.4671	358.5587	256.859	378.4661	411.7547	376.66
69	QD28_MPW			$y = -6.159528E-05x^3 + 1.786167E-02x^2 - 1.403245E+00x + 4.291903E+02$														
70	QF38_MPW			$y = -9.700388E-07x^4 + 5.207567E-04x^3 - 1.853008E-02x + 3.568216E+02$														
71	VCM_UP			$y = -1.613417E-05x^3 + 2.904940E+00$														
72	VCM_DOWN			$y = -1.613417E-05x^3 + 2.904940E+00$														
73	HCM_UP			$y = -1.186231E-04x^3 + 1.490591E+00$														
74	HCM_DOWN			$y = -1.186231E-04x^3 + 1.490591E+00$														
75																		
76																		
77																		
78																		
79																		
80																		
81																		

Figure 4.13 All corrected magnets current were recorded during commissioning and they were generated to functions of SWLS current, beam energy, and MPW gap.





**Figure 4.14** The magnet current values as a functions of SWLS current, beam energy, and MPW gap which were put in PLC ladder program for machine operation. All operated magnets parameter were set in this program.



**Figure 4.15** The beam lifetime and beam current on website (<http://accelerator.slri.or.th>).

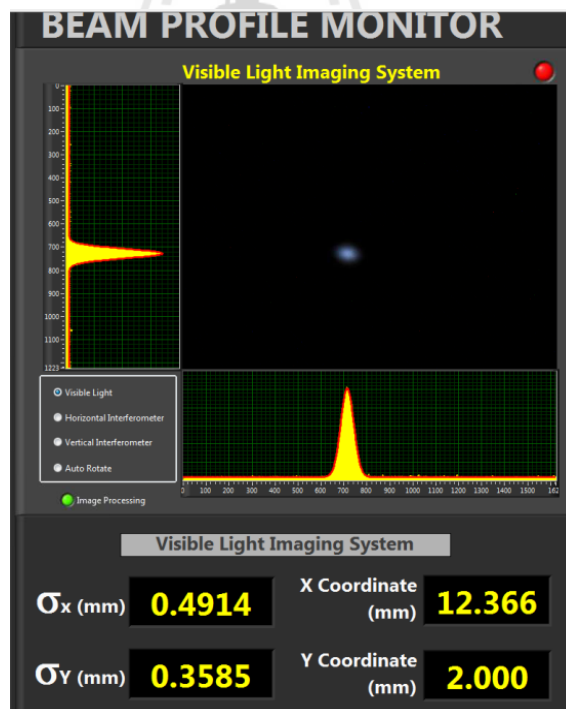


**Figure 4.16** Measured beam profile which is calculated by the gaussian fitting.



## CHAPTER VI

### RESULTS AND DISCUSSION OF SWLS AND MPW

The Siam Photon Source (SPS) with the electron storage ring contains three insertion devices (IDs); undulator, hybrid multipole wiggler, and superconducting wavelength shifter. They were commissioned with a beam in December 2013. Two high field IDs can generate the synchrotron radiation in range of hard X-ray for the requirement of the beamline user. Including the two insertion devices will have effect to the beam dynamics. Thus, the betatron function distortions can be compensated almost perfectly by adjusting local quadrupole magnets. The betatron tunes are corrected to remain unchanged by using the global quadrupole magnets correction. At emittance of 61 nmrad (4.768/2.813), 308A SWLS and 23.5 mm MPW had been commissioned. The beam current is lower than 50 mA after operating for 11 hours. If SWLS and MPW are operated together, the beam current is not enough for user service. User service needs to operate two IDs together at the same time thus the new operating point is observed. From the Frequency Map Analysis (FMA), the operating point at 4.790/2.818 on resonance diagram has long beam lifetime. It is increased by 30% compared with operating point (4.768/2.813). After commissioning 4.0 Tesla SWLS and 4.6 Tesla SWLS with 2.18 Tesla MPW, the beam lifetimes are 13 and 11 hours, respectively. The SWLS and MPW have small effect on beam lifetime after correction. The emittance and beam size are also increased by the effects of IDs.

## 5.1 Observation of operating point

An important issue is the observed reduction of beam lifetime due to the increasing of the magnetic field. The working point of the betatron oscillations on the resonance diagram corresponds to betatron tunes  $\nu_x = 4.768$  (horizontal) and  $\nu_y = 2.813$  (vertical). At SPS, the measurement of the beam lifetime is performed using the DCCT signal. The total beam lifetime defines the time when the beam current reduce by

$$I = I_0 e^{-t/\tau} \quad (5.1)$$

The beam lifetime is dependent with respect of the vertical and horizontal apertures and RF cavity voltage. Presently, the achievable voltage in the RF cavities of SPS is 125 keV which is equivalent to 8 hours at 100 mA. In general the measured lifetime does not fit the model which is optimistic by a factor around 30%. The beam lifetime at 150 mA stored current is about 11 hours without insertion devices (IDs). This can go down by 30-40% to 3 – 5 hours after installing two IDs at the maximum peak fields. The beam lifetime reductions have effects strongly depending on the machine tune and on the beam optics distortion cause by the IDs. The dynamic aperture is sensitive to the betatron tune and betatron function. The SPS storage ring has been run with measured vertical chromaticity at +3 until recently. However, the measured chromaticity in the SPS storage ring were not performed at the studied chromaticity values in the simulations at +2.

Any change of the phase space of a particle beam will affect the beam loss rates. By observing the beam lifetime as a function of the tune, the phase space area of the lattice can be investigated by using FMA. The nominal working point was chosen to provide a good dynamic aperture in the storage ring with several solutions

providing good beam lifetime. After optimizing operating point, beam lifetime increases to 16 hours.

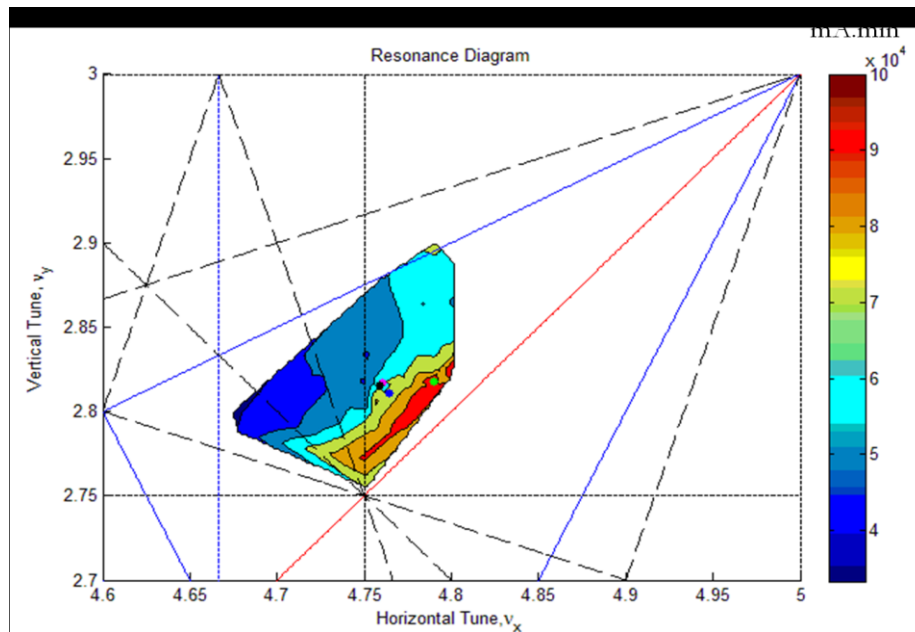


**Figure 5.1** Contour plot of measured beam lifetime [mA\*min] scan over a range of vertical and horizontal betatron tune (FMA).

The beam lifetime as a function of the horizontal and vertical betatron tunes,  $v_x$  and  $v_y$  are measured and plotted on the tune diagram. The product current  $\times$  lifetime is presented in a color contour with the horizontal and vertical of the tune as shown in Figure 5.1. The scale shown the scan indicates the lifetime, in mA\*min. Much larger regions of lifetimes over 20 hours can also be seen in the red region. In order to be higher beam lifetime, the operating betatron tunes for new operating point have been chosen to be horizontal of 4.790 and vertical of 2.818. The compared locations of betatron tune are shown in Figure 5.2. The new tune point is moved close to the coupling resonance so the vertical beam size increases as given by the formula for the

coupling ratio. The coupling ratio can be controlled by the multipole magnet, which has been used as a skew quadrupole. Normally, the working point has to be chosen away from the coupling resonance lines due to the low emittance for higher brightness. Now, we choose the working point from beam lifetime consideration because of the limitation of RF voltage. The main parameters are listed in Table 5.1.

**Table 5.1** Compared beam optic parameters between two operating points.

Parameter	Old operating point	New operating point
Betatron tunes, $\nu_x, \nu_y$	4.768, 2.813	4.790, 2.818
Natural energy spread	0.0006	0.0006
Natural emittance	61 nm-rad	63 nm-rad
Beam lifetime	65,000 mA.min	104,000 mA.min

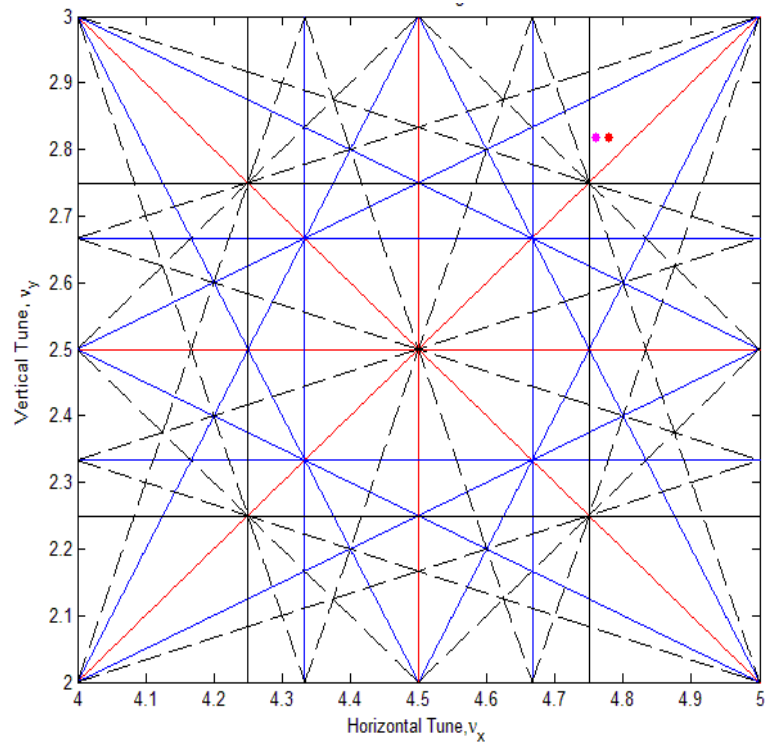


**Figure 5.2** Tune diagram showing the resonance lines up including the 4<sup>th</sup> order.

A lattice with higher beam lifetime has been measured in the SPS storage ring. The simulated emittance is increased to 63 nm-rad instead of the nominal 61 nm-rad. Figure 5.3 shows the comparison of the beam optics between two beam optics. The new beam optics has been applied to the machine. The simulated emittance that is calculated by MAD-X agrees very well with TRACY-II code. The strength of quadrupole magnets are presented in Table 5.2. The betatron functions of new operating point in the middle long straight section,  $\beta_x, \beta_y$  are 14.53 and 2.98 m. The dispersion of new operating point grows up 1 % compared to old operating point ( $\nu_x = 4.678, \nu_y = 2.813$ ).

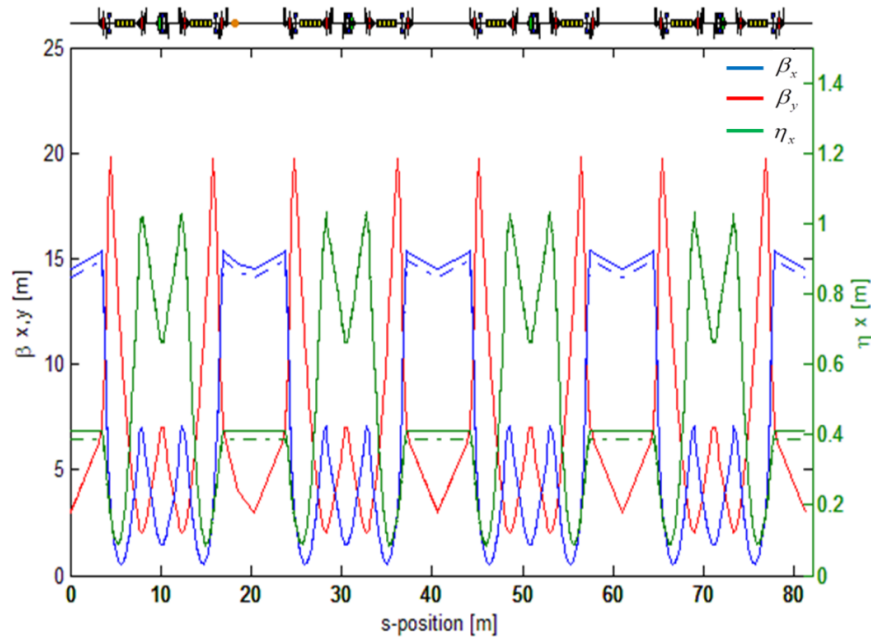


**Figure 5.3** The simulated optic functions comparison between the nominal (dashed lines) and the new optics (continuous lines).

**Table 5.2** The quadrupole magnets parameters of SPS storage ring without IDs.

Magnet/working point	Strength quadrupole magnet [m <sup>-2</sup> ]			
	QF1	QD2	QF3	QD4
Present operating point	2.4744	-2.6299	2.3175	-1.6821
New operating point	2.4834	-2.6348	2.3175	-1.6821

The SPS storage ring has the two sextupole families for adjusting the chromaticity. The optimizing the dynamic aperture for off-momentum,  $\Delta p/p \neq 0$  particles has shown to be successful at chromaticities +2 for simulation. A significant enlargement of the dynamic aperture of the storage ring in ideal machine has been achieved, as illustrated in Figure 5.4 and compared between the different two

operating points. The dynamic aperture of new optics is approximately 70 and 45 mm in horizontal and vertical planes, respectively. Although all sextupoles contribute to the chromaticity correction in the beam optics, the two sextupole families in the SPS storage ring are still primarily used to enlarge the dynamic aperture, relating to chromaticity correction. Now, the SPS storage ring cannot operate with a simulated vertical chromaticity of +2 because of the limitation of sextupole magnets current.

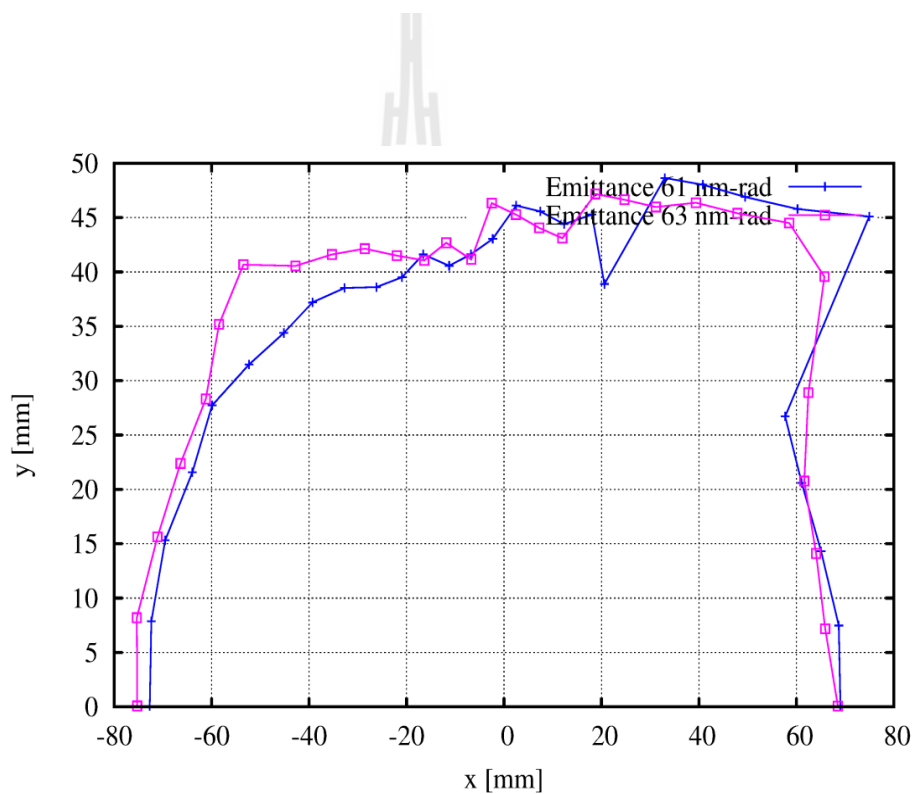


**Figure 5.4** Dynamic aperture of two beam optics at 1.2 GeV. Chromaticity +2,  $\Delta p/p = 0\%$ .

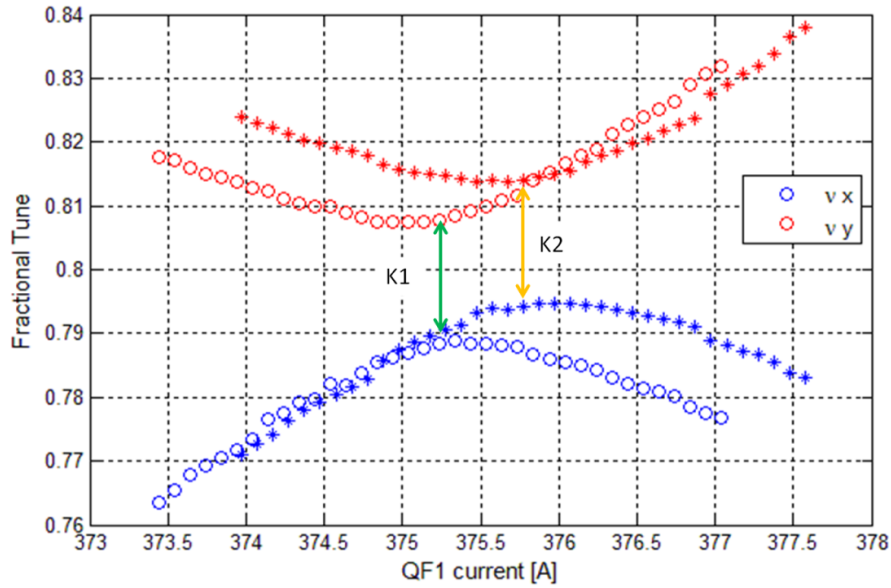


**Figure 5.5** Coupling measurements of present operating point (circle) and new operating point (star) without insertion devices.

In this study, the coupling parameters of the two operating points have been measured; these are summarized in Table 5.1. The measured coupling is shown in Figure 5.5. The theory of linear betatron coupling shows that the emittance ratio  $C$  of the vertical to horizontal emittance is given by

$$C = \frac{K^2}{K^2 + 2(v_x - v_y - l)^2}, \quad K = v_{y\min} - v_{x\max} \quad (5.2)$$

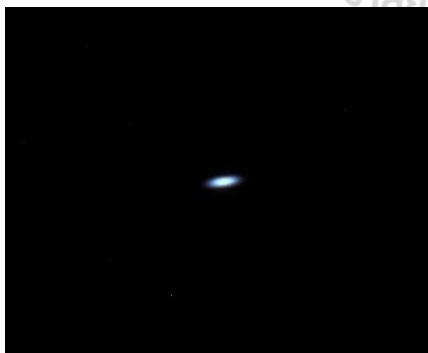
Where the coupling strength  $K$  is measured by the closest approach of the betatron tunes to the coupling resonance,  $v_x, v_y$  is the betatron tune in the SPS storage ring at the operating point. From the measured emittance ratio of different two beam optics are listed in Table 5.3. The emittance coupling grew up 57% for new operating point. The vertical beam size also rises up to 0.04 mm compared to the old operating point. In the SPS storage ring, the vertical beam size is determined by the coupling ratio of



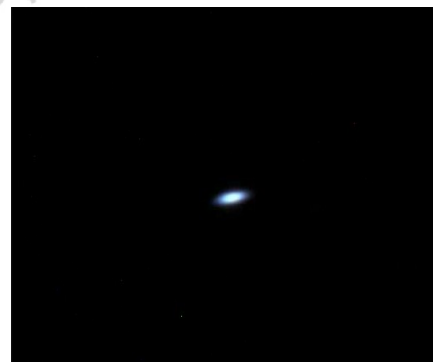
beam oscillations and vertical betatron function. The betatron coupling can be reduced by adjusting the strengths of some skew quadrupoles properly placed in the lattice. The beam size is calculated by Gaussian fitting (Sudmuang *et al.*, 2012). The measured vertical beam size is persistently larger than expected because of the coupling resonance of the working tune point. However, the experiment has proven that this method is good for increasing beam lifetime.

**Table 5.3** The emittance ratio and beam size of SPS storage ring without IDs.

Simulated Emittance	$\nu_x$	$\nu_y$	Measured emittance ratio	Beam size $\sigma_x, \sigma_y$ mm
61 nm-rad	4.760	2.817	4.940 %	0.5927, 0.1883
63 nm-rad	4.780	2.818	11.770 %	0.5935, 0.2282



(a)



(b)

**Figure 5.6** Comparison between beam images of (a) present and (b) new working point at a beam energy of 1.2 GeV.

## 5.2 The effects of insertion devices and commissioning results

Due to an influence of the insertion devices (IDs) installation into the SPS storage ring caused by the vertical focusing of IDs. The new operating point is 4.790 and 2.818 with beam lifetime of 104,000 mA.min without IDs. After installing SWLS, the beam lifetime has decreased by 30-40% to 70,000 mA.min. The electron beam can store for beamline user about 11 hours. The new operating point resulting to beam lifetime is important parameter because the present RF cavity in SPS storage ring, which is used to compensate energy loss. The distortion and compensation of SWLS and MPW on beam dynamics are separately studied at peak magnetic field of 6.5 Tesla (308 A SWLS current), 2.18 Tesla (23.5 mm MPW gap), and two insertion devices together (4.0 Tesla SWLS + 2.18 Tesla MPW and 4.6 Tesla SWLS + 2.18 Tesla MPW). The SWLS is installed in the middle long straight section, which has small horizontal dispersion function  $\sim 0.41$  m in order to have minimal effects on linear optic perturbations. The SWLS has the highest magnetic field of 6.5 Tesla. It also has the strongest effects on the beam dynamics parameters. In the following we study the effects of high field of 6.5 Tesla with the length of 0.323 m (see Chapter I).

For insertion devices installation, the beam dynamic effects have to be carefully considered in a low energy storage ring. The SWLS is placed in the medium long straight sections of SPS lattice. The effects of IDs on transverse tune have also been summarized in section of tune shift. The MPW operates at peak magnetic field  $B_0 = 2.2$  Tesla. It is also installed in low horizontal dispersion but shifted to 1.168 m from the center long strength section. The distorted beta functions in the presence of two IDs are calculated with MAD-X code and depicted in next section. There are two major effects due to the perturbation of the electron beam dynamics by IDs in a

storage ring. The first is the shift of the tune due to the magnetic field of the IDs, which results in beta beating and a smaller dynamic aperture (Chunjarean, 2011). The second is the change in emittance and energy spread of the electron beam due to the energy radiated from the IDs. Effects of the focusing of the IDs may therefore be studied from the focusing strength of the magnet devices in the vertical plane due to the electron beam motion through the oscillating magnetic field. This property gives rise to the change in the betatron tune, the tune shift, of the circulating electron beam in the SPS storage ring. Here the tune shift of the IDs field in the storage ring is estimated using a perturbation method. Simulations were done using MAD-X with the chromaticities at +2 and with no misalignments or field errors in the magnetic field elements. The measured effects the IDs in the SPS storage ring are evaluated analytically and compared it with the simulation results. However, the synchrotron radiation emitted from the SWLS and MPW will increase to hard X-ray region for beamline user. This study was investigated for commissioning IDs in machine consisting of betatron distortion, tune shift, energy loss, beam size change, emittance reduction, and dynamic aperture by adjusting the quadrupole magnets. The lattice distortion, betatron tune shift, beta-beating, and dynamic aperture reduction are investigated and compensated. It is required to correct both tunes and betatron function for smooth operation.

There are three processes to commission after installing two IDs in the SPS storage ring with new operating point resulting higher beam lifetime for user service.

1. Inject electron beam from the booster synchrotron: the commissioning will be started at 1.0 GeV with SWLS. The MPW and undulator gaps are opened fully. The beam current was 50 mA and can be increased approximately to 100mA. The

magnetic field of SWLS is excited from 0-308 A. During driving magnetic field of SWLS, the tune, beta-beating and electron orbit together are corrected. The injection with two insertion devices (SWLS + MPW) has been tried to commission. But the electron beam cannot inject and fill with MPW. Moreover, the electron beam with 2.18 Tesla MPW at 1.0 GeV can store but cannot fill the electron into the storage ring because of the bump voltage, which are not enough to kick the beam from the booster synchrotron to the storage ring. And it also generates some noise to disturb the RF cavity at high voltage resulting to the beam dump.

2. Ramping up the beam energy to 1.2 GeV storage ring: After successfully installing SWLS with target magnetic field (4.0 Tesla and 4.6 Tesla), the electron beam energy is ramped up from 1.0 to 1.2 GeV with a step of 0.2 GeV. The effect and correction of SWLS on the beam dynamics need to be studied as the function of SWLS current/field together with the beam energy. The beam energy relates to the bending magnet current

3. Store an electron beam for user service: at 1.2 GeV beam energy with target current SWLS. The MPW gap is closed from 180 - 23.5 mm. The electron orbit is started to correct at the gap of 80 mm by adjusting the steering magnet adjacent to MPW. The global quadrupole magnets are used to tune the betatron tune far away from the resonances lines.

### 5.2.1 Effects of the insertion devices on the electron beam dynamics

#### Betatron tune shift

The high field insertion devices generated beam optic distortions have been corrected well using MAD-X code. Since a vertical focusing occurs in the device magnets. If the vertical betatron function at a location of the IDs is large, then the tune shift also is large. The tune shifts can be calculated by a linear perturbation method as follows

$$\Delta \nu_y \approx \frac{\beta_y L_{\text{wiggler}}}{8\pi\rho^2}, \quad \Delta \nu_x \approx 0 \quad (5.3)$$

Where  $\beta_y$  is the average value of the betatron function at the position of insertion device,  $L_{\text{wiggler}}$  is the length of the insertion device, and  $\nu_y$  is the vertical betatron tune.

The SWLS currents are driven from 0 to the maximum current of 308A (6.5 Tesla). The MPW and undulator are still opened fully. The tune shift at 1.0 GeV in Figure 5.8 can be therefore compensated to nominal betatron tune. The initial tunes were 4.790 and 2.818 horizontally and vertically, respectively. The betatron tunes will be pulled to the original tunes. As a result of matching, the lattice is changed and thus the global machine working point (tune) is shifted. This can be corrected by a global correction of the main quadrupoles in the storage ring. A global tune correction was then applied by adjusting the global quadrupole families of QF1 and QD2. After injecting electron beam into storage ring with SWLS at an electron beam energy 1.0 GeV.

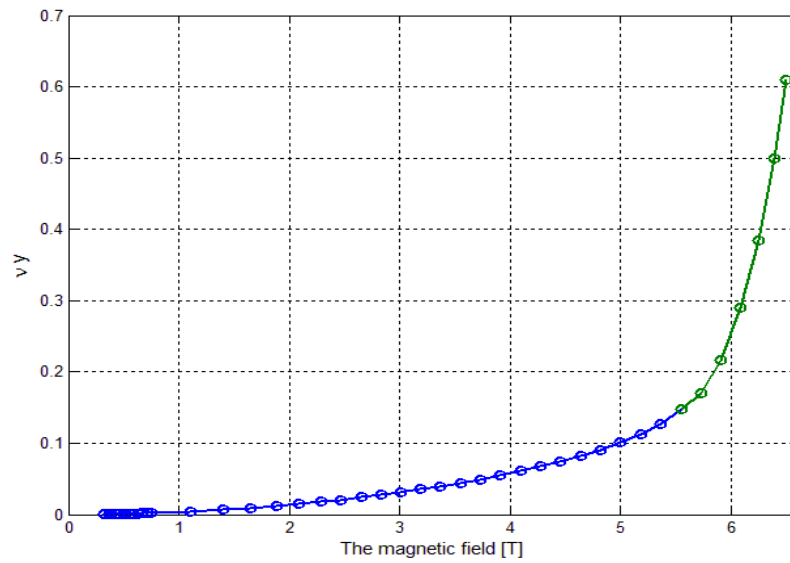


**Figure 5.8** The tune shift at an electron beam energy of 1.0 GeV (injection) with corrected chromaticity = +2 in both planes varies to magnetic field of SWLS.

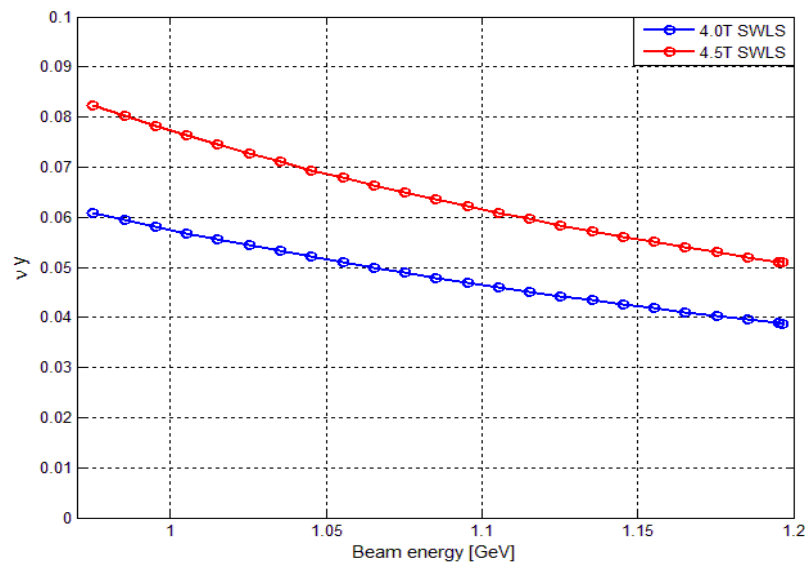


**Figure 5.9** The tune shift with 4.0 Tesla SWLS (red line) and 4.6 Tesla SWLS (blue line) with corrected chromaticity = +2 in vertical plane, varies to an electron beam energy.

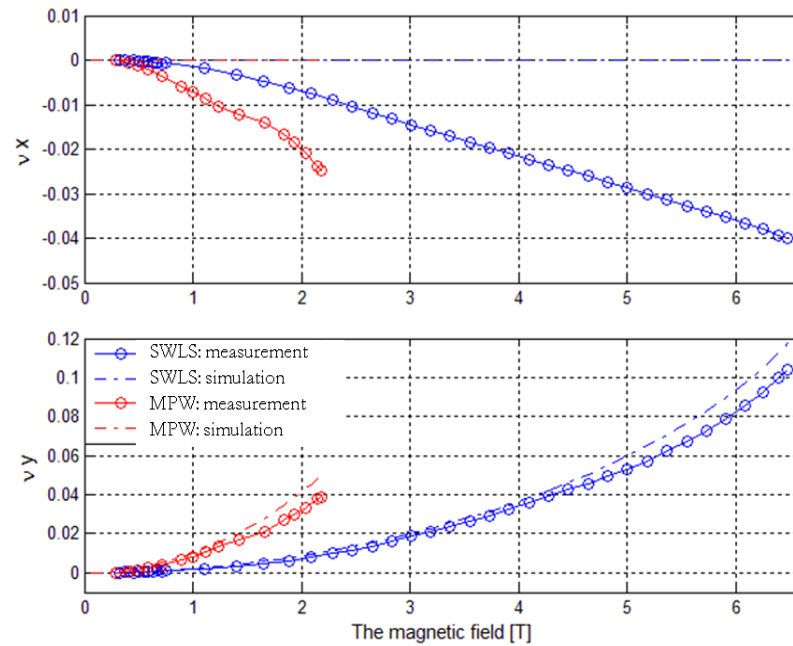


**Figure 5.10** The vertical tune shift as a function of magnetic field at 1.2 GeV.

Before correction, Figure 5.8 shows the tune shift in blue line the electron beam can store. In the green line was found that there are no stable solution exists at the high magnetic field (larger than 5.5 T SWLS). At the maximum peak field, the tune is approximately jumped up to 0.6 vertically due to the vertical focusing field while the horizontal tune is not change. At the low beam energy of 1.0 GeV, the effects on beam dynamics are stronger because of the energy relate to the curvature radius of hard edge model as shown in Figure 5.9. This problem is rather serious for a low energy ring because the energy of the electron beam is small while the magnetic field strength of the ID is strong. After ramping energy with SWLS to 1.2 GeV, The MPW can be scanned from the MPW open position (gap of 200 mm) down to a minimum gap of 23.5 mm. The MPW gap was closed from 190 mm to 23.5 mm in a step of 10 mm. At each setting, the tune and electron orbits were recorded. For a gap of 23.5 mm, the measured magnetic field corresponding to this gap is  $B_0 = 2.18$  Tesla.

The tune shift at 1.2 GeV was measured as a function of magnetic field of each insertion devices. The betatron tune shifts were changed from the nominal tunes for the SPS lattice are  $\nu_x = 4.790$  and  $\nu_y = 2.818$  for both IDs as detailed in Figure 5.10. The measured tune shift is shown together with the predictions of the lattice calculation using MAD-X code. This figure shows the good agreement between the simulated and measured vertical data as a function of the magnetic field at 1.2 GeV. The simulated vertical betatron tunes of the SWLS and MPW are changed to 2.921 and 2.861, respectively, which are 0.5% smaller than measurement. The simulated horizontal betatron tune remains unchanged, but the measured results are decreased to 4.728 and 4.741 for SWLS and MPW, respectively. The measured data are larger than the simulation because the simulation is assumed that the magnetic fields of magnets have no field error for both planes. At maximum SWLS excitation, the measured tune shift was 0.1 and 0.04 for vertical and horizontal compared with a predicted.

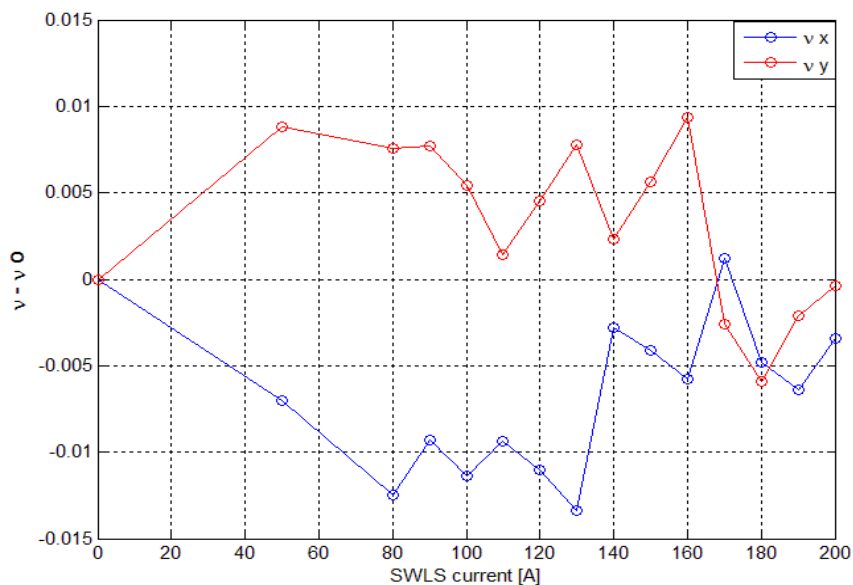


**Figure 5.11** The tune shift after correction at various SWLS currents at 1.0 GeV.



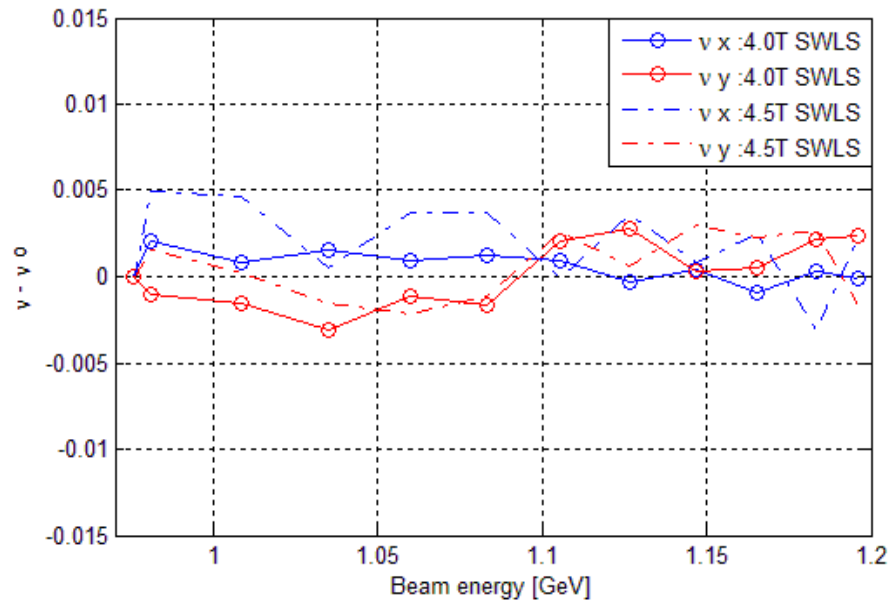


**Figure 5.12** The tune shift after correction compared between simulation and measurement with 4.0 Tesla and 4.6 Tesla SWLS as a function of the energy.

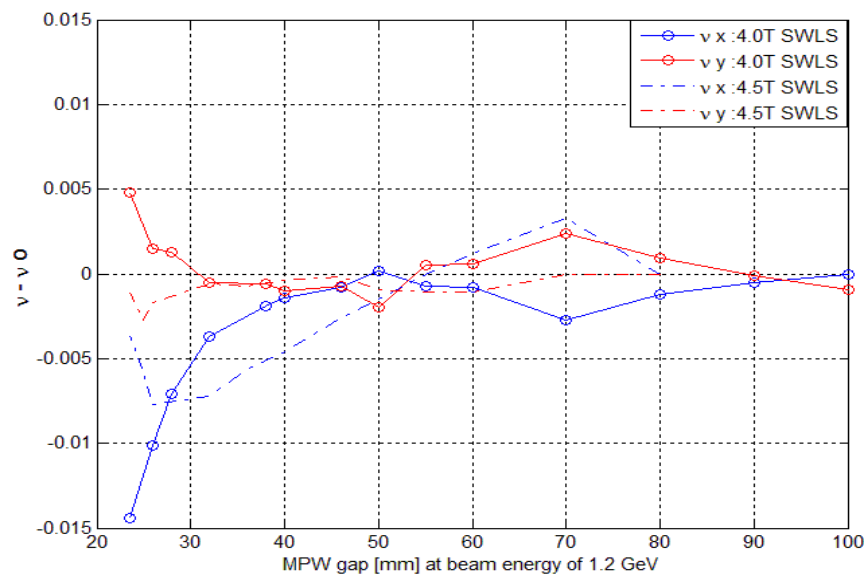


**Figure 5.13** The tune shift after correction at various MPW gap compared between simulation and measurement at 1.2 GeV with 4.0 Tesla SWLS and 4.6 Tesla SWLS.

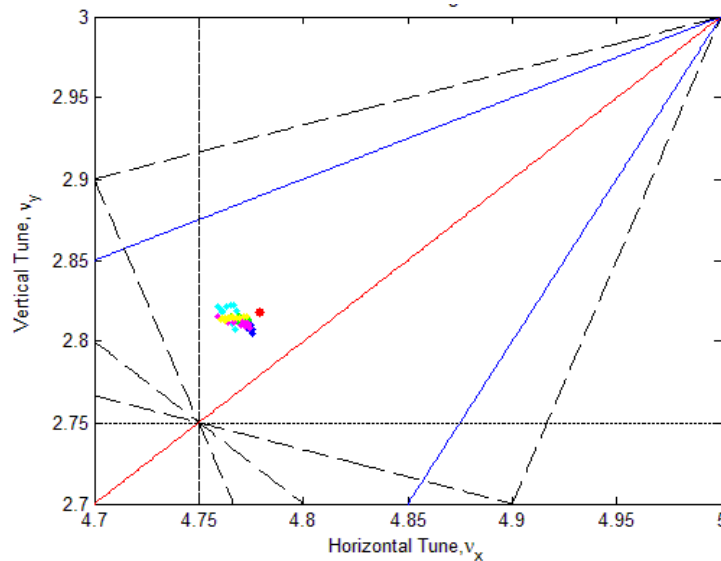


**Figure 5.14** Tune variations after commissioning with five conditions consisting of at 1.0 GeV exciting SWLS current (pink), with 4.0 Tesla SWLS vary beam energy (blue), with 4.6 Tesla SWLS vary beam energy (green), at 1.2 GeV with 4.0 Tesla SWLS vary MPW gap (purple), and at 1.2 GeV with 4.6 Tesla SWLS vary MPW gap (yellow).

After commissioning, the tune shift was removed by a suitable adjustment to the main quadrupoles magnet in the ring. The tune shift is kept away from crossing the serious resonance especially the 3<sup>rd</sup> order one. The simulated tune is corrected and constant at operating point of 4.790 and 2.818. The measured number revolution or tune is constant at a fixed value of 0.05 respects with the original value during commissioning. The measured vertical tune shift is shown in Figure 5.11 as a function of the SWLS current at 1.0 GeV beam energy. The horizontal tune is changed by the vertical tune compensation and magnetic field errors. The measured results are nearly the nominal tune. At injection energy 1.0 GeV, the maximum tune is shifted 0.01 and 0.014 for vertical (red line) and horizontal (blue line), respectively. Figure 5.12 shows

that the change tune is measured during ramping energy process. The betatron tune with 4.0 Tesla and 4.6 Tesla SWLS as a function of beam energy is change less than 0.005 for both planes after commissioning. At a beam energy of 1.2 GeV, the MPW is close to minimum gap of 23.5 mm. It shows that the horizontal tune is changed much more than vertical after correction as plotted in Figure 5.13. The Figure 5.14 shows that the betatron tune is varied during commissioning. This is possibly due to misalignments, not included in the simulations. It caused by the quadrupole effects associated with the insertion devices, which have been shown in Chapter II.

#### **Beta-beating (betatron distortion)**

The betatron distortion can be compensated successfully by local correction. The quadrupole current settings were calculated using MAD-X and applied to the lattice. The vertical focusing due to magnetic field of IDs cause a beating of the betatron functions around the SPS storage ring. Therefore, the beta-beating has to be improved in the injection, ramping and store electron commissioning processes. The simulation and measurements with the local beta correction were done. Figure 5.15 is shown the optics distortions at maximum peak field of two insertion devices. If the 1.2 GeV SPS storage ring includes only the SWLS at middle long strength section, the betatron is high amplitude up to 63 m but it still symmetry as shown in Figure 5.15 (left). After including the 2.18 Tesla MPW, the betatron symmetry is broken (Figure 5.15 right) because the MPW is not located in the middle of long straight section. It is shifted to 1.168 m from the center of long straight section resulting to the vertical betatron asymmetry. In the presence of SWLS and MPW, only changes in vertical beta function are perturbed while horizontal beta function did not change any more.

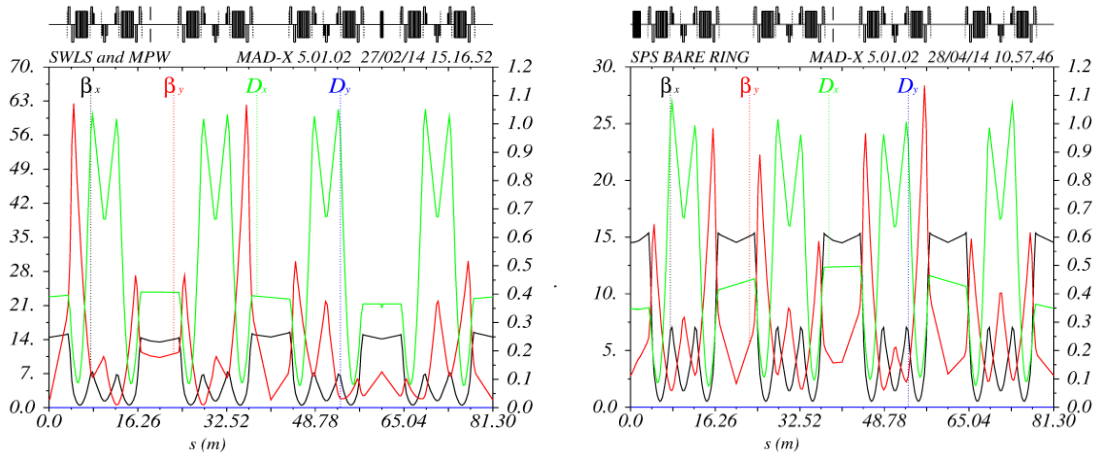
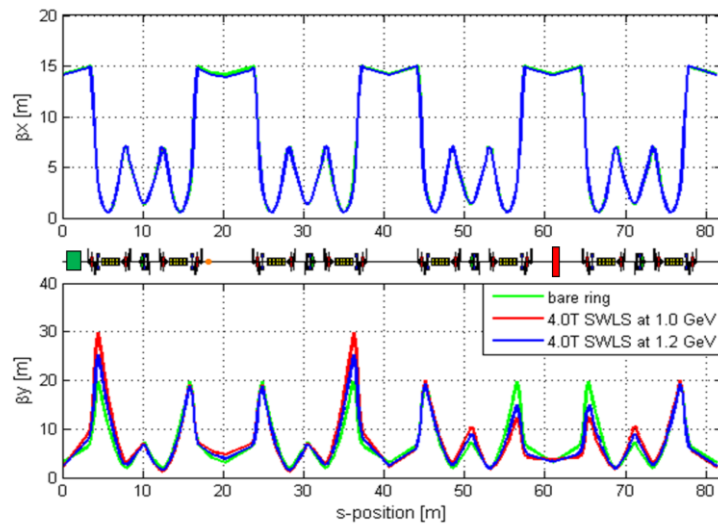


**Figure 5.15** Betatron function effect on the 1.2 GeV SPS machine with 6.5 Tesla SWLS (left) and 2.18 Tesla MPW (right).

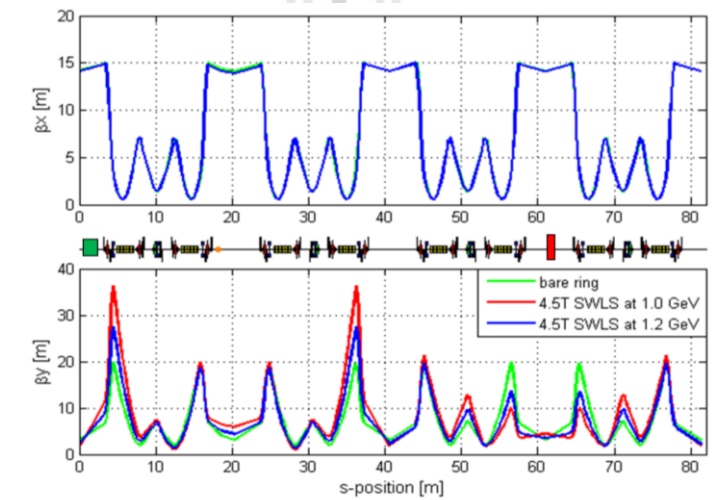
Due to the fact that the two magnetic fields of SWLS (4.0 Tesla and 4.6 Tesla) with 2.18 Tesla MPW are important commissioned response the requirement of the beamline user. Thus, the optic functions are investigated, corrected, and measured. The beating of betatron function due to the insertion device in the storage ring can be simply calculated by following formula (Ropert, 1998)

$$\left(\frac{\Delta\beta_y}{\beta_y}\right)_{\max} \approx \frac{\beta_y L_{\text{wiggler}}}{4\rho^2 \sin(2\pi\nu_y)}, \quad \frac{\Delta\beta_x}{\beta_x} \approx 0 \quad (5.4)$$

Where  $\beta_y$  is the average value of the betatron function at the position of insertion device,  $L_{\text{wiggler}}$  is the length of the insertion device,  $\nu_y$  is the vertical betatron tune, and  $\rho$  is the bending radius.



(a)



(b)

**Figure 5.16** The betatron functions along the SPS storage ring before correction. (a) with 4.0 Tesla SWLS (b) with 4.6 Tesla SWLS at 1.0 and 1.2 GeV. The MPW and SWLS are indicated with red and green boxes a long straight section.

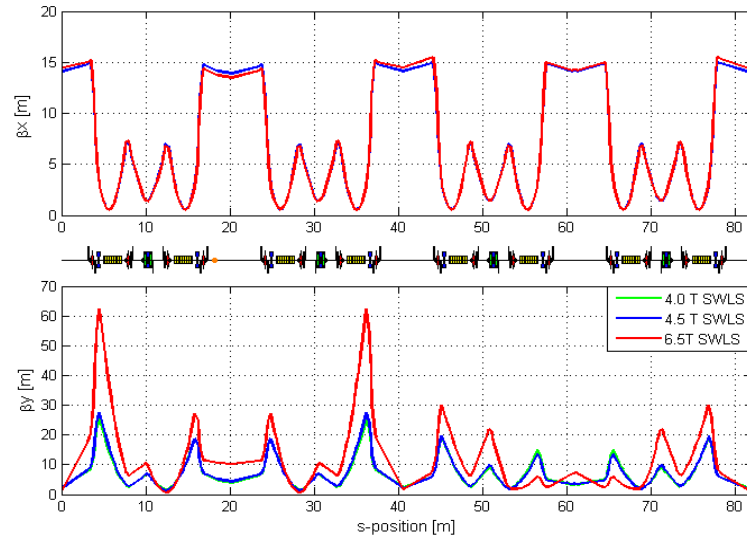


**Figure 5.17** The betatron functions before correction around the SPS storage ring various the magnetic fields of SWLS at 1.2 GeV.

Figure 5.16 shows the effects on beam dynamics by 4.0 Tesla and 4.6 Tesla SWLS are stronger at low energy of 1.0 GeV because of the energy relate to the curvature radius of hard edge model. The vertical betatron distortion depends on the length of insertion devices. The length of device magnet relate to the magnetic field of the device magnet in Equation 5.3. So that at high magnetic field the betatron function will be disturbed by the high amplitude. The optics distortion is stronger at higher magnetic field as present in Figure 5.17 due to the vertical focusing of SWLS. The betatron function of SPS bare ring is designed to be symmetric. Since two IDs were installed, the symmetry lattice were broken resulting the vertical betatron functions amplitude increased up to 63, 30.01 and 27.63 m after including the 6.5 Tesla, 4.6 Tesla and 4.0 Tesla SWLS. The horizontal betatron functions have no effects from the magnetic field of both IDs. However, the two insertion devices (IDs) will be commissioned into SPS storage ring with unperturbed optics parameters for machine

operation. The large betatron distortion also causes the beam lifetime reduction. The betatron function has to be compensated to originally lattice as plotted in Figure 5.18.

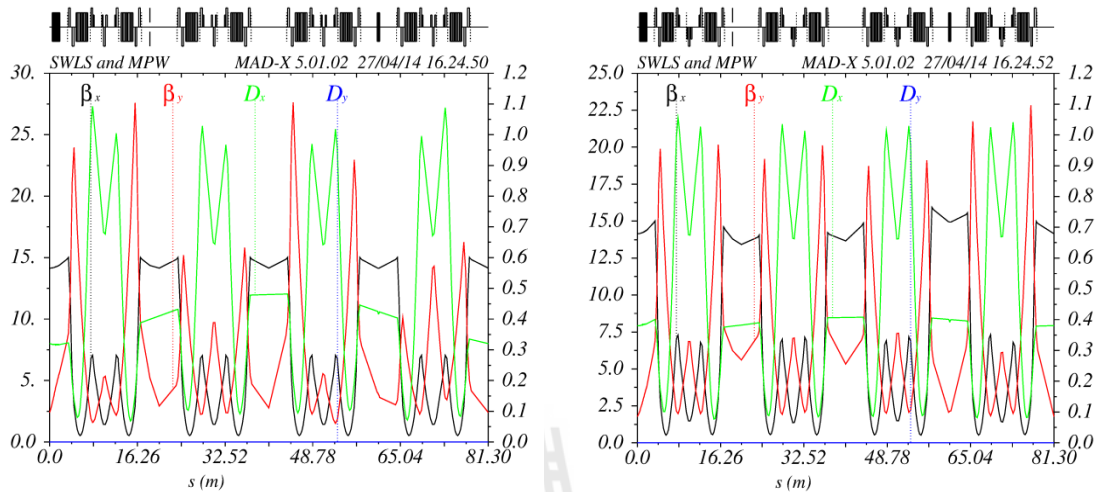


**Figure 5.18** The betatron functions around the SPS storage ring with the 4.0 Tesla magnetic fields of SWLS and 2.18 Tesla MPW at 1.2 GeV (left) before correction and (right) after correction.

The corrected betatron functions around the SPS storage ring after including are displayed in Figure 5.19. The vertical betatron function is beat by 27% and 33% after including 4.0 Tesla and 4.6 Tesla SWLS together with 2.18 Tesla MPW when compared with the designed lattice without insertion device. After correction, the betatron distortions are almost close to the original value displayed in a green line. Corrections for SWLS and MPW have been implemented and a reduction in the beta-beating has been achieved. In order to minimize a change in the betatron function the IDs should be located at the places where low dispersion functions occur. However, the effect of the IDs on the beam optics should be eliminated all together and the optics should be restored to the original one outside the IDs sections.

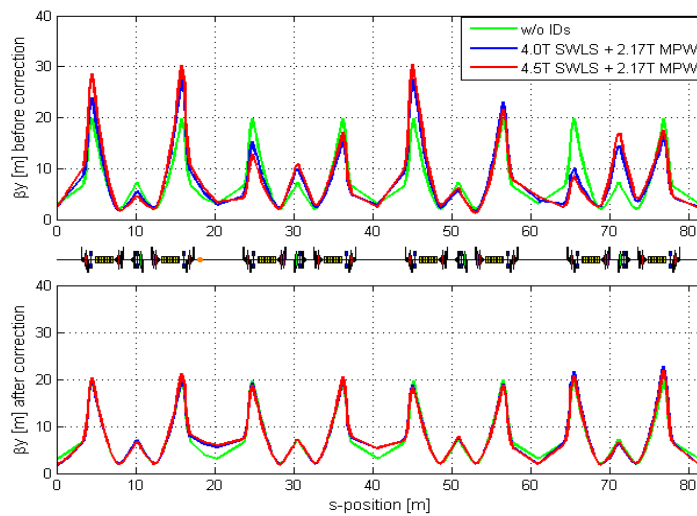


**Figure 5.19** The betatron functions before (top) and after (bottom) correction at various magnetic fields of SWLS with 2.18 Tesla MPW at 1.2 GeV.

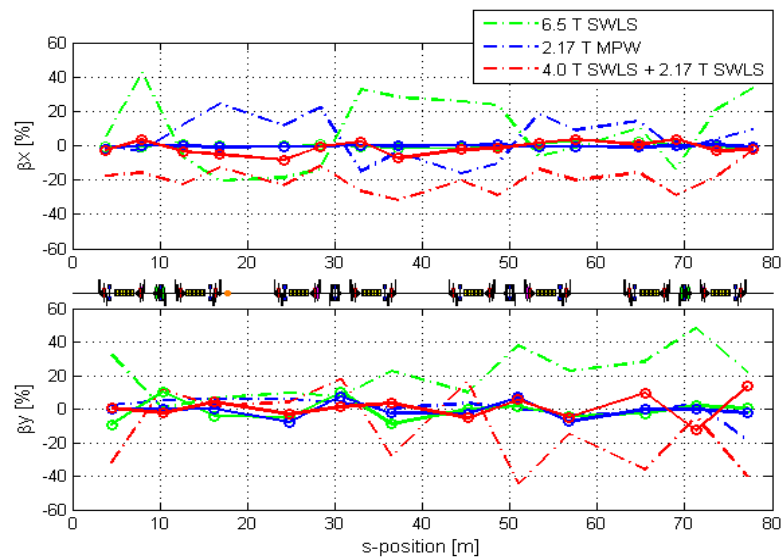


**Figure 5.20** The simulated (circle) and measured (dot line) beta beating along the ring with the insertion devices after commissioning at 1.2 GeV with 2.18 Tesla MPW.



After commissioning, the effects are compensated by local quadrupole magnets. Figure 5.20 presents the measured beta beating in dotted line and it is compared with the simulation results in solid line along the ring. The betatron function measurements were conducted after the correction. The beta-beat was measured at quadrupole magnet location. After commissioning 4.0 Tesla SWLS together with 2.18 Tesla MPW, the measured beta beating values are indicated to be 40% and 20% higher than expected for vertical and horizontal, respectively. At high field of 6.5 Tesla SWLS, the measured betatron functions are changed by 40% and 50% in vertical and horizontal planes. The amounts of measured data are larger than that of the simulation because in the simulation it is assumed that the magnetic fields of magnets have no field error for both planes. The magnetic field errors occur from the magnet misalignment. Here, the magnetic fields in both planes are not perfect. The brightness of the synchrotron radiation may be reduced and large betatron functions may reduce the dynamic aperture.

### **Chromaticity compensation and dynamic aperture reduction**

The chromaticities were compensated at +2 in SPS storage ring while the real chromaticities in the machine are not constant at +2. Because of the limitation of the sextupole magnets in the SPS storage ring, the SPS storage ring cannot store the beam with chromaticity at +2. The MAD-X code is used to tune the sextupole strengths with chromaticity at +2. The region in the phase space where the beam trajectories are stable, it can be reduced with respect to the physical aperture and to the RF acceptance by the nonlinearities of magnetic fields. The dynamic aperture refers to the stable area in which the electron can move with high beam stability. The most of

electron motion are within a physical aperture defined by the vacuum chamber to ensure a good beam lifetime.

In most storage rings the dynamic aperture is determined by the sextupoles used to correct the chromaticity. The sextupole scheme is adjusted by calculations and tracking simulations in order to have a dynamic aperture larger than the physical aperture. The strength comparison of two sextupole families, SF and SD, is summarized in Table 5.4. The oscillation amplitude guarantees stable particle motion over a given number of turns. For the dynamic aperture with off-momentum collisions happen between the beam particles because of energy loss between them. In commissioning processes the sextupole current magnets, SF/SD, are constant at 10.8/10.8 (1.0GeV) and 15.6/17.4 (1.2 GeV) for all cases.

**Table 5.4** Sextupole strength magnets for chromaticities correction.

IDs field	Strength sextupole magnet [m <sup>-3</sup> ]	
	SF	SD
6.5 T SWLS	9.403	-10.427
2.18 T MPW	9.756	-10.863
4.0 T SWLS + 2.18 T MPW	9.782	-11.646
4.6 T SWLS + 2.18 T MPW	9.758	-11.552

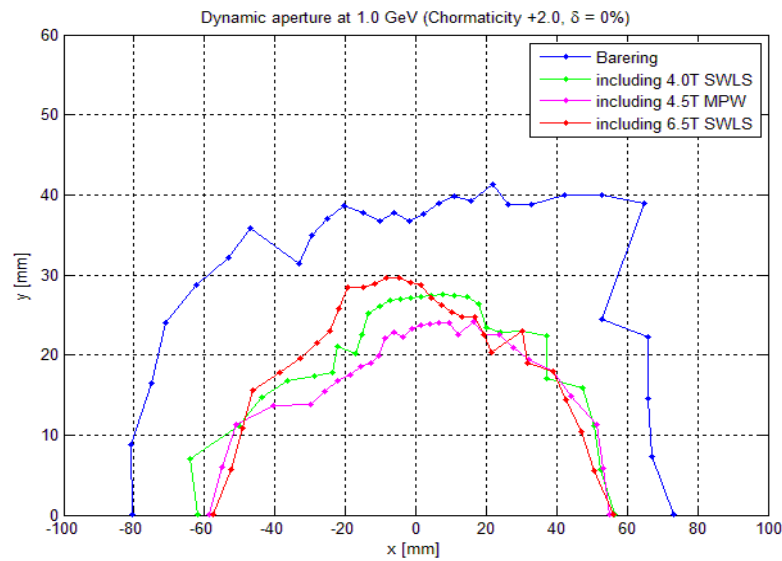


**Figure 5.21** The simulated dynamic apertures of SWLS by using TRACY-II code with chromaticity +2 at 1.0 GeV after correction.

The dynamic apertures are also plotted with the natural chromaticity corrected to +2 in both planes. The calculations were made with the TRACY-II code. In the presence of IDs the dynamic apertures are reduced mainly due to its linear effects. The dynamic aperture of the machine after correction is shown in Figure 5.21. Although the optics perturbation due to the IDs field can be compensated and the operating point can be restored close to the original lattice, the SWLS and MPW still have an effect on the reduction of dynamic aperture. Dynamic aperture improves by 33% and 18% in vertical and horizontal planes, respectively. In both cases of dynamic aperture are smaller than the lattice design in comparison.

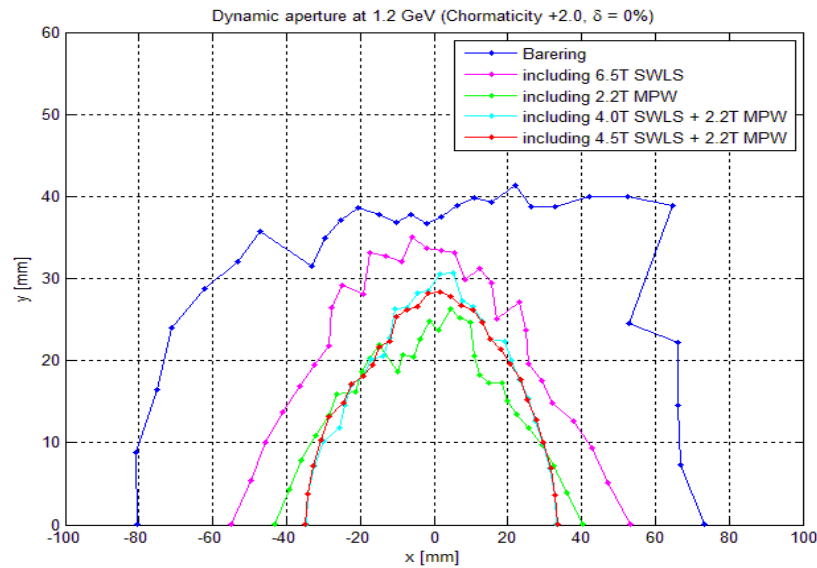


**Figure 5.22** Dynamic apertures after including IDs, chromaticity +2, off-momentum ( $\Delta p/p = 0\%$ ) at beam energy of 1.2 GeV.

The result shown in Figure 5.22, after tracking with TRACY-II code, that the electron beam can survive in the storage ring. The dynamic apertures are decreased because the IDs break the SPS storage ring symmetry and lattice periodicity. The simulation by using TRACY-II code as shown in Figure 5.26 shows that the dynamic apertures are reduced by 12/31% and 37/56% at the maximum field of the SWLS and MPW, respectively. The vertical amplitude of dynamic aperture is in the range of 40 - 25 m after including SWLS together with MPW. It also depends on the value of betatron function around the SPS storage ring as presented in the previous section.

### Electron orbit distortion

From the deviated electron angle at the exit of the IDs we can be written the closed orbit distortion (COD) in the BPM numbered  $j$  as

$$\Delta = \frac{\theta \sqrt{\beta_i \beta_j}}{2 \sin \pi \nu} \cos(|\mu_i - \mu_j| - \nu \pi), \quad (5.5)$$

where  $\theta$  is the kicked electron angle,  $\mu$  is the phase advance, and  $\nu$  is the betatron tune. The indices  $i$  and  $j$  indicate the position at the exit of IDs and BPMs.

In SPS storage ring, 20 BPMs and 28 correctors are implemented for 16 horizontal planes and 12 vertical planes. After including the SWLS and MPW into the SPS storage ring, 4 BPMs and 4 steering magnets are installed to the downstream and upstream of the two IDs. As an electron beam passes through the insertion devices, it will be shifted from the center position by the magnetic field of insertion devices. The misalignments yielding the field errors cause it to jump up. The electron trajectory at the end of the IDs was measured and presented in the chapter III. The electron orbits are not zero at the end of the device magnets. For maximum field of SWLS and MPW, the displacements are 2 mm and 0.1 mm. The angle deviations are 6.5 mrad and 0.15 mrad, respectively. The electron orbit can be compensated by steering magnet adjacent to SWLS and MPW. The effect of vertical magnetic field of SWLS yields the electron orbit distortion along the device magnets. The electron will hit the vacuum chamber resulting to higher pressure, higher energy loss, and shorter beam lifetime in the storage ring. During commissioning MPW at 1.2 GeV, the electron orbit is unstable at the MPW gap of 60 to 50 mm. The electron orbit has to be corrected by adjusting steering magnet to be set quickly.

The real machine contains different types of errors produced by magnet misalignment, magnetic field, and several external sources. The beam distortion and instability of the closed orbit are disturbed by these errors resulting to the dynamic aperture reduction and the optics changes. They will disturb emittance and brightness. Thus, they must be corrected. Closed orbit correction in Equation 5.4 can be achieved by using steering magnets and beam position monitors (BPMs). In order to maintain the high brilliance of the radiation coming from the IDs and to minimize the electron closed orbit changes, the closed orbit must be corrected at the position of the IDs.

Insertion of the IDs will introduce both changes in electron trajectory. The results were already shown in the chapter III. The orbit distortions are compensated by the corrector magnets or steering magnets. They are used to kick angles required for the correction magnets to compensate the electron orbit. The corrector magnets are used in the real machine as plotted in Figure 5.23 and Figure 5.24. As the MPW gap was reduced from 60 mm to 20mm, the vertical and horizontal tune changed, resulting correction in the electron orbits. The electron beam orbit distortions are less than 0.5 mm in both planes for beam operation. The steering magnets in use are summarized in Table 5.5.

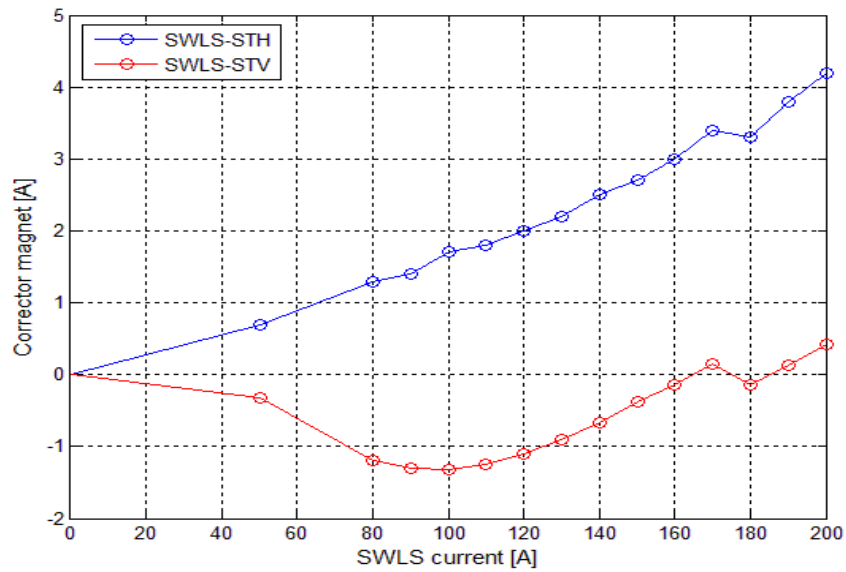


**Figure 5.23** The steering magnet current adjacent to SWLS vs. the magnetic field of SWLS in the real machine for orbit correction at 1.0 GeV.

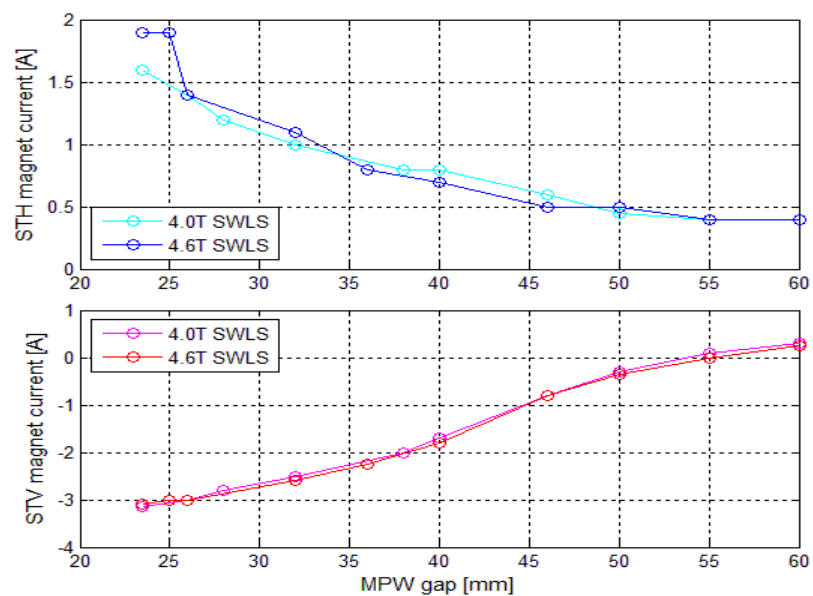


**Figure 5.24** The steering magnet current adjacent to MPW vs. the MPW gap in the real machine for orbit correction at 1.2 GeV.

**Table 5.5** The steering magnet current adjacent to SWLS and MPW at 1.2 GeV.

IDs operation	Steering magnet of IDs [A]			
	STH-SWLS	STV-SWLS	STH-MPW	STV-MPW
Bare ring w/o Ids	0	0	0	0
4.0 T SWLS + 2.18 T MPW	3.4	0.15	1.6	-3.15
4.6 T SWLS + 2.18 T MPW	4.2	0.43	1.9	-3.10

### Quadrupole magnet currents

Due to the compensation of beam dynamics effects of the insertion devices (IDs) on the SPS storage ring, the quadrupole magnets around the ring are used to correct the effects consisting of local and global corrections. In SPS storage, there are included the two families of focusing (QF1, QF3) and two families of defocusing quadrupole magnets (QD2, QD4). The QF1 and QD2 restore the global tune back to the lattice design. Betatron function compensation around the ring is called the local correction. The SWLS is placed in the middle long straight section. The two families of QF1 and QD2 adjacent to SWLS correct the betatron distortion. The MPW is not located in the middle long strength section. Thus, the correction of betatron distortion is matched by the six individual quadrupole magnets close to MPW. The values of the quadrupole magnets values are expected to be set in the machine by using MAD-X code. The detail of matching was presented in the Chapter 4. The quadrupole strength of magnets before including IDs consisting of QF1, QD2, QF3, and QD4 are 2.48342, -2.63478, 2.3176, and -1.6823, respectively. This algorithm was applied to generate quadrupole settings to operate ring with both IDs.



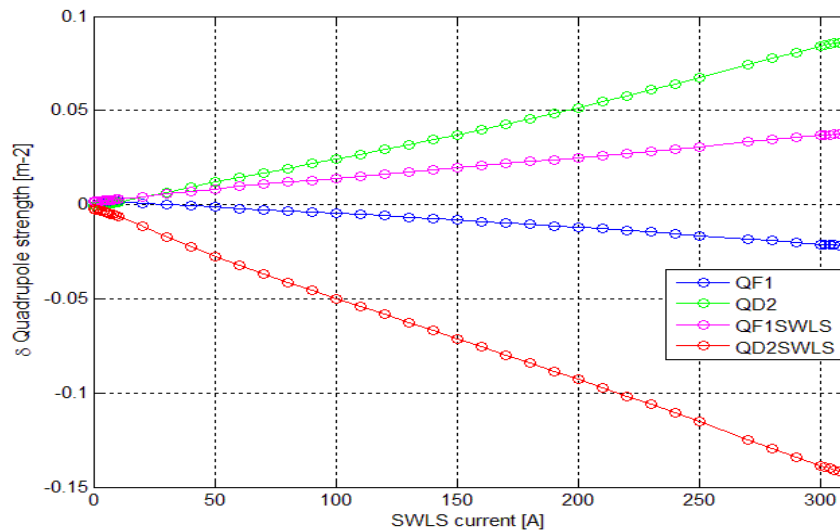


**Figure 5.25** The focusing strengths of quadrupole magnets at 1.0 GeV beam energy with different magnetic fields of SWLS.

The commissioning process started at low energy (1.0 GeV) with SWLS. The simulated strengths of quadrupole magnets are shown in Figure 5.25, which are used to compensate the optics parameters. Due to the vertical magnetic field of SWLS the defocusing quadrupole magnets of QD2 and QD2SWLS are changed to the values larger than those of the focusing quadrupole magnets of QF1 and QF1SWLS for tune and beta-beating correction. The needed strength of quadrupole magnets of 6.5 Tesla SWLS change to compensate for the tune shift of 0.6 was 20% at 1.0 GeV. Because the beam dynamics effects are stronger at low beam energy, at operation energy of 1.2 GeV the strength of quadrupole magnets are shifted to the values smaller than injection energy of 1.0 GeV in Figure 5.26.

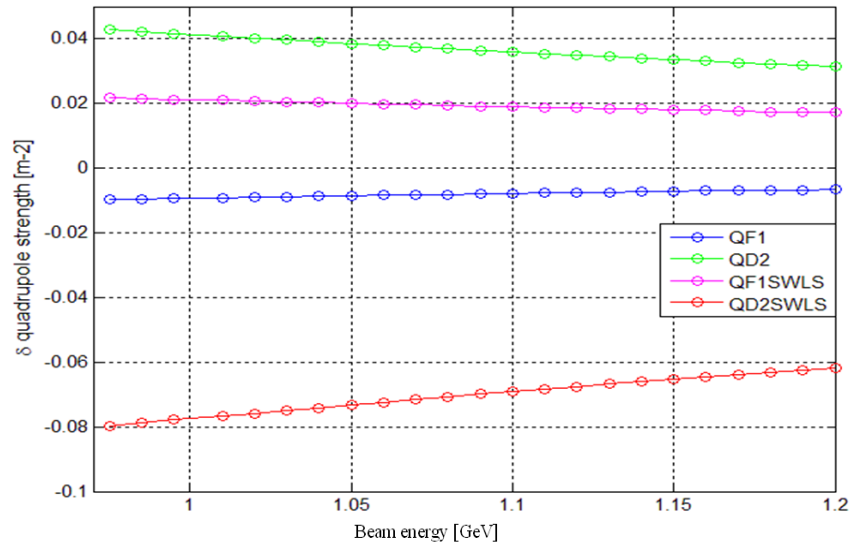


**Figure 5.26** The strengths of quadrupole magnets with 4.6 T SWLS vary to the beam energy.

After ramping up the beam energy with SWLS, the gap of MPW is closed from 180 to 23.5 mm as presented in Figure 5.27. The six individual quadrupole magnets are used for local/betatron correction. The maximum change of strengths of the quadrupole magnet is that of QF3MPWD, which is located in MPW downstream. It decreases  $0.1 \text{ m}^{-2}$  or 15.45 if converted to current. The QD2 strength magnet for tune correction is reduced by  $0.06 \text{ m}^{-2}$  or 9 A different from the bare ring. The simulated and used currents in real machine are compared in Figure 5.28. The simulated quadrupole current values are approximately used to correct beam optics during commissioning. After commissioning IDs with the machine, all magnets current are fitted as function as summarized in Table 5.6, 5.7, 5.8, and 5.9 for three processes.

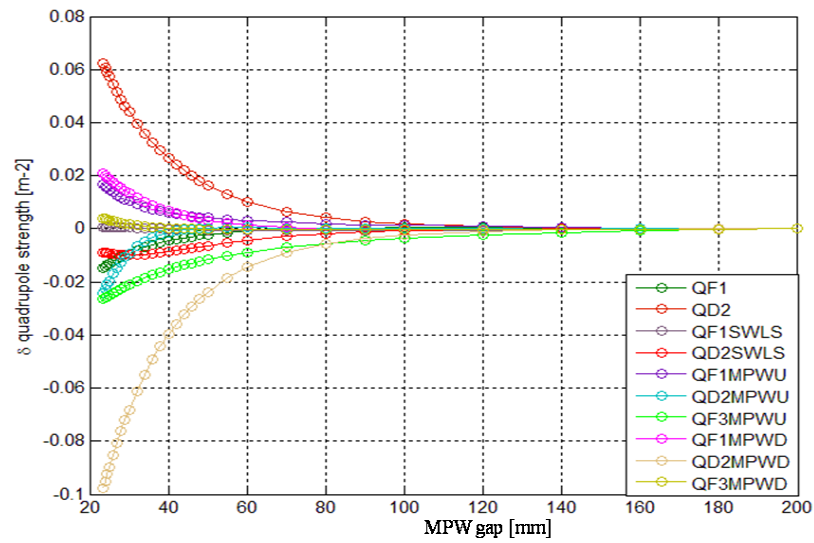


**Figure 5.27** The quadrupole strength magnets as a function of MPW gap with 4.6 T SWLS at beam energy of 1.2 GeV.

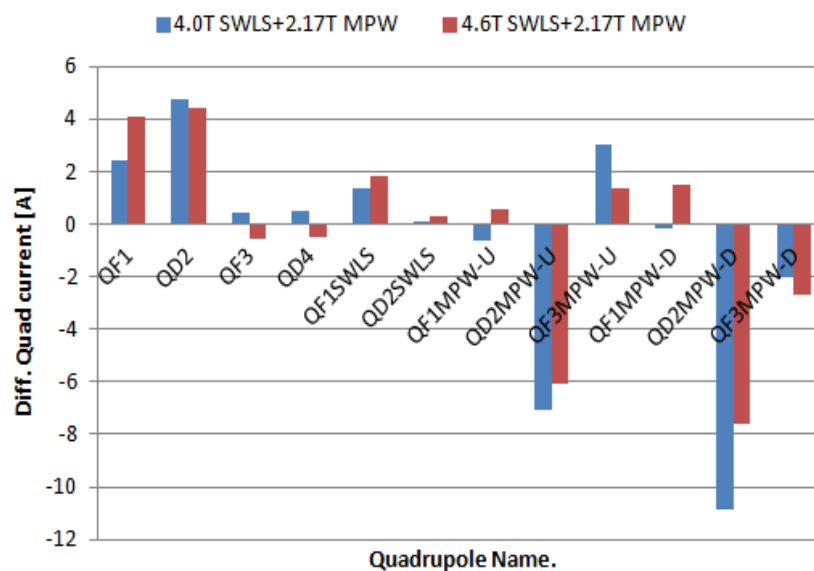


**Figure 5.28** The compared quadrupole magnet currents in storage ring between simulation (blue) and setting (red) in the machine with 4.0 Tesla SWLS+ 2.18 Tesla MPW and 4.6 Tesla SWLS+ 2.18 Tesla MPW at 1.2 GeV beam energy.

**Table 5.6** Magnet current are used in the real machine for beam operation in Ampere at 1.0 GeV beam injection.

Magnets	4.0 Tesla SWLS	4.6 T SWLS
QF1	305.5021	305.7021
QD2	321.4595	321.4595
QF3	287.2157	287.2157
QD4	205.8391	205.8391
QF1SWLS	307.7409	307.9409
QD2SWLS	333.5128	333.5128
STV_SWLS	3.4	0.15
STH_SWLS	4.2	0.425

**Table 5.7** The quadrupole current magnets as a function of beam energy (E), and MPW gap with 4.0 Tesla SWLS and 4.6 Tesla SWLS.

Magnets	Polynomial functions
<i>The beam energy (E) is ramped up to 1.2GeV with 170A SWLS</i>	
QF1	$I(E) = 954.302E^3 - 3,148.6562E^2 + 3,765.4952E - 1,257.298$
QD2	$I(E) = 1,184.772E^3 - 3,884.2472E^2 + 4,568.2302E - 1,538.329$
QF3	$I(E) = 958.6432E^3 - 3,131.9652E^2 + 3,718.153E - 1,249.304$
QD4	$I(E) = 507.967E^3 - 1,624.918E^2 + 1,952.792E - 624.339$
QF1SWLS	$I(E) = 966.442E^3 - 3,188.182E^2 + 3,810.583E - 1,272.698$
QD2SWLS	$I(E) = 1,229.180E^3 - 4,029.841E^2 + 4,739.468E - 1,595.9928$
<i>The beam energy (E) is ramped up to 1.2GeV with 200A SWLS</i>	
QF1	$I(E) = 980.406E^3 - 3,243.724E^2 + 3,879.394E - 1,302.151$
QD2	$I(E) = 998.002E^3 - 3,278.299E^2 + 3,915.278E - 1,304.740$
QF3	$I(E) = 1,035.448E^3 - 3,387.292E^2 + 4,000.600E - 1,353.272$
QD4	$I(E) = 559.868E^3 - 1,797.455E^2 + 2,143.656E - 694.595$
QF1SWLS	$I(E) = 987.602E^3 - 3,267.533E^2 + 3,907.874E - 1,311.710$
QD2SWLS	$I(E) = 1,035.433E^3 - 3,401.254E^2 + 4,062.119E - 1,353.674$

**Table 5.8** Magnet current are used in the real machine at a beam energy 1.2 GeV with 170A SWLS.

Magnets	Polynomial functions
QF1	$I(G) = 2.410E-05G^3 - 4.936E-03G^2 + 3.314E-01G + 3.674E+02$
QD2	$I(G) = 8.588E-05G^3 - 1.699E-02G^2 + 1.137E+00G + 3.700E+02$
QF3	$I(G) = -4.803E-06G^3 + 8.388E-05G^2 + 2.093E-04G + 3.585E+02$
QD4	$I(G) = -4.808E-06G^3 + 8.443E-05G^2 + 1.892E-04G + 2.568E+02$
QF1SWLS	$I(G) = -1.723E-05G^3 + 2.773E-03G^2 - 1.570E-01G + 3.808E+02$
QD2SWLS	$I(G) = -5.224E-05G^3 + 8.875E-03G^2 - 4.793E-01G + 4.187E+02$
QF1MPW-U	$I(G) = -2.528E-05G^3 + 4.664E-03G^2 - 2.951E-01G + 3.813E+02$
QD2MPW-U	$I(G) = -8.002E-05G^3 + 1.575E-02G^2 - 9.287E-01G + 4.119E+02$
QF3MPW-U	$I(G) = -9.431E-06G^3 - 6.586E-04G^2 + 1.306E-01G + 3.544E+02$
QF1MPW-D	$I(G) = -1.443E-05G^3 + 4.852E-03G^2 - 4.039E-01G + 3.847E+02$
QD2MPW-D	$I(G) = -6.159E-05G^3 + 1.786E-02G^2 - 1.403E+00G + 4.292E+02$
QF3MPW-D	$I(G) = -9.700E-07G^3 + 5.207E-04G^2 - 1.853E-02G + 3.568E+02$
STV_MPW	$I(G) = -1.613E-05G^3 + 2.905E-03G^2 - 1.855E-01G + 4.530E+00$
STH_MPW	$I(G) = -1.186E-04G^3 + 1.490E-02G^2 - 4.916E-01G + 1.784E+00$

**Table 5.9** Magnet current are used in the real machine at a beam energy 1.2 GeV with 200A SWLS.

Magnets	Polynomial functions
QF1	$I(G,80-30mm) = 8.104E-06x^4 - 1.465E-03x^3 + 9.561E-02x^2 - 2.608E+00x + 3.986E+02$ $I(G,30-23.5mm) = 1.473E-03x^2 - 4.659E-01x + 3.845E+02$
QD2	$I(G) = 1.923E-05x^3 - 9.695E-03x^2 + 9.324E-01x + 3.704E+02$
QF3	constant at 357.586 A
QD4	constant at 255.886 A
QF1SWLS	$I(G) = 1.712E-08x^6 - 4.530E-06x^5 + 4.934E-04x^4 - 2.832E-02x^3 + 9.052E-01x^2 - 1.534E+01x + 4.863E+02$
QD2SWLS	$I(G) = -5.531E-05x^3 + 9.824E-03x^2 - 5.677E-01x + 4.211E+02$
QF1MPW-U	$I(G) = -6.800E-05x^3 + 1.136E-02x^2 - 6.352E-01x + 3.873E+02$
QD2MPW-U	$I(G) = -1.314E-05x^4 + 2.194E-03x^3 - 1.254E-01x^2 + 2.716E+00x + 3.797E+02$
QF3MPW-U	$I(G) = -1.263E-05x^3 + 6.282E-04x^2 + 7.912E-02x + 3.533E+02$
QF1MPW-D	$I(G) = 6.024E-07x^4 - 8.891E-05x^3 + 5.083E-03x^2 - 1.295E-01x + 3.572E+02$
QD2MPW-D	$I(G) = 7.742E-05x^3 - 3.373E-04x^2 - 7.371E-01x + 4.252E+02$
QF3MPW-D	$I(G) = -2.985E-05x^3 + 7.171E-03x^2 - 5.497E-01x + 3.886E+02$
STV_MPW	$I(G) = -4.589E-05x^3 + 7.357E-03x^2 - 4.008E-01x + 7.860E+00$
STH_MPW	$I(G) = -1.438E-04x^3 + 1.818E-02x^2 - 6.284E-01x + 3.551E+00$

## 5.2.2 Effects of radiation from insertion devices

### Emittance change

The effect of the IDs is the change in emittance due to emission radiation obtained from MAD-X simulations. The natural emittance depends on the quantum excitation and radiation damping. The emittance is proportional to the ratio  $I_5/I_2$  in Chapter 2. The  $I_5$  and  $I_2$  terms are synchrotron radiation integrals. We have already seen that the IDs insertion in a machine increases  $I_2$  and, therefore, increase the energy radiated per turn. The emittance depends on the value of  $I_5$  which is determined by the dispersion and optical functions in the IDs sections. Emittance can be tuned by varying the dispersion in the IDs. At a operating point (4.768, 2.813) the dispersion function is 5% higher than that of the new operating point (4.790, 2.818). So the emittance increases much more than new operating point because of the quantum excitation term. The emittance of a storage ring with IDs can be expressed as

$$\varepsilon_0 \approx \frac{8}{15\pi} C_q \gamma^2 \frac{\langle \beta_x \rangle}{\rho_w^3 k_w^2} \quad (5.6)$$

Where  $C_q$  is the quantum constant,  $3.84 \times 10^{-13}$  m,  $\beta_x$  is the horizontal betatron function,  $\rho_w$  and  $k_w$  are the radius and focusing strength of insertion device, respectively.

Equation 5.5 also illustrates how IDs installed in dispersive sections can increase the emittance in the insertion devices. The installation of such devices can be considered once all dispersion free long straights have been occupied with IDs.



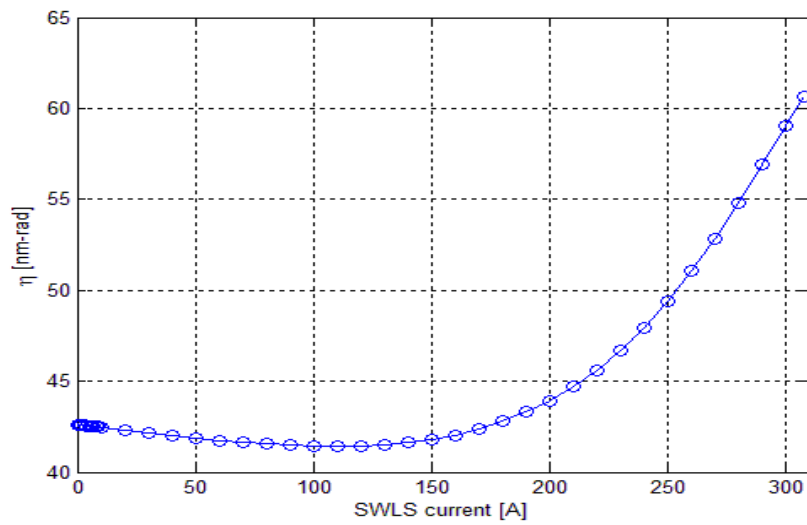


**Figure 5.29** The beam emittance as a function of SWLS current for 1.0 GeV ring.

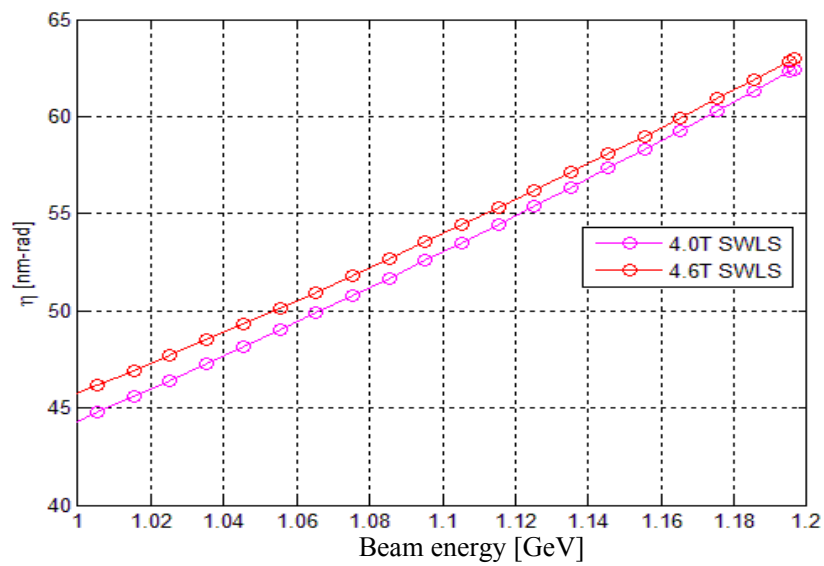


**Figure 5.30** The beam emittance with 4.0 Tesla SWLS (pink line) and 4.6 Tesla SWLS (red line) as a function of beam energy.

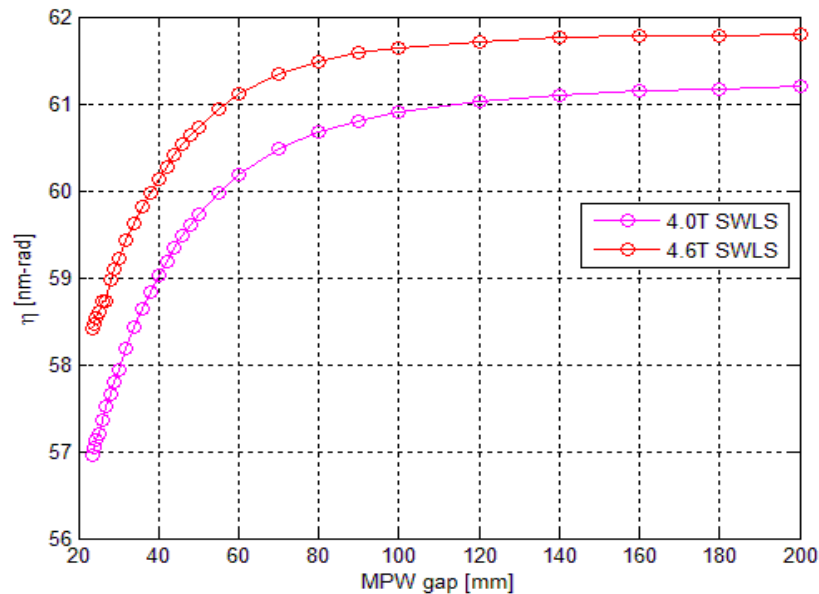


**Figure 5.31** The variation of beam emittance with MPW gap in 1.2 GeV storage ring with SWLS field are 4.0 Tesla and 4.6 Tesla.

Figure 5.29 shows that the natural emittance of the perturbed lattice with the 6.5 Tesla SWLS is increased from 41.4 to 60.5 nm-rad at a beam energy of 1.0 GeV. It also introduces an emittance blowup of about 46% compared to the bare lattice. The emittance is increased because SWLS is placed in a high dispersion section through the radiation excitation. The IDs magnets should be placed where the dispersion function is zero. In other words, the IDs magnets should be placed where the equilibrium orbit is independent of the particle energy. It can be reduced by increasing the damping without increasing the quantum radiation. The emittance is also increased by ramping up beam energy as shown in Figure 5.30. The production of a photon creates a sudden energy loss and then a sudden change of the particle equilibrium trajectory which lead to an increase of the particle amplitude. Since the radiation is quantized, the statistical fluctuations in the energy radiated per turn cause

a growth of the oscillation amplitudes. At 1.2 GeV the beam operation with 2.18 Tesla MPW (23.5 mm MPW gap) is reduced about 5 nm-rad compared to the starting point with MPW off in Figure 5.31. The emittance is inversely proportional to the damping rate. The damping rate is proportional to the energy radiated in one turn. The equilibrium distribution of the particles results from the combined effect of quantum excitation and radiation damping. Moreover, the beam emittance is also changed by the insertion of device magnets, which is the vertical field integral increased depending on the third magnetic field integral term.

### Energy loss

Energy loss is an important property of electron beam. Insertion devices increase the energy loss of electron particle from synchrotron radiation. The total energy loss per turn in the storage ring is given by

$$U_0 = \frac{C_\gamma}{2\pi} E^4 \left( \frac{1}{(B\rho)^2} \frac{B_w^2 L_w}{2} \right) \quad (5.7)$$

Where  $C_\gamma$  is  $8.846 \times 10^{-5} \text{ m/GeV}^3$ ,  $\beta_x$  is the horizontal betatron function,  $L_w$  and  $B_w$  are total length and magnetic field of insertion device, and  $B$  and  $\rho$  are magnetic field and radius of bending magnet.

The energy is lost by the total length and the magnetic field of insertion devices as described by Equation 5.6. The energy loss with SWLS and MPW at full field increases by 24.6% to 82.85 keV/turn as listed in Table 5.10. The beam energy loss in SPS storage ring can be compensated by RF voltage of 125 kV.

**Table 5.10** The energy loss in the SPS storage ring after installing insertion devices in keV/turn.

SWLS field	E = 1.0 GeV	E = 1.2 GeV
		with 2.18 Tesla MPW
w/o SWLS	28.82	70.01
w/ 4.0 Tesla SWLS	31.75	74.56
w/ 4.6 Tesla SWLS	32.60	75.82
w/ 6.5 Tesla SWLS	36.26	82.85

### 5.3 The stored electron for user service

After setting bending, quadrupole and sextupole magnets power supply according to 1.0 GeV injection, we tried to inject the electron beam into storage ring with SWLS. The method is found to be more suitable for operation which is implemented for SPS storage ring with good injection efficiency and lifetime. The magnet current values were put into the auto file. It was set in PLC program with the polynomial functions as listed in Table 5.6, 5.7, and 5.8. It will automatically adjust the all magnet current for operation. This appeared to work well until smaller gaps were reached to the minimum of 23.5 mm with SWLS at 1.2 GeV. The period time for preparing the beam is approximate 30 minutes. The quadrupole current magnets used for machine operation are summarized in Table 5.11 and 5.12. The used quadrupole magnets can correct the perturbation effects by two IDs almost perfectly. The electron can be stored for user service to generate the synchrotron radiation in a range of hard X-ray.

**Table 5.11** Magnet current used in the real machine for beam operation with SWLS in Ampere.

QM magnets	4.0 Tesla SWLS		4.6 Tesla SWLS	
	1.0 GeV	1.2 GeV	1.0 GeV	1.2 GeV
QF1	305.5021	374.8680	305.7021	374.9612
QD2	321.4595	396.0005	321.4595	395.9190
QF3	287.2157	357.5878	287.2157	357.5855
QD4	205.8391	255.8879	205.8391	255.8863
QF1SWLS	307.7409	377.6152	307.9409	377.7072
QD2SWLS	333.5128	410.8488	333.5128	410.7642
QF1MPW-U	305.4774	374.8377	305.4774	374.9309
QD2MPW-U	321.4595	396.0005	321.4595	395.9190
QF3MPW-U	287.2157	357.5878	287.2157	357.5855
QF1MPW-D	305.5021	374.8680	305.7021	374.9612
QD2MPW-D	321.4595	396.0005	321.4595	395.9190
QF3MPW-D	287.2157	357.5878	287.2157	357.5855

**Table 5.12** Magnet current are used in the real machine at a beam energy 1.2 GeV with two IDs.

Magnets	Storage ring magnet current [A]	
	4.0 T SWLS + 2.18 T MPW	4.6 T SWLS + 2.18 T MPW
QF1	372.9208	374.3573
QD2	388.6532	387.4023
QF3	358.5578	357.5855
QD4	256.8580	255.8858
QF1SWLS	378.4475	378.9947
QD2SWLS	411.7099	412.4174
QF1MPW-U	376.6102	377.7942
QD2MPW-U	397.6346	398.6254
QF3MPW-U	357.0259	355.3371
QF1MPW-D	377.6593	379.3021
QD2MPW-D	404.9825	408.3481
QF3MPW-D	356.6635	355.9647

### Machine operation

Currently the SPS has been commissioned completely. It has five operation modes consisting of 1) bare ring, 2) 6.5 Tesla SWLS, 3) 2.18 Tesla MPW, 4) 4.0 Tesla SWLS + 2.18 Tesla MPW, and 5) 4.0 Tesla SWLS + 2.18 Tesla MPW. Modes 1 – 3 had been started with bare ring emittance of 61 nmrads and modes 4 - 5 were began with bare ring emittance of 63 nmrads for increasing beam lifetime. This research is focused on modes 4 and 5 only. These modes serve the beamline

requirement. The beam current is decayed from 150 to 50 mA with two IDs at 1.2 GeV after 11 hours of operation. The operation process was maintained by PLC program, which controlled all main magnet supplies, RF and steering supplies. The electron beam is operated at working point as places on tune diagram (Figure 5.32). The betatron tune of bare ring is  $\nu_x = 4.790$  and  $\nu_y = 2.818$  in red point. The horizontal tunes are changed to 0.021 and 0.015 from nominal point for 4.0 Tesla SWLS and 4.6 Tesla SWLS with 2.18 Tesla MPW while the vertical point can be corrected almost close the original value. The beam is stable at these points because it is far away from resonance lines.

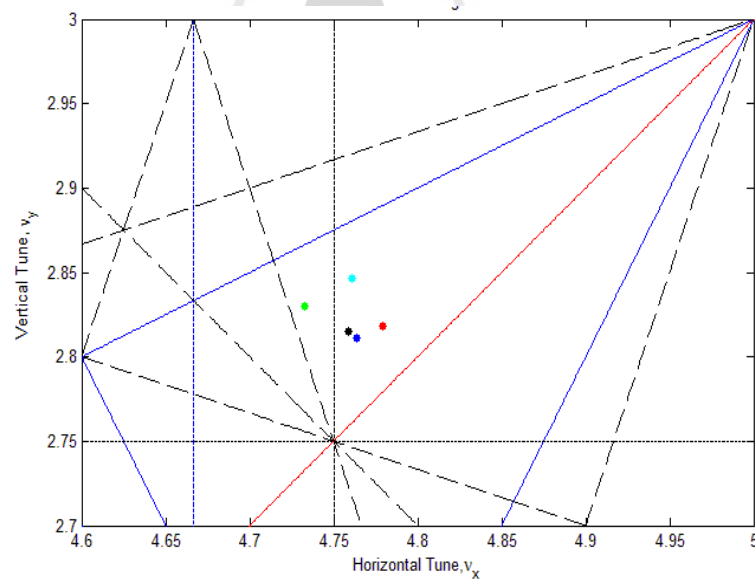


**Figure 5.32** Tune diagram with 4<sup>th</sup> resonance line, The machine operation without IDs (red), with 6.5 Tesla SWLS (light blue), with 2.18 Tesla MPW (green), with 4.0 Tesla SWLS + 2.18 Tesla MPW (black), and 4.6 Tesla SWLS + 2.18 Tesla MPW (blue).

### Beam size

The beam size is 0.5935 mm along the horizontal axis and 0.2282 mm along the vertical axis without insertion devices. The beam emittance will blow up vertically in Table 5.13. Due to the effect of radiation emission from device magnets, the emittance will rise up resulting blow up in the beam size. The Gaussian fitting is used to estimate the size of synchrotron beam.

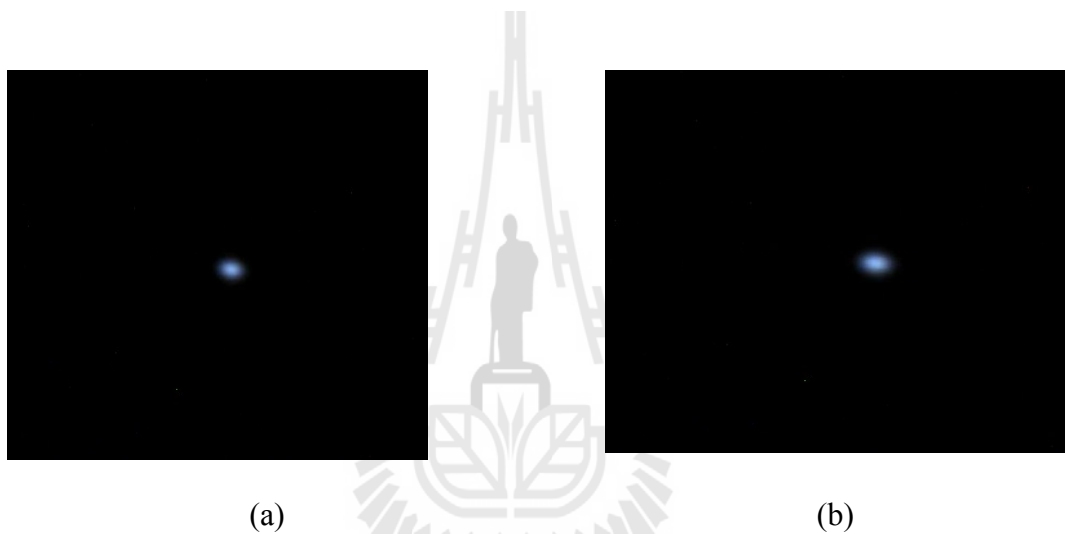


**Figure 5.33** Beam images for (a) with 4.0 Tesla SWLS + 2.18 Tesla MPW (b) with 4.6 Tesla SWLS + 2.18 Tesla MPW.

**Table 5.13** The beam size at different the magnetic field of IDs.

IDs	Horizontal beam size	Vertical beam size
4.0 T SWLS + 2.18 T MPW	0.4831 mm	0.3046 mm
4.6 T SWLS + 2.18 T MPW	0.4838 mm	0.3436 mm



### **Beam lifetime**

In order to serve beamline user requirement, the beam current has to be higher than 50 mA after 11 hours (Table 5.14). Beam lifetime is determined by the time interval in which the beam intensity is reduced to a fraction of its initial value. In this case the beam lifetime is reduced due to the effect of emitted radiation inside the insertion devices. The particle loss produced by their betatron or synchrotron oscillation amplitude exceeds the dynamic aperture limitation. The beam lifetime consists of the Touschek and quantum lifetimes. The Touschek scattering process happens inside the electron beam itself. It can be increased by increasing RF voltage in storage ring. Since a beam lifetime depends on the 3<sup>rd</sup> power of machine energy. This will cause beam energy increase from 1.0 to 1.2 GeV. The quantum lifetime depends on the pressure in vacuum chamber. After the beam operation for user service about 5 months the pressure in the SPS storage ring is better resulting to a higher beam lifetime. At operating point ( $v_x = 4.768$ ,  $v_y = 2.813$ ) the beam current is reduced to be lower than 50 mA after applying 6.5 Tesla SWLS and 2.18 Tesla MPW. Therefore, the beam intensity resulting to a number of photon/second is also lower. The experiment time is longer. The sample may be damaged by synchrotron radiation beam.

**Table 5.14** The beam lifetime in SPS storage ring different conditions.

Operation mode	Beam lifetime [mA.min] at $I_b=100\text{mA}$	Beam current [mA] after 11 hours
<i>Operating point at 4.768, 2.813, emittance of 61 nmrad</i>		
Bare ring	77655	150-58
2.18 T MPW	72370	150-54
6.5 T SWLS	34595	150-18
<i>Operating point at 4.790, 2.818, emittance of 63 nmrad</i>		
Bare ring	101554	150-73
4.0 T SWLS + 2.18 T MPW	74685	150-56
4.6 T SWLS + 2.18 T MPW	62317	150-46

#### Close orbit distortion

The distorted closed orbit can be corrected to the residual distortion of -0.5 m vertically and 0.4 mm horizontally in the ID straight section with 4.6 Tesla SWLS + 2.18 Tesla MPW while the root mean square orbit is of 0.98 mm vertically and 1.60 mm horizontally. The COD orbit changes are shown in Figure 5.35. It is in a range lower than 10  $\mu\text{m}$  and 30  $\mu\text{m}$  for horizontal and vertical axes compared to the reference orbit except at the position of insertion devices (SWLS and MPW). By operating the two devices at the same time the overall closed orbit error increases to 0.5 mm with 4.6 Tesla SWLS and the MPW at minimum gap. The closed orbit distortion changes are rather large which, to a large extent, is an effect of the bad correction at IDs sections after increasing the magnetic field of the IDs. However, the

variation of COD can be controlled well within  $10\ \mu\text{m}$  by the slow orbit feedback (Supat *et al.*, 2012).

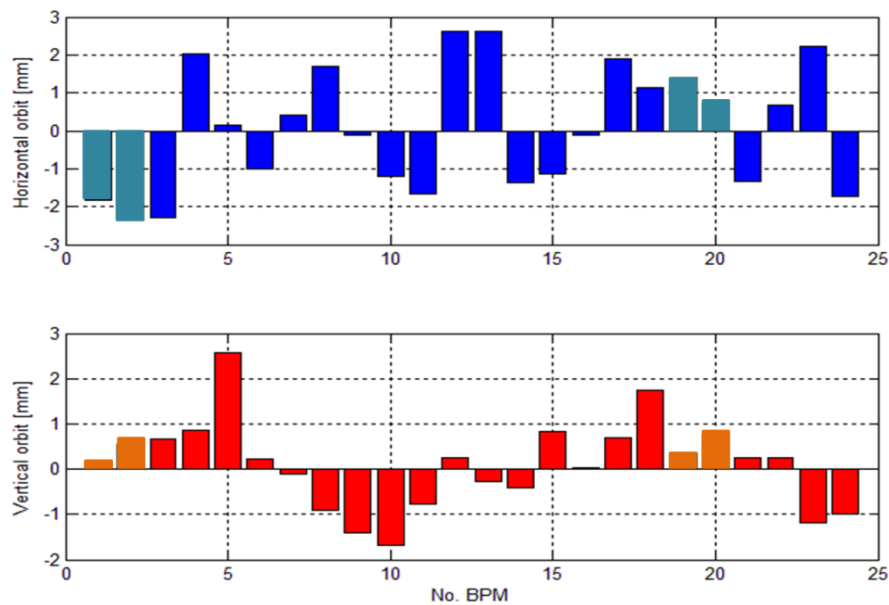


**Figure 5.34** The reference electron orbit in the SPS storage ring.

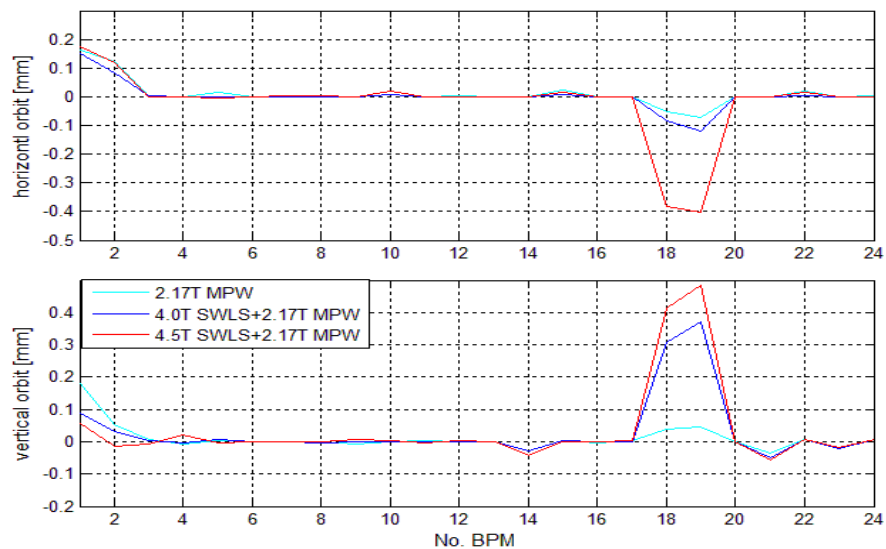


**Figure 5.35** The close electron orbit (COD) after applying the magnetic field of insertion devices (IDs) which are corrected by all steering magnets.

### User service

Figure 5.36 shows the beam current and beam lifetime for 4.0 Tesla SWLS + 2.18 Tesla MPW operation mode. This mode can generate the synchrotron radiations that have the photon energy of 12.7 keV (with  $10^9$  phs/s) and 8 keV (with  $10^{10}$  phs/s) from 4.0 Tesla SWLS and 2.18 Tesla MPW, respectively to beamline measurements. Then the electron beam can be stored with beam current of 60 mA after operating for 11 hours.

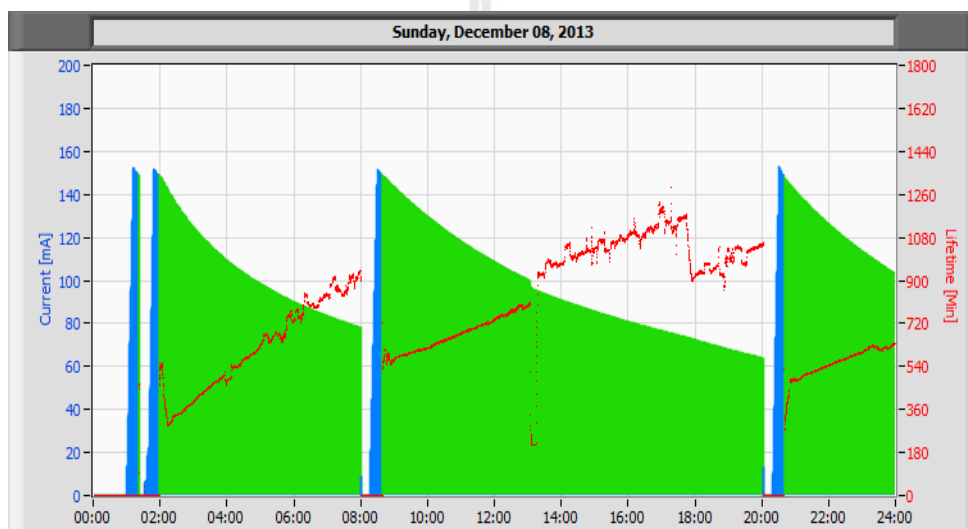


**Figure 5.36** Beam operation windows.

### 5.4 The future work

1. Apply the measured field errors to simulation.
2. Expect and calibrate the quadrupole magnets current into the real machine using LOCO (Safranek *et al.*, 2002) after installing insertion devices.
3. After installing the second RF cavity, which has higher voltage, the emittance will be decreased and the beam lifetime will be higher for high beam brightness.

## CHAPTER VII

### CONCLUSIONS

The commissioning and operation results of the high field insertion devices (superconducting wavelength shifter and hybrid multipole wiggler) for the Siam Photon Source (SPS) storage ring are concluded in this thesis. Three main achievements include:

1. Optimization and improvement of the SPS optics of the bare ring after installing the MPW and SWLS.

The operating point observation using the Frequency Map Analysis (FMA), the operating point was observed for long beam lifetime. The beam lifetime as a function of the horizontal and vertical betatron tunes,  $\nu_x$  and  $\nu_y$  was measured and plotted on the resonance diagram. We selected the new point which is located at  $\nu_x = 4.790$  and  $\nu_y = 2.818$ . The beam lifetime increased 30% to 104,000 mA.min compared with old operating point ( $\nu_x = 4.768$  and  $\nu_y = 2.813$ ). The simulated emittance increased to 63 nm-rad instead of the nominal 61 nm-rad. At the new operating point, the measured emittance coupling grew up 57% and the vertical beam size also rises 0.04 mm compared to the old operating point.

2. Calculation and compensation of the beam dynamics effects introduced by high-field insertion devices in the SPS storage ring.

There are two major effects due to the perturbation of the electron beam dynamics by insertion devices (IDs) in a storage ring.

2.1 The first is the effect from IDs may change beam dynamics parameters such as betatron distortion and tune shifts that cause to reduce dynamics aperture due to the magnetic field of the IDs.

- At the maximum peak field of 6.5 Tesla SWLS, the calculated tune is approximately jumped up to 0.6 vertically due to the vertical focusing field at beam energy of 1.0 GeV. The vertical tune shift is decreased to 0.1 after the beam energy is ramped up to 1.2 GeV while the horizontal tune is not change. The simulated vertical betatron tunes of the SWLS and MPW are changed to 2.921 and 2.861, respectively, which are 0.5% smaller than measurement. The measured horizontal data are larger than the simulation because the simulation is assumed the magnetic fields of magnets have no field error for both plane. The betatron tune is corrected and constant at operating point of 4.790 and 2.818 by simulation. After commissioning in the machine, the maximum tune is shifted 0.01 and 0.015 for vertical and horizontal, respectively. The vertical and horizontal tunes were corrected by two families of global quadrupoles magnet, QF1 and QD2.

- The vertical betatron function is disturbed by 27% and 33% after including 4.0 Tesla and 4.6 Tesla SWLS together with 2.18 Tesla MPW, compared with designed lattice without insertion device. The effects were compensated by local quadrupole magnets which are placed adjacent to two IDs. The simulated betatron distortions are almost closely the original value for both planes. After commissioning 4.0 Tesla SWLS together with 2.18 Tesla MPW, the measured beta beating values

indicated to be 40% and 20% higher than expected for vertical and horizontal, respectively. For high field of 6.5 Tesla SWLS, the measured betatron functions were changed by 50% and 40% in vertical and horizontal planes.

- The simulated dynamic aperture reduces in vertical plane by 33% and in horizontal plane by 18% compared to the lattice design at beam energy of 1.2 GeV. The effect of multiple field errors in case of disturbed machine was also the dynamic aperture reduction.

2.2 The second is the change in emittance and energy loss of the electron beam due to the energy radiated from the IDs.

- The energy loss with SWLS and MPW at full field increased by 24.6% to 82.85 keV/turn. Because the energy loss is raised up so the storage ring needs the increasing RF voltage.

- The simulated emittance was changed from 63 to 57 and 58.5 after including 4.0 Tesla SWLS and 4.6 Tesla SWLS with 2.18 Tesla MPW at 1.2 GeV, respectively due to the damping and the quantum radiation.

- The beam size without insertion devices was 0.5935 and 0.2282 mm in horizontal and vertical axis. After installing and commissioning 4.0 Tesla SWLS and 4.6 Tesla SWLS with 2.18 Tesla MPW into the storage ring, the beam size was increased from 0.3042 to 0.3436 mm. While the horizontal beam sizes were approximately 0.48 mm for both planes.

3. The operating conditions of SPS storage ring with the high field insertion devices.

In order to respond to the requirement of beamline user, the operation beam current with two IDs has to be higher than 50 mA after operating for 11 hours at 1.2 GeV beam energy due to the intensity of beam. At a machine operation of 4.0 Tesla SWLS and 4.6 Tesla SWLS with 2.18 Tesla MPW modes, the beam lifetime productions are 74,685 and 62,314 mA.min, respectively. The beam current is higher than 50 mA. The electron orbits are in a range lower than 10  $\mu\text{m}$  and 30  $\mu\text{m}$  for horizontal and vertical axes except at the position of the two insertion devices compared to the reference orbit. However, the orbit stability can be controlled well within 10  $\mu\text{m}$  using the SOFB for about 11 hours.

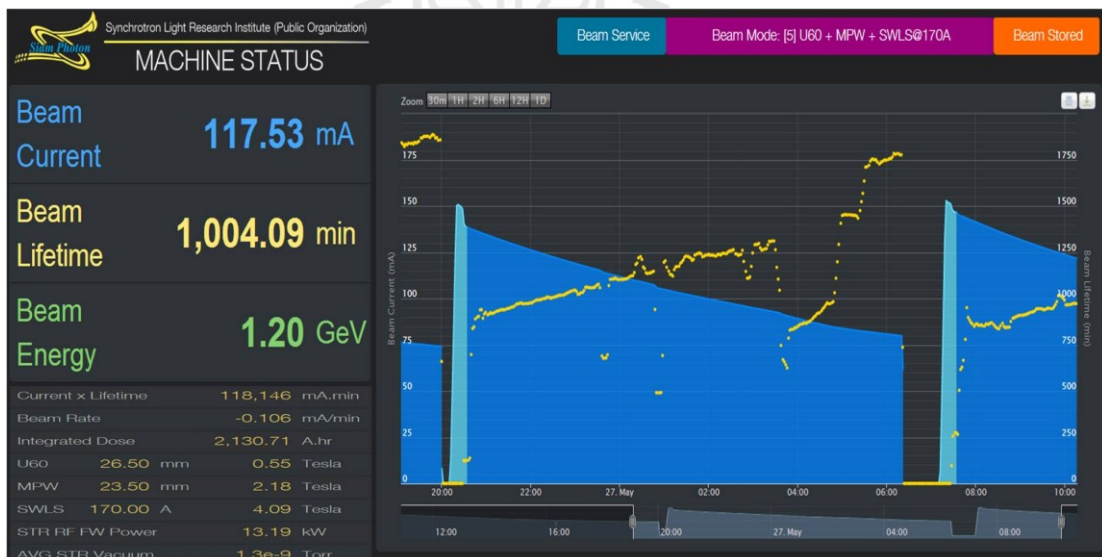


**Figure 6.1** The machine operation with 4.0 Tesla SWLS, 2.18 Tesla MPW, and 0.55 Tesla U60 at 1.2 GeV beam energy and beam current of 117 mA (<http://accelerator.slri.or.th>).



## REFERENCES



## REFERENCES

- Attal, M. (2013). Influence of the vacuum chamber limitation on dynamic aperture calculation, **International Particle Accelerator Conference** PP. 2543-2545.
- Artamonov, A. S., Barkov, L. M., Baryshew, V. B., Bashtovoy, N. S., Vinokurov, N. A., Gluskin, E. S., Korniyukhin, G. A., Kochubei, V. A., Kulipanov, G. N., Mezentsev, N. A., Pindiurin, V. F., and Skrinsky, A. N. (1980). First results of the work with a superconducting “snake” at the VEPP-3 storage ring, **Nuclear Instruments and Methods in Physics** 177: 230-246.
- Aslaninejad, M., Guiducci, S., and Preger, M. (2007). Electron trajectory in the DAFNE wigglers, **EUROTeV-Memo 2007- 002**.
- Bengtsson, J. (1997). Tracy-II User manual, unpublished.
- Brown, G., Halback, K., Harris, J., and Winick, H. (1983). Wiggler and undulator magnets – A Review, **Nuclear Instruments and Methods in Physics** 208: 65-67.
- Chao, H. C. (2007). Beam dynamics effects with insertion device for the proposed 3 GeV ring in Taiwan, **European Particle Accelerator Conference** PP. 196-198.
- Chunjarean, S., and Shin, S. (2011). Insertion devices and beam dynamics in the PLS-II storage ring, **International Particle Accelerator Conference** PP. 2187-2189.
- Clarke, J. A. (1997). The magnetic design of a high field permanent magnet multipole wiggler for the SRS, **Particle Accelerator Conferences** 3: 3503-3505.

- Clarke, J. A., and Dobbing, G. S. (1999). Commissioning of the new multipole wiggler in the SRS, **Particle Accelerator Conference** PP. 2653-2655.
- Clarke, J. A., Bliss, N., Fayz, K., Hannon, F. E., Hill, C., and Reid, R. J. (2003). A very high magnetic field strength permanent magnet multipole wiggler for the daresbury SRS, unpublished.
- Clarke, J. A. (2013). Insertion devices: permanent magnet undulators, (online) Available : [http://www.cockcroft.ac.uk/education/PG\\_courses\\_200910/Spring\\_2010/Lecture%204.pdf](http://www.cockcroft.ac.uk/education/PG_courses_200910/Spring_2010/Lecture%204.pdf).
- Corbett, J., and Nosochkov, Y. (1999). Effect of insertion device in SPEAR-3, **Particle Accelerator Conferences** 4: 2358-2360.
- Farvacque, L., Laclare, J. L., and Ropert, A. (1987). BETA user guide, **ESRF-SR/LAT-88-08**: 1.
- Feikes, J., and Wuestefeld, G. (2003). Lifetime reduction due to insertion devices at BESSY II, **Particle Accelerator Conferences** 2: 845-847.
- Hitchcock, A. P., and Neville, J. J. (1999). Applications of synchrotron light to physics and chemistry, **Physics in Canada** 55: 191-198.
- Hwang, C. S., Lin, E. Y., and Fan, T. (2003). Integral magnetic field measurements using an automatic fast long-loop-flip coil system, **IEEE Transactions on Instrumentation and Measurement** 52: 865-870.
- Hwang, C. S., Wang, B., Wahrer, B., Taylor, C., Chen, C, Juang, T., Lin, F. Y., Jan, J. C., Chang, C. H., Chen, H. H., Huang, M. H., Hsu, K. T., and Hsiung, G. Y. (2007). Design, construction, and performance testing of a 6.5 T superconducting wavelength shifter, **Particle Accelerator Conferences** 17: 1229-1234.

- Hwang, C. S., Chang, C. H., Chang, H. P., Chang, C. K., Chen, J. R., Chen, H. H., Chen, J., Chein, Y. C., Fan, T. C., Kuo, C. C., Lin, F. Y., Hsu, K. T., Hsu, S. N., Huang, M. H., Hsiung, G. Y., and Chen, C. T. (2005). Construction and performance of superconducting magnets for synchrotron radiation, **Particle Accelerator Conferences** PP. 2218-2220.
- Hwang, J. G., Jang, S. W., and Kim, E. S. (2010). Issue on beam dynamics in PLS-II, **International Particle Accelerator Conference** PP. 701-702.
- Huang, X., and Corbett, J. (2010). Measurement of beam lifetime and applications for SPEAR3, **Nuclear Instruments and Methods in Physics P.** 14397.
- Grote, H., and Iselin, F. C. (1995). The MAD Program, Version 8, User's Reference Manual, **CERN SL/90-13 Rev. 4.**
- Grote, H., and Schmidt, F. (2011). Mad-X Program, (online) Available: <http://mad.webcern.ch/mad>.
- Kim, ES. (2005). Effects of insertion devices on the beam parameters at the pohang light source, **Journal of the Korean Physical Society** 46: 1125-1130.
- Klinkhieo, S., Sudmuang, P., Krainara, S., Suradet, N., Boonsuya, S., Klysubun, P., Rujirawat, S., and Songsiriritthigul, P. (2012). Commissioning results of slow orbit feedback using PID controller method for the Siam Photon Source, **International Particle Accelerator Conference** 6: 2861-2863.
- Klysubun, P., Rugmai, S., Rujirawat, S., Cheedket, S., Kwankaseam, C., Hoyes G., and Oyamada, M. (2007). Operation and recent developments at the Siam Photon Source, **Asian Particle Accelerator Conference** PP. 607-609.
- Laskar, J. (2003). Frequency map analysis and particle accelerators, **Particle Accelerator Conference** 1: 378-382.

- Liuzzo, S. M., Biagini, M. E., and Raimondi, P. (2012). Frequency map analysis for SuperB, **International Particle Accelerator Conference** PP. 1341-1343.
- Lubell, M. S. (1983). Empirical scaling formulas for critical current and critical field for commercial NbTi. **IEEE Transactions on Instrumentation and Measurement** 19: 754-757.
- Oide, K. (1997). Strategic Accelerator Design, (online) Available: <http://acc-physics.kek.jp/SAD>.
- Onuki, H., Elleaume, P. (2003). **Undulators, wigglers, and their applications**, Taylor & Francis, London.
- Reichet, I. (2007). Frequency map studies for the ILC damping rings, **Particle Accelerator Conference** PP. 2987-2989.
- Robin, D., Safranek, J., Decking, W., and Nishimura, H. (1997). Global beta-beating compensation of the ALS W16 wiggler, **Particle Accelerator Conferences** 1: 799-801.
- Roport, A. (1989). Dynamics aperture, **CERN Accelerator School**, Sweden, CERN 90-04.
- Roport, A. (1998). Lattices and emittances, **CAS CERN Accelerator School: Synchrotron Radiation and Free Electron Lasers**, GENEVA.
- Roszbach, J. Roszbach, and Schmuser, P. (1992). CERN Accelerator School 5th General Accelerator Physics Course, **CERN 94-01** 1: 514.
- Rugmai, S. (2002). Linear effects of the 7.5T Superconducting wiggler on the SPS storage ring, **NSRC-ID-02/02**.
- Rugmai, S. (2005). Effects of high field permanent magnet insertion device on the Siam Photon Source storage ring, **Science Asia** 31 PP. 159-165.

- Safranek, J., Limborg, C., Terebilo, A., Elleaume, P., and Nosochkov, Y. (2002), Nonlinear dynamics in SPEAR wiggler, **Physical Review Special Topics - Accelerators and Beams** 5: 010701.
- Safranek, J., Protmann, G., and Terebilo, A. (2002). MATLAB BASED LOCO, **European Particle Accelerator Conference** P. 1184.
- Sudmuang, P., Klysubun, P., Krainara, S., Poolampong, T., Deethae, N., Suradet, N., and Sitisart, K. (2012). Beam size measurement at Siam Photon Source. **International Particle Accelerator Conference** 6: 906-908.
- Suller, V. P., Marks, N., Poole, M. W., and Walker, R. P. (1983). SRS behavior with a superconducting 5-Tesla wiggler insertion, **Transactions on Nuclear Science** 30: 3127-3129.
- Thananchai, D. (2008). Characterization of soft X-ray undulator for the Siam Photon Source, Doctoral dissertation, Suranaree University of Technology, Thailand.
- Voss, G. A. (1998). A 7.5T superconducting wiggler, **DESY**, manual report.
- Walker, R. P. (1995). Wigglers, **CERN Accelerator School Proceeding** P. 807.
- Wallen, E. (2002). Commissioning of a 6.4 T superconducting wavelength shifter at MAX-lab, **Nuclear Instruments and Methods in Physics** 495: 58-64.
- Wiedemann, H. (1999). **Particle Accelerator Physics II** (2nd ed.). Springer-Verlag Berlin Heidelberg.
- Wiedemann, H. (2003). **Synchrotron radiation**, Springer-Verlag Berlin Heidelberg.
- Wiedemann, H. (2007). **Particle Accelerator Physics II** (3rd ed.). Springer-Verlag Berlin Heidelberg.
- Wilson, M. N. (1983). **Superconducting magnets**, Oxford University Press, New York.



## APPENDIX

### THE INFLUENCE OF HIGH FIELD INSERTION DEVICES ON THE BEAM DYNAMICS OF SPS STORAGE RING

S.Krainara,<sup>a,b\*</sup> P.Sudmuang,<sup>b</sup> S.Maensiri,<sup>a</sup> S.Rugmai,<sup>b</sup> P.Klysubun,<sup>b</sup> A.Tong-on,<sup>b</sup>

<sup>a)</sup> School of Physics and NANOTEC-SUT Center of Excellence on Advanced Functional Nanomaterials, Suranaree University of Technology, 111 University Avenue, Muang District, Nakhon Ratchasima 30000, Thailand

<sup>b)</sup> Synchrotron Light Research Institute (Public Organization), P.O. Box 93, Nakhon Ratchasima 30000, Thailand. \*e-mail: siriwan@slri.or.th

**Abstract:** The Siam Photon Source (SPS) with an electron storage ring having the beam energy of 1.2 GeV was designed to use the primary source from bending magnets. In order to response the requirement of hard X-ray synchrotron radiation to the beam line user, the Synchrotron Light Research Institute (SLRI) have planned to install two high field insertion devices into SPS storage ring consisting of the 6.5 T Superconducting Wavelength Shifter (SWLS) and 2.4 T Hybrid Multipole Wiggler (MPW). These devices will provide higher the photon energy and flux density of synchrotron radiation than those of bending magnets. The effect on electron beam optic parameters after installing SWLS and MPW such as the betatron tune shift, betatron function beating, emittance blow up, and energy loss are studied in this



presentation. In order to obtain these effects precisely, the calculations will be performed by using three different codes consist of MAD-X, AT-ROOT and TRACY-3.



## **CURRICULUM VITAE**

**NAME** Miss Siriwan Krainara

**DATE OF BIRTH** January 23, 1987

**PLACE OF BIRTH** Nakhon Si Thammarat, Thailand.

**PERSONAL ADDRESS** 179/3, Bangroop sub-district, Thungyai district,  
Nakhon Si Thammarat 80240, Thailand.

**MOBILE** 66-878948919

**E-MAIL** siriwan@slri.or.th, krainara@gmail.com.

**EDUCATIONS**

2012 - present Master of Science (School of Physics)  
at Suranaree University of Technology,  
Nakhon Ratchasima, Thailand.

2004 - 2008 Bachelor of Science (Computational Science)  
at Walailak University, Nakhon Si Thammarat,  
Thailand.

**WORK EXPERIENCE**

2008 - present Beam dynamics group, Accelerator Technology  
division, Synchrotron Light Research Institute  
(Public organization), Nakhon Ratchasima,  
Thailand.